AMPLITUDE CONTROL OF SPIN-TRIPLET SUPERCURRENT IN SUPERCONDUCTOR/FERROMAGNET/SUPERCONDUCTOR JOSEPHSON JUNCTIONS

By

William M. Martinez

A DISSERTATION

Submitted to
Michigan State University
in partial fulfillment of the requirements
for the degree of

Physics — Doctor of Philosophy

2015

ABSTRACT

AMPLITUDE CONTROL OF SPIN-TRIPLET SUPERCURRENT IN SUPERCONDUCTOR/FERROMAGNET/SUPERCONDUCTOR JOSEPHSON JUNCTIONS

By

William M. Martinez

When a conventional superconductor (S) is placed in contact with a ferromagnet (F), the decay length of the pair correlations in the ferromagnet is very short, on the order of a nm in a strong ferromagnet such as Co or Fe. This is due to the spin-polarized nature of the ferromagnet, whereas the spins of Cooper pairs in a conventional superconductor are anti-aligned in a spin-singlet state. However, in 2001, theorists predicted that long-range pair correlations in a spin-triplet state could be generated through magnetic inhomogeneity. With parallel spins, the decay length of these correlations extends in principle to that of a superconductor-normal metal system, which can be on the order of a micron at sufficiently low temperature.

This effect has been observed experimentally by several groups, commonly through the use of extrinsic magnetic inhomogeneity in samples with multiple magnetic layers. Josephson junction measurements have demonstrated critical currents orders of magnitude larger in samples with this inhomogeneity compared to samples without. However, the ability to reliably control the spin-state of the pair correlations in a single sample has yet to be realized.

The goal of this work is to perform measurements on Josephson junctions in which the inhomogeneity can be manipulated. Our approach is to fabricate S/F'/F/F"/S Josephson junctions where we can control the relative magnetization orientations of all three ferromagnetic layers. In order to realize this control, we first had to perform studies to characterize

various magnetic materials, most notably a NiFe alloy similar to Permalloy and Co/Ru/Co, a synthetic antiferromagnet. Studies of the NiFe have demonstrated its ability to be used as a spin-triplet generator. Measurements have also been taken of NiFe films to determine how easily its magnetization direction can be rotated in an external field. We have also measured the magnetic hardness of Co/Ru/Co synthetic antiferromagnets as a function of the Co thickness. By keeping the Co thin, we can minimize the rotation of this layer under the influence of small applied magnetic fields.

Using these results, we demonstrate amplitude modulation of the supercurrent in S/F'/F/F"/S Josephson junctions which is dependent on the magnetization direction of NiFe. Through the use of an external field, the magnetization of the NiFe F" layer can be rotated with respect to the magnetization of the Co/Ru/Co F layer. By rotating into and out of a non-collinear state, we have demonstrated the ability to tune the supercurrent from a spin-triplet to a spin-singlet state, effectively turning the supercurrent in these junctions "on" and "off."

This thesis is dedicated to my parents, Anita and Michael Martinez.

ACKNOWLEDGMENTS

In writing these acknowledgments, I am reminded of how fortunate I am to have had the support of so many amazing people. There are far too many to name them all, and I sincerely apologize in advance for leaving anyone out.

First and foremost, I would like to thank my adviser, Professor Norman Birge. Since the first physics class I had as an undergraduate almost 11 years ago, I have turned to you for advice on a wide range of topics. Your guidance and mentoring have been invaluable. I sincerely thank you for your time and patience through the years, as well as your constant assistance during the stumbles along the way. I am honored to have had you as an adviser.

I also want to thank Professor William Pratt, whose experimental knowledge and engineering skills know no equal. A constant fixture in the lab, I cannot thank you enough for all your help, especially regarding QD-II and QD-VII. I might still be trying to repair those probes if it weren't for you.

It is no exaggeration to say that my research would not be possible without the help of Dr. Reza Loloee and Dr. Baokang Bi. I cannot believe how much I have learned from you both, and am so thankful for all your time and patience. I have looked up to you both for so long and with pride call you not only my mentors but also my friends.

I have received a lot of guidance and encouragement from my committee members: Professors William Hartmann, Carlo Piermarocchi, Kirsten Tollefson, and Remco Zegers. When various projects weren't panning out as expected, the sound advice I received from them kept me on track.

My research group has been amazing, and I have learned so much from various members, past and present, and I hope I can pass on even half of it: Michael Crosser, Charles

Moreau, Gassem Alzoubi, Trupti Khaire, Mazin Khasawneh, Yixing Wang, Eric Gingrich, Bethany Niedzielski, Joseph Glick, Victor Aguilar, Alex Cramer, Brandon Ewert, Patrick Quarterman, Kevin Barry, Kevin Werner, Kurt Boden, and Ilya Beskin. Beyond mentoring, you've made the lab much more fun. That also goes for all my other coworkers, especially Sean Wagner, Ian Dayton, Jess West, Connor Glosser, and Bai Nie. You've all made the basement a brighter place.

I would be remiss if I didn't acknowledge the help from various faculty and staff in BPS. So much of our equipment is made or altered in the machine shop, which has an unbelievably friendly and helpful staff. I want to recognize Tom Palazzolo, Tom Hudson, Jim Muns, and Rob Bennett for the countless hours spent machining the parts we rely on. While experimentalists couldn't get by without the machine shop, none of the students could get through graduate school without the help of our secretaries, who all too often go unrecognized for their work. For their help and patience along the way, I want to thank Cathy Cords, Debbie Barratt, and Kim Crosslan, my work mom.

Speaking of moms, I have to acknowledge my family, including the Stockmeiers and Magañas in that category. This is especially extended to my parents, Mike and Anita. They have stood by me and helped out more than I can say, even when I haven't been so patient in return. My brother John deserves equal thanks, as he always knew how to get the smile back on my face whenever it started to fade.

In addition to those previously mentioned, I have to thank my friends that have pulled me through more than they realize. To those I've met in graduate school, especially Katie Corker, Paul Curran, Steve Fawley, Eric Macaulay, Aaron Mosier, and Kelly Smith, I know we all have limited free time in our programs. Whether playing board games or having philosophical discussions over beer, it means a lot that you'd spend yours with me. With

that, the recent addition of murder mysteries with my neighbors Ben Loseth and Nicki Larson have been a great way to wrap up a weekend. I want to thank my teammates, especially Kortney Cooper, Daniel Couvertier, Aaron Hoffer, Chris Prokop, and Steve Quinn. Running around on the courts or in the sunlight has been a breath of fresh air and a welcome change from the work routine.

I am fortunate enough to still be close with many friends from my past, and they have all been sources of both enjoyment and encouragement. To those I've met as an undergrad, especially Patrick Breen, Jeff Craig, Cullen Dembowski, Andrew Keller, Tyler Neal, and Caleb Wojcik, as well as those from even before, including Peter Butzen, Paul Casperson, Pat Dineen, Monica Fumorolo, Alex Mohr, Logan Price, Marie Russo, Maggie Ryan, Jack Scacco, Tim Schram, Arjun Venkataswamy, and Terry Whittington, I cannot express how much you mean to me.

Special thanks must go to my Little, Deveontye Brown. While we haven't been able to hang out as much as either of us would have liked, I know I can count on you to help me switch out of work mode from time to time.

Despite fitting into many of the above categories, individual recognition has to be paid to Aimee Shore. Amazingly supportive, especially in these past few months, the term "neighbor" doesn't seem to do it justice. You and the drawing on my fridge are constant reminders of life outside of the basement.

Whether explicitly mentioned or apologetically omitted, thank you all.

This work has been supported by US-DOE grant DE-FG02-06ER46341.

TABLE OF CONTENTS

LIST OF TABLES

LIST OF FIGURES

Chapter 1

Introduction

1.1 Motivation

At the turn of the 20th Century, experimentalists were investigating the effect of temperature on the electrical resistance of metals. They had found that, as the temperature decreases, the resistance of the metal also decreases. However, due to the limited temperature range of refrigeration systems available at the time, the question of "What happens to a metal's resistance as it approaches absolute zero temperature?" had remained one for theorists.

However, in 1908, Heike Kamerlingh Onnes successfully liquefied Helium, which condenses at 4.2 K. This novel cryogenic liquid opened a regime of low-temperature physics that had yet to be realized. In 1911, Onnes dipped a sample of mercury into liquid helium to measure the resistance as it dropped towards 0 K, discovering superconductivity in the process [1]. Although it took decades to develop a theory for this drop in resistance [2], research involving superconductivity has become a major aspect of condensed matter physics.

Since the discovery of superconductivity just over a century ago, numerous subfields have emerged, many leading to technological applications useful to society. Superconducting magnets are used in a wide range of fields, from medical uses in MRI machines to accelerator labs, where nuclear and high energy physicists around the world probe the very foundation of matter.

Although they may not be in the public eye as much as those mentioned above, research is

constantly being done to find new applications for superconductors in society. For evidence of this, we need to look no further than the limitations of silicon-based computing [5]. While traditional computing is reaching its limit, the desire for higher powered computers continues to grow, evidenced by frequent benchmarking competitions [6]. In an effort to move away from the silicon-based transistors in conventional computing, a lot of work is being done to realize quantum computing. The foundation of quantum computing revolves around superconducting qubits, quantum dots that remain in a superposition of two states. Although one company has claimed to have developed the first iteration of these computing "holy grails" [7][8], critics and supporters alike agree that quantum computing is in its infancy.

Superconducting logic circuits, including reliable magnetic random access memory (MRAM), is another type of applied superconductivity being sought [9][10]. In principle, superconducting memory can be achieved by either controlling the supercurrent amplitude or the phase of a Josephson junction. The work described in this thesis is also aimed at realizing control over the supercurrent amplitude in superconducting-ferromagnetic Josephson junctions, the culmination of decades of theoretical and experimental results [11].

In this work, we use conventional superconductors (S) that carry spin singlet Cooper pairs. In Josephson junctions with a normal metal (N) barrier, supercurrent can be measured even in junctions with barriers as thick as a micron. When a ferromagnet (F) is inserted as a barrier between two S electrodes, the Cooper pairs die out very quickly, an effect of the spin-polarization of ferromagnets [12]. However, previous theoretical and experimental results have shown that in Josephson junctions with multiple magnetic layers, i.e. $S/F_1/F_2/F_3/S$ junctions, it is possible to generate spin-triplet pair correlations from the spin-singlet Cooper pairs [13]. These correlations have much longer length scales, reminiscent of those of S/N/S

systems.

As will be discussed in the next chapter, this triplet generation is dependent on magnetic inhomogeneity between ferromagnetic layers. If adjacent F layers have collinear magnetization directions, there will be no triplet generated. The spin-singlet pair correlations will dephase rapidly, and the critical current will be quite small. If, however, there is non-collinearity between all adjacent F layers, a large spin-triplet supercurrent can be measured across the junction. Therefore, if one can control the orientation of the magnetizations of the F layers, the ability to tune the amplitude of critical current follows. Control over these parameters, the magnetization and critical current amplitude, is the focus of this thesis.

While the work herein has been investigated largely for the sake of discovering new and novel advancements for science, I will make the naive claim that it may be useful in any application that requires a system with binary control of a supercurrent amplitude, such as the MRAM mentioned above. Regardless of future outcomes or lack thereof, it is with excitement that I can present the results of this work, demonstrating reliable control of critical current amplitude in superconducting Josephson junctions with ferromagnetic barrier layers.

1.2 Thesis Structure

The intent of this thesis is to demonstrate our most recent attempts to control the spin-triplet supercurrent in superconducting-ferromagnetic Josephson junctions. There is a lot of background information that needs to be conveyed first, and will be discussed in the following way:

Chapter 2 will discuss the theoretical background of the systems employed in our work.

It will start with an overview of ferromagnetism and superconductivity and move on to the physics at the interface of these materials. The background principles of Josephson junctions will follow, with an emphasis on the short-range nature of the supercurrent in junctions with a ferromagnetic barrier. The chapter will wrap up with a discussion of various mechanisms to generate long-range superconducting pair correlations, capable of being detected through thick ferromagnetic layers.

Chapter 3 will take a look at the previous experimental work that facilitated this research. The results therein will be mostly composed of relevant contributions from previous and current group members; these include the realization of long-range spin-triplet correlations, the characterization of Ni as a hard ferromagnet, and the characterization of NiFeMo as both a spin-triplet generation layer as well as a soft magnet whose magnetization can be switched easily. This chapter will also feature work done by another group investigating very similar physics; junctions they have created have demonstrated, in a certain measurement scheme, the ability to switch from spin-singlet to spin-triplet supercurrent.

Chapter 4 will focus on sample fabrication. It will feature an analytical look at the equipment used for preparation, deposition, and characterization of samples, all of which have been made in-house. It will also feature the recipe used to create our Josephson junctions.

Like Chapter 4, Chapter 5 will be mechanical in nature as it discusses the equipment necessary to measure our samples. This includes the functionality of the quick-dipper system used to submerge samples in liquid helium and the principles of a SQUID-based measurement system. The former is necessary to generate the required magnetic fields at the sample while the latter is a high-precision measurement tool that yields excellent signal-to-noise capabilities.

Chapter 6 is included to demonstrate the important properties of individual layers in our

Josephson junctions. With three different magnetic layers being utilized in these samples, it is important to understand how each are affected by an external magnetic field. The chapter will be primarily concerned with two layers: NiFe and Co/Ru/Co. (The NiFe used in this work deviates marginally from the common alloy Permalloy (Py), which consists of 80% Ni, 20% Fe.) Discussion of the former will focus on its spin-triplet generation capabilities and the ease of rotating its magnetization in the same manner as had been done for NiFeMo. In contrast, discussion of the latter will focus on its ability to be used as a relatively hard ferromagnet, demonstrated in the magnetization's lack of response to an external field, at least when the field is small.

Finally, in Chapter 7, the data demonstrating our ability to control spin-triplet supercurrent in ferromagnetic Josephson junctions will be presented. This will include the procedure utilized to obtain these measurements and diagrammatic representation of each layer's magnetization direction at various times of measurement, an important understanding necessary to glean any relevant information from the data.

Chapter 8 will be a brief summary of the work that preceded it, as well as a quick look at future research areas that emerge as a result.

For those interested, the appendix will feature important aspects of a project intended to probe the range of the spin-triplet supercurrent in superconducting-ferromagnetic Josephson junctions. To the dismay of this author, despite evidence of successful fabrication, the supercurrent in this geometry has not yet been observed as of the time of writing this thesis. While not entirely understood, possible reasons, as well as potential directions for future research, will be analyzed.

Chapter 2

Theory

Traditionally, superconductors (S) and ferromagnets (F) are considered systems with opposing forms of order. The spin-polarized nature of ferromagnets directly contrasts the anti-parallel spin nature of Cooper pairs. And yet, the work described in this dissertation is fundamentally reliant on the interplay between these systems. This section will discuss the principles of these materials, the interaction at their interface, and the background of how experimental interest emerged from systems of such opposing order.

2.1 Ferromagnetism

Magnetism is a physical property with which every reader likely has experience, from a tool with which one can affix items to the kitchen refrigerator to a navigating aid in the form of a compass needle. However, despite the effects of magnetism being known for millennia, the fundamental properties of ferromagnets are complex enough to warrant research interest today.

Ferromagnets are materials whose magnetic moments are predominantly aligned parallel to their nearest neighbor, creating a microscopic magnetic moment

$$\vec{\mu} = -\frac{ge}{2m}\vec{J} \tag{2.1}$$

where $\vec{J}$ is the orbital or spin angular momentum, e is the charge of an electron, m is the mass of an electron, and g is the gyromagnetic ratio, such that $g = 1$ for purely orbital motion and $g = 2$ for purely spin (else $1 < g < 2$). The macroscopic magnetization can be determined as

$$\vec{M} = \frac{1}{V} \sum \vec{\mu} \tag{2.2}$$

where V is the volume of the material. Although there are two main microscopic sources of magnetism, orbital motion and spin, the spin term generally has more effect on the macroscopic magnetization [14].

The alignment of atomic spins, inherent in some materials and absent in others, depends on the exchange constant (J_{ab}). Although only equivalent in specific circumstances, i.e. electrons in orthogonal orbitals, it is useful to think of the exchange constant as analogous to the exchange integral, J_{ex}. According to the Pauli-exclusion principle, fermions must be anti-symmetric about exchange. If we consider a two-particle system, the Pauli-exclusion principle states

$$\Psi(x_1, s_1; x_2, s_2) = -\Psi(x_2, s_2; x_1, s_1) \tag{2.3}$$

for particles located at x_1, x_2 with spins s_1, s_2 [15]. Therefore, if the particles are symmetric spatially, they must be anti-symmetric about spin and vice versa. In a ferromagnet, Coulomb repulsion is minimized with a spatially anti-symmetric wavefunction, and therefore the spins must align.

In terms of energy, this can be modeled by the Heisenberg Exchange or Heisenberg-Dirac Hamiltonian

$$\mathcal{H} = -2J_{ab}\vec{s}_a * \vec{s}_b \tag{2.4}$$

where $\vec{s}_{a,b}$ is the spin of the electron located at a or b [16][17]. The energy can be minimized when considering the interplay between spins and exchange constant. This interaction governs whether neighboring spins tend to align parallel in systems with $J_{ab} > 0$ or anti-parallel if $J_{ab} < 0$. Ferromagnets have $J_{ab} > 0$.

2.1.1 Balancing Act: Energies and Domains

A material will develop a magnetic structure such that its energy is minimized. While exchange is a major source of the total magnetic energy, there are several other types of interaction that also influence the magnetization of a sample. These include magnetostatic, magnetocrystalline, magnetostrictive, and Zeeman energies.

Magnetostatic energy is directly related to the shape of the material. To determine the magnetostatic energy, one must integrate the interaction between the magnetization and internal field, $\vec{H}$, which point in opposite directions due to the demagnetizing nature of the internal field [18]. The larger the region of aligned spins, the larger the internal field becomes in opposition of this magnetization. Depending on size and shape of the material, this energy can become quite large, forcing the system to find other ways to minimize internal energy (discussed below). If the system has a favored magnetization direction, it is called the easy axis. A sphere has perfect shape symmetry about all axes and therefore has no preferential magnetization direction. In contrast, a long straight wire has uniaxial symmetry in which the energy is minimized by pointing the magnetization along the wire. A thin disc, which is symmetric in two planes but very thin in the third, will minimize energy with an easy axis laying in the plane of the disc. This geometry is the one utilized in this work, and although it confines the magnetization in-plane, the magnetostatic energy forces no further favored direction within it.

The magnetocrystalline energy is an effect of magnetocrystalline anisotropy which arises from the crystal structure. To first order this is an effect of spin-orbit coupling, and the orbital motion of electrons can couple to the electric field inherent in the crystal [18][19]. In order to confine magnetization in this way, however, there must be asymmetry in both the electric field and orbitals. Otherwise, no direction is favorable, and magnetization can align randomly. For example, in certain alloys such as NiFe (Permalloy), the locations of the Ni and Fe atoms can induce a magnetocrystalline anisotropy. The direction of this anisotropy can be set by growing NiFe films in an external magnetic field. As the film grows, the positions of Ni and Fe within the crystal preferentially favor the asymmetry desired. While weak compared to the exchange interaction, the effect of magnetocrystalline anisotropy can define a preferential direction when others may not exist. Considering the undetermined easy axis in the example of a thin-disc above, controlling the crystal growth, and thus magnetocrystalline anisotropy, will confine the easy axis in a single direction.

Magnetostriction is an effect of the stresses on the magnetic material. The energy from these stresses relates how a ferromagnetic sample will expand or contract due to its magnetization. Conversely, strain induced during film growth can induce magnetic anisotropy. The shape of the system can change due to this energy, which brings about yet another competitor of the exchange energy.

The Zeeman energy arises when a sample is exposed to an external field. In order to minimize the internal magnetic energy, moment direction and magnetic structure may change in the presence of a field. This is discussed more thoroughly in Section 2.1.2.

Clearly, ferromagnetic systems are very complex. Therefore, when trying to minimize the internal energy, it is necessary to consider much more than solely the parallel or anti-parallel nature of nearby moments. In bulk materials, these competing energies can overcome the

exchange energy, minimizing the total energy in the system through the creation of domains. The existence of domains was originally predicted in 1907 [20], and the first experimental effects of them were first observed in 1919 [21]. By creating domains, areas of aligned spin that are different from one another, the magnetostatic and magnetostrictive energies can become minimized at the cost of an increase of the exchange energy at the edge of these domains [22]. These edges, called domain walls, are regions where the spins of nearby moments undergo a change of direction.

Domains can be directly observed a number of ways. The first observation occurred when magnetite deposits oriented along surface domain walls of a Ni sample [23]. While this demonstrated the boundary regions, the domains themselves were later imaged optically using polarized light [24]. The plane of light polarization is affected by the domain direction, and therefore can be used to directly image surface domains.

To minimize the magnetostatic energy, which is directly analogous to the external magnetic field, a material will create its domain structure in order to reduce its external field. Domains which eliminate this field are called closure domains [19], and materials with perpendicular easy axes will form closure domains with no additional energy cost. Otherwise, closure domains would not be pointing along the easy axis, thereby increasing the magnetocrystalline energy. The domain size will also be influenced by the magnetostrictive energy. Domains that have magnetizations unaligned will expand/contract the crystal in conflicting ways. This effect adds an elastic strain energy, which is smaller for smaller domains. To keep domains small would, however, require more of them, which increases the exchange energy. With so many competing energy terms, determining the domain structure of a material is no simple task.

The size of the wall is another complex consideration [19]. An abrupt switch is unfavor-

able with respect to exchange energy, which would prefer a slow rotation of spin. If long enough, nearest neighbors are marginally misaligned, keeping energy between these moments low. However, shape and crystalline structure favor alignment along the easy axis (if one is present). Because of this, slow rotation of spins may not be as favorable, instead promoting a narrow domain wall.

If the sample is kept small enough, it is possible to create ferromagnetic films that are single domain. The NiFe switching layer discussed in this work (see Sections 6.1, 7.4) has been patterned small enough to ensure this.

2.1.2 Magnetization

The Zeeman energy arises within a material when it is placed in an external field. This additional energy term will alter the domain structure, causing magnetic domains to move or even be removed completely. This process will be described here and is demonstrated in Figure 2.1a.

Consider a bulk ferromagnet that has domains pointing in all directions. While minimizing the internal energy, domains have formed that resulted in no net magnetic moment. Recall that minimizing the internal energy is analogous with minimizing external field, i.e. enclosing the magnetization completely also minimizes the internal energy. At this point, this sample is considered at its lowest energy state and unmagnetized.

As an external field is applied, magnetic moments will attempt to point in the same direction as this field. The effect can be as subtle as increasing the size of domains that point parallel to the external field to more extreme effects such as complete rotation or elimination of domains depending on the field and size of individual energy parameters. For example, a long, thin wire will move domains along it's length more easily than rotating

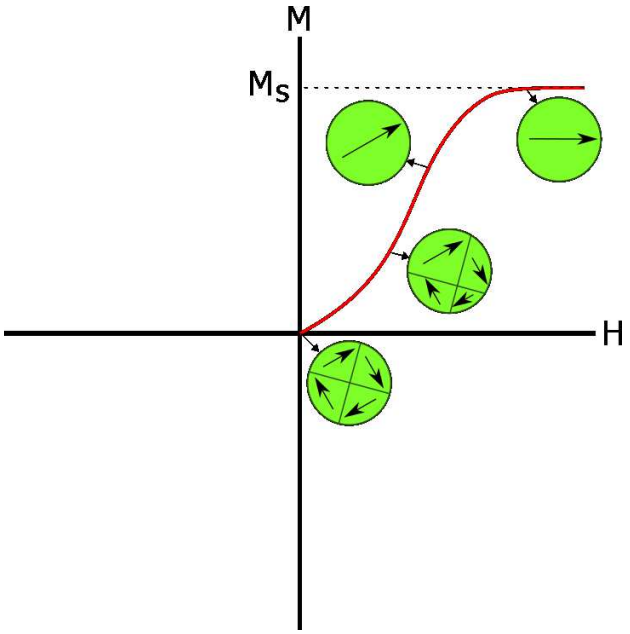

(a)

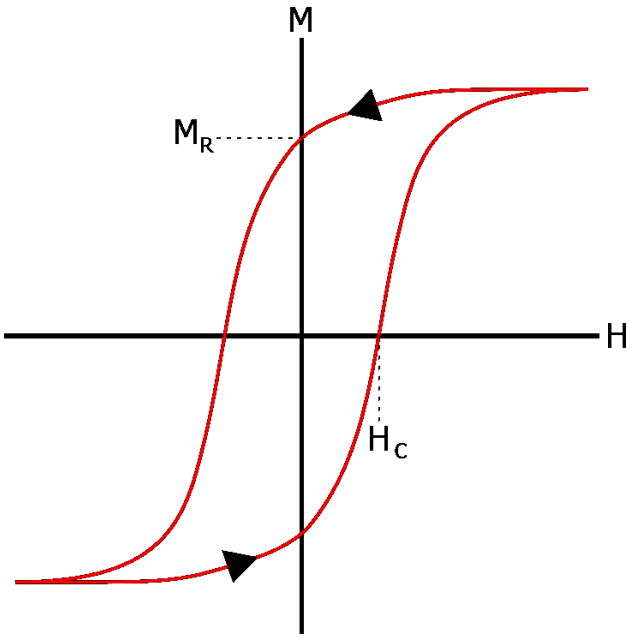

(b)

Figure 2.1 *Magnetization curves.* a) Initial application of field, H, will alter the domain structure (segmented green sections). Domains with moments in the direction of the field will increase in size while opposing moments will decrease. Eventually only one domain will remain and rotate in the direction of applied field, saturating the magnetization (M_s). b) After initial magnetization, measuring M vs H will demonstrate hysteresis. The magnetization that remains at $H = 0$ is called remnant magnetization (M_R), while the field that cancels the magnetization is called the coercive field (H_c).

the magnetization out of the wire itself, which would force the magnetization to point along a hard axis. Within a certain limit, the process is reversible. Decreasing the external field still allows for the domains to rotate and move in an attempt to reset back to its original, unmagnetized state. However, eventually the domains can become pinned, either through crystal irregularities or the elimination of domain walls. Once this occurs, it is not possible to return to an unmagnetized state, at least not by removal of the field alone (while demagnetizing processes exist, including heating the material above its Curie temperature, they are not useful for this work and will not be discussed further). After removal of the external field, that which remains is called the remnant magnetization and is created by the ferromagnet [22].

Once pinning begins, further increases of external field affect the size of the remnant field by moving, removing, or rotating more domains that also become pinned. Eventually, however, all moments will point in the direction of the field, and no more magnetization can be induced. This upper limit is aptly called the saturation magnetization, M_S.

As shown in Figure 2.1b, future measurement of the magnetization as a function of field will yield a hysteresis loop. The field required to demagnetize the sample (i.e. when the curve crosses M=0) is called the coercive field (H_c). These hysteresis loops and magnetization measurements are important when determining the hardness/softness of magnetic material (i.e. larger $H_c \rightarrow$ harder magnet), a necessary consideration when choosing materials to be used in samples.

2.2 Superconductivity

In the early 1900s, experimentalists were exploring the limits of transport in metals at ever colder temperatures. It had been well known that resistance drops with the temperature, but what happened when $T \to 0K$ had long been a curiosity. In 1911, aided by the discovery of liquid helium, Heike Kamerlingh Onnes measured the resistance of mercury as it cooled. What he found was the first evidence of superconductivity, a drop in resistance to 0 ohm at 4.2 K [1]. This discovery was remarkable and unexpected, so much so that his results couldn't be fully explained for almost half a century.

Using aspects of various early theories, especially Leon Cooper's 1956 paper on electron pairs [25], John Bardeen, Leon Cooper, and John Robert Schieffer developed a microscopic theory to explain this phenomena in 1957, now called BCS Theory [2]. The theory is based around the principle idea that, in superconductors, it becomes energetically favorable for electrons to pair together. One electron near the Fermi surface creates a virtual phonon, a region of positive charges in the lattice of the material. This, in turn, attracts another electron (with opposite spin) with sufficient potential energy to overcome Coulomb repulsion between the two. The binding energy (E) of these electrons is

$$E = 2\Delta(0) \tag{2.5}$$

where $\Delta(0)$ is the material-dependent superconducting gap [26]. Scattering events, such as phonon scattering, electron repulsion, lattice defects, etc., are not large enough to overcome this binding energy, and is thus the reason that R drops completely to 0 ohm.

The abruptness of the drop occurs because the superconducting gap energy becomes

greater than that of thermal excitations. Within BCS theory, the relationship between superconducting energy gap and temperature is

$$\Delta(0) = 1.764 k_B T_c \tag{2.6}$$

where k_B is the Boltzmann constant and T_c is the critical temperature, below which the material becomes a superconductor [26].

One final (and very important) aspect of Cooper pairs in the vast majority of superconductors is that their quantum make-up consists of opposite-spin, opposite-momentum electrons. These electrons are called spin-singlet and can be described as

$$|0,0\rangle = \frac{1}{\sqrt{2}}(|\uparrow\downarrow\rangle - |\downarrow\uparrow\rangle). \tag{2.7}$$

The general form of this notation is written as $|s, m_s\rangle$ where s is the total spin quantum number and m_s is the secondary spin quantum number ($-s \leq m_s \leq s$).

Aside from having no resistance, bulk superconductors also exhibit perfect diamagnetism, known as the Meissner Effect [27]. In the presence of a magnetic field, the surface of the superconductor will generate screening currents. This causes the magnetic field to decay exponentially to zero in the superconducting region [26], eliminating the field in the bulk of the superconductor. The repulsion of magnetic field is but another example of the competing nature of superconductors and magnetism. The screening length will be discussed again briefly in Section 2.4.2.

It should be noted that BCS Theory only accounts for traditional, s-wave superconductors with Cooper pairs in the spin-singlet state. While there are many other types of

superconductors, the work herein only utilizes s-wave superconductors, and thus others are beyond the scope of this thesis.

2.3 Proximity Effect

Despite being aware of these materials for a century or more, there is a continued interest in studying the individual fundamental properties of superconductors, ferromagnets, and normal metals (N). However, what is of greater concern to this thesis is the interplay between these very different materials when they are placed in contact with each other, called the proximity effect. Overall, it describes the amount of Cooper pair "leakage" from a superconductor to another material, although the details of the effect are highly material dependent.

2.3.1 Superconductor/Normal Metal

What happens when you place a normal metal in contact with a superconductor? At energies well above the band gap, quasi-particle states exist in the superconductor, and single electron transport can occur. It is instead at electron energies within the superconductor band gap (if e has $|E| < \Delta$) that unique physics can be observed.

At these energies, electrons in the superconductor have paired with spin-opposite counterparts and formed Cooper pairs. There are no states that single electrons from the normal metal can occupy in the superconductor, and so charges of e cannot enter the superconductor (as shown in the band structure of Figure 2.2). This doesn't, however, prevent transport to occur in these systems. Instead, electrons in the normal metal will enter the superconductor and reflect out a hole, a process known as Andreev Reflection [28] (Figure 2.2a), the effect of which is that a charge of $-2e$ enters the superconductor. This is equivalent to saying two

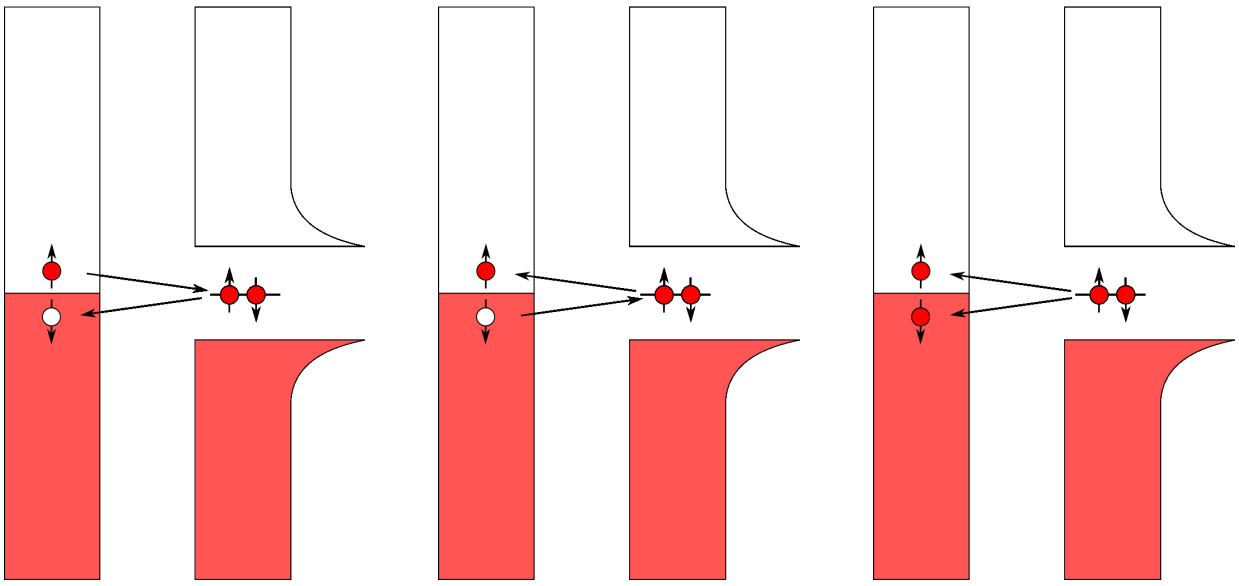

(a) Andreev Reflection (b) Inverse Andreev Reflection (c) Cooper pair leakage from S into N.

Figure 2.2 *Cartoon of pair leakage models.* Energy band diagrams near the Fermi energy for N and S (left and right of each figure, respectively). There are no single states for electrons in N to enter within the superconducting gap in S, and all transport between the two must exchange a charge of $-2e$. This can be modeled as electron from N entering S, retro-reflecting a hole (a) and creating a Cooper pair. This process is known as the Andreev reflection. The inverse Andreev reflection models a Cooper pair in S entering N as a hole incident on the interface, retro-reflecting a single electron (b). This can also be modeled as a Cooper pair leaking into the normal metal, transferring both electrons into N (c).

electrons, or a Cooper pair, enter the superconductor. This process will therefore exchange $2e$ for every transport event.

The inverse process consists of a hole incident on the interface, reflecting an electron, and thus a Cooper pair leaving the superconductor (Figure 2.2b). In this case, one can also look at the process as Cooper pairs leaking into the normal metal (Figure 2.2c). The characteristic decay length scale, or coherence length (ξ), describes how far the two electrons propagate into N before they lose phase coherence with each other. The timespan of the coherence is defined as $\tau = \hbar/\epsilon$, where $\epsilon \approx 2\pi k_B T$ after averaging over the thermal distribution. If the mean free path is much longer than the thickness of the material through which the electron transmits, the particle will travel at the Fermi velocity, v_F, and is said to be in the clean (ballistic) limit. If the material is thicker than the mean free path, like in the samples discussed herein, the electron diffuses through the material via scattering effects according to the diffusion coefficient D. This limit is called the dirty (diffusive) limit. Taking these limits into account, we obtain a "normal metal coherence length"

$$\xi_N = \frac{\hbar v_f}{2\pi k_B T} \tag{2.8}$$

in the clean limit and

$$\xi_N = \sqrt{\frac{\hbar D}{2\pi k_B T}} \tag{2.9}$$

in the diffusive limit [32][33].

The normal metal coherence length is dependent on the thermal energy and material used, but in some systems at low enough temperature ($T \ll 1K$), ξ_N can get as long as a μm.

2.3.2 Superconductor/Ferromagnet

The biggest difference between a normal metal and a ferromagnet is that normal metals have no preferential spin while spins are polarized in a ferromagnet. A rigorous approach to analyzing the effect strong magnetic fields have on Cooper pairs would require us to follow the work done by Flude and Ferrell [29], and Larkin and Ovchinkov [30][31], commonly referred to as FFLO or LOFF. Fortunately though, for our needs, a very simplified approach can be taken by modeling the ferromagnetic band structure as a normal metal in a magnetic field. The resultant Zeeman splitting is demonstrated in Figure 2.3 which plots kinetic energy (E_k) vs wavevector (k) at the interface. In the normal metal, there is only one band structure for all spins. However, in the ferromagnet, the two bands are offset by twice the exchange energy (E_{ex}) of the ferromagnet. Therefore, at the Fermi energy (horizontal black line in the figures), $|k_F|$ will be slightly different for the up-spin electron relative to the down-spin electron.

As discussed, electrons in the superconductor are bound as Cooper pairs and have opposite spin and momentum. If we consider these electrons as they pass through the interface between S and F, the band structure of F will cause the pair correlations to pick up a center-of-mass momentum shift

$$\hbar Q = \hbar(k_F^{\uparrow} - k_F^{\downarrow}) \tag{2.10}$$

which can be simplified to

$$Q = \frac{2E_{ex}}{\hbar v_F} \tag{2.11}$$

if we ignore the Fermi velocity difference between the spin-bands, i.e. $E_{ex} \ll E_F$ [34]. For $|\uparrow\downarrow\rangle$ pairs incident normal to the interface, moving in the x-direction, they will be shifted by

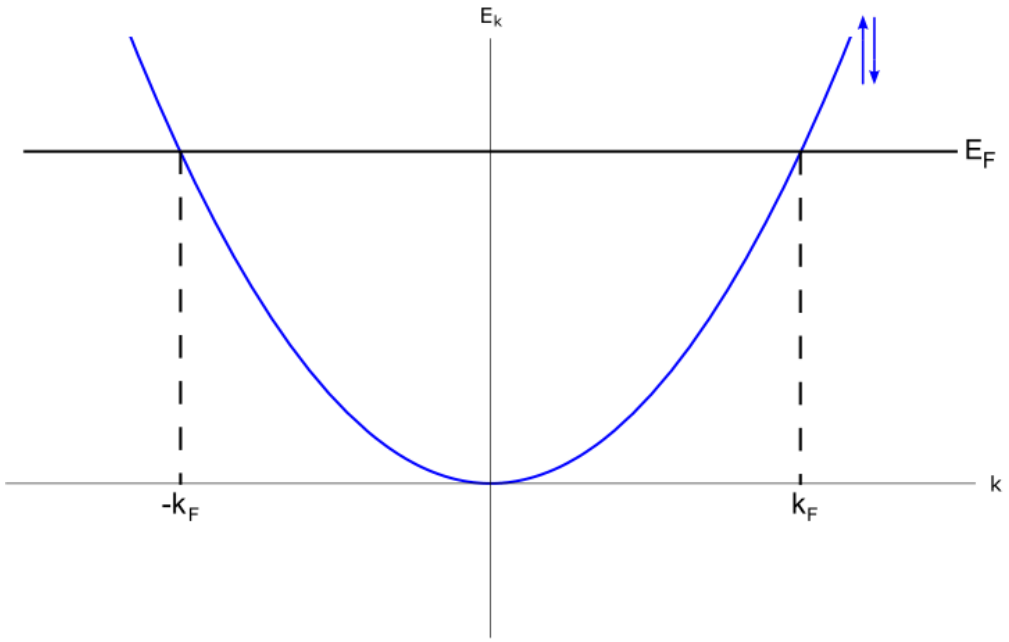

(a)

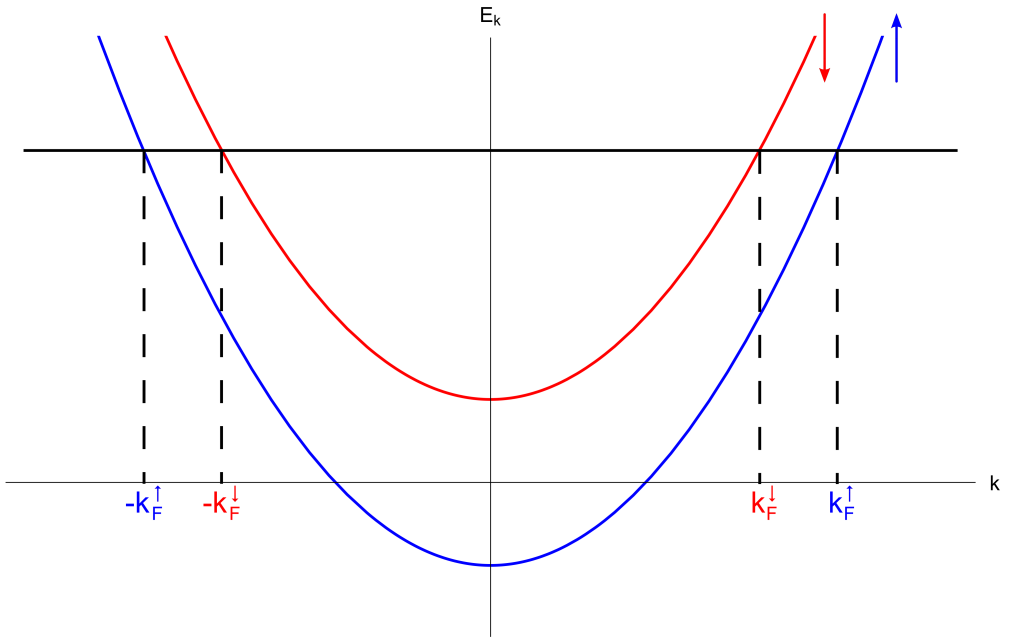

(b)

Figure 2.3 *Interface band structure.* In the case of a normal metal (a), there is no spin-polarization, and both up- and down-spin electrons enter the same band. In the simplified cartoon representation of a ferromagnetic band structure (b), the band separation of $2E_{ex}$ causes the up- and down-spin electrons to enter different bands.

Q while the $|\downarrow\uparrow\rangle$ pairs are shifted by $-Q$, i.e.

$$|\psi\rangle_F = \frac{1}{\sqrt{2}}\left[\exp\left(\frac{iQx}{\hbar}\right)|\uparrow\downarrow\rangle - \exp\left(\frac{-iQx}{\hbar}\right)|\downarrow\uparrow\rangle\right]. \tag{2.12}$$

If the pair is incident on the interface at an angle θ, then since the components of momentum parallel to the interface are conserved, the perpendicular component must be shifted by $Q/\cos\theta$ to conserve energy [34]. Averaging over all possible angles will yield the pair correlation function amplitude (Ψ) and coherence length (ξ_F)

$$\begin{aligned}\Psi &= \frac{\sin\left(\frac{x}{\xi_F}\right)}{\frac{x}{\xi_F}} \\ \xi_F &= \frac{\hbar v_F}{2E_{ex}}\end{aligned} \tag{2.13}$$

in the clean limit and

$$\begin{aligned}\Psi &= \exp\left(\frac{-x}{\xi_F}\right)\sin\left(\frac{x}{\xi_F}\right) \\ \xi_F &= \sqrt{\frac{\hbar D}{E_{ex}}}\end{aligned} \tag{2.14}$$

in the dirty limit.

To compare this result with that of S/N, we need to look closer at E_{ex}. We can estimate $E_{ex} \approx k_B T_C$, where T_C is the Curie temperature of the ferromagnet. Therefore, the relationship between coherence lengths can be approximated as

$$\begin{aligned}\frac{\xi_N}{\xi_F} &\approx \frac{E_{ex}}{k_B T} \\ &\approx \frac{T_C}{T}.\end{aligned} \tag{2.15}$$

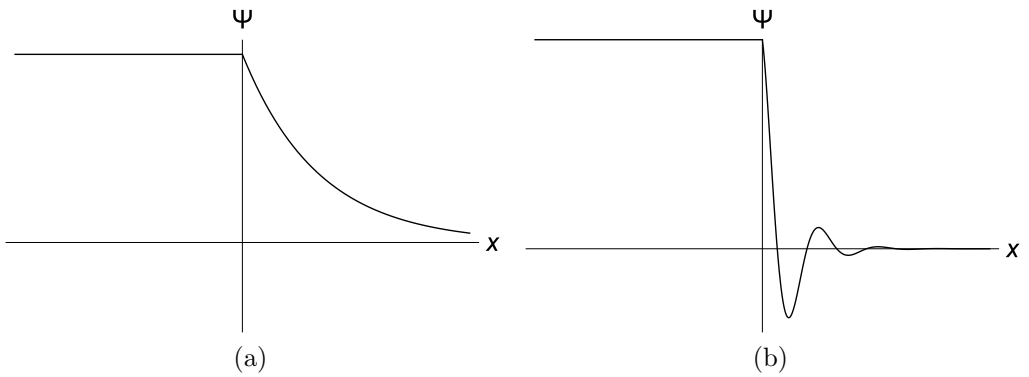

Figure 2.4 *Pair correlation functions.* In a) we can see the S/N pair correlation function while b) demonstrates the same for S/F systems. Both the shortened coherence length and the oscillatory nature are a direct result of the exchange energy present in ferromagnets but absent in normal metals.

Looking at Curie temperatures of common ferromagnets, we find $T_{C,Fe} = 1043$K, $T_{C,Co} = 1388$K and $T_{C,Ni} = 627$K [14]. Taking $T_C \approx 1000K$ as an estimate and measuring at $T = 4$K, the coherence length is roughly 250 times smaller in ferromagnets than in normal metals in the clean limit. Due to the large exchange energy, ξ_F can only extend up to a few nm, in contrast to the μm length obtainable in S/N systems.

The correlation functions are plotted for both S/N and S/F systems in Figure 2.4. An interesting observation is that, in addition to the short coherence length, we obtain an oscillating component in the correlation amplitude in the S/F case.

Because ξ_F is so short, the experiments intended to observe the oscillations in the pair-correlation wavevector (Figure 2.3b) were quite challenging. As an effect of the oscillations, the superconducting critical temperature of an S/F bilayer is predicted to also oscillate as a function of the thickness of the ferromagnet. Combining the difficulties of fabricating thin ferromagnet samples with the presence of magnetically dead layers for very thin F films [35], any observations of oscillations in the critical temperature [36] were difficult to understand. Two experimental breakthroughs were achieved in 2001. By using ferromagnetic

alloys with lower E_{ex}, and thus longer ξ_F, experimentalists were able to observe a change in sign in the structure of the density of states in $Nb/Pd_{1-x}Ni_x$ systems [37]. Further observations of oscillation were reported in systems with a second superconducting electrode, S/F/S Josephson junctions [38][39] (for a discussion on Josephson junctions, see the following section).

2.4 Josephson Junctions

We have seen what happens when materials are placed in contact with a superconductor. What, then, happens if you put superconductors on both sides of a non-superconducting film? As theorized by Brian Josephson, it is conceivable that Cooper pairs will tunnel completely through the barrier between the superconductors [40][41]. These systems became known as Josephson junctions, and although initially demonstrated with an insulating barrier (I), the material separating the superconducting layers can be I, N, or F.

There are two main equations governing the flow of supercurrent in Josephson junctions, known as the Josephson equations, which can be developed by examining the superconducting wavefunction

$$\Psi(\vec{r},t) = \sqrt{n_s^*(\vec{r},t)}e^{i\theta(\vec{r},t)} \tag{2.16}$$

where n_s^* is the local Cooper pair density ($= \Psi^\dagger\Psi$) and θ is the phase of the superconducting condensate. This wavefunction evolves in time according to the Schrodinger-equation in an electromagnetic field

$$i\hbar\frac{\partial\Psi(\vec{r},t)}{\partial t} = \frac{1}{2\mu}(\frac{\hbar}{i}\nabla - q^*\mathbf{A}(\vec{r},t))^2\Psi(\vec{r},t) + q^*\phi(\vec{r},t)\Psi(\vec{r},t). \tag{2.17}$$

We also have an expression for the Cooper pair current density

$$\mathbf{J}_s = \frac{q^*\hbar}{2\mu i}(\Psi^\dagger \nabla\Psi - \Psi\nabla\Psi^\dagger) - \frac{q^{*2}}{\mu}\Psi\Psi^\dagger\mathbf{A} \tag{2.18}$$

where $\mathbf{A}$ is the vector potential, ϕ is the scalar potential, μ is the effective mass of a Cooper pair and $q^* = -2e$, the effective charge of a Cooper pair.

Substituting 2.16 into 2.18 yields

$$\mathbf{J}_s = \frac{q^* n_s^* \hbar}{\mu}(\nabla\theta - \frac{q^*}{\hbar}\mathbf{A}). \tag{2.19}$$

The current therefore depends on the density of the Cooper pairs as well as the gauge-invariant phase gradient $(\nabla\theta - \frac{q^*}{\hbar}\mathbf{A})$. We can calculate the gauge-invariant phase difference (φ) between the superconductors (which we shall label 1 and 2 as shown in Figure 2.5) as a path integral through the junction

$$\begin{aligned}\varphi &= \int_1^2 (\nabla\theta - \frac{q^*}{\hbar}\mathbf{A}) \cdot d\vec{l} \\ &= \theta_2 - \theta_1 - \frac{q^*}{\hbar}\int_1^2 \mathbf{A}\cdot d\vec{l}.\end{aligned} \tag{2.20}$$

With no current, we should expect the phase difference and gradient to also be 0. We also expect that the system should act independently of phase differences of 2π. From these conclusions, assuming the Josephson coupling is weak and combining the leading multiplicative factors as J_c (the maximum critical current in the junction), Josephson obtained the first Josephson equation [41]

$$\mathbf{J}_s = J_c \sin\varphi. \tag{2.21}$$

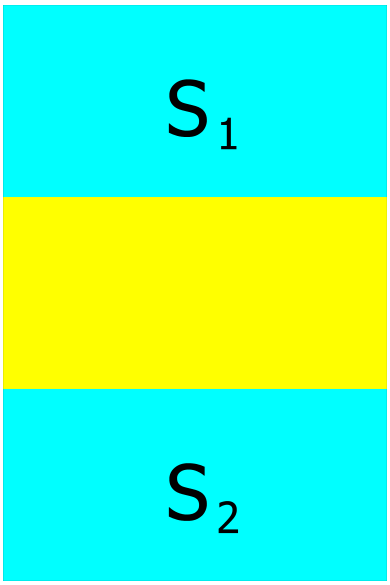

Figure 2.5 *A simple Josephson junction.* S_1 and S_2 are the two superconducting electrodes, labeled for clarity for the derivation of the Josephson equations, and are separated by a barrier layer.

Another derivation of Eqn 2.21 has been done by Feynman [42].

If we assume n_s^* to be constant in time, we can substitute 2.16 into 2.17 to get

$$-\hbar\frac{\partial\theta}{\partial t} = \frac{\mu}{2n_s^{*2}q^{*2}}\mathbf{J}_s^2 + q^*\phi. \tag{2.22}$$

Inserting this into the time evolution of φ, we find

$$\begin{aligned}\frac{\partial\varphi}{\partial t} &= \frac{\partial\theta_2}{\partial t} - \frac{\partial\theta_1}{\partial t} - \frac{q^*}{\hbar}\frac{\partial}{\partial t}\int_1^2 \mathbf{A}\cdot d\vec{l} \\ &= \frac{q^*}{\hbar}(\phi_1 - \phi_2) - \frac{q^*}{\hbar}\frac{\partial}{\partial t}\int_1^2 \mathbf{A}\cdot d\vec{l} \\ &= \frac{q^*}{\hbar}\int_1^2(-\nabla\phi - \frac{\partial\mathbf{A}}{\partial t})\cdot d\vec{l}.\end{aligned} \tag{2.23}$$

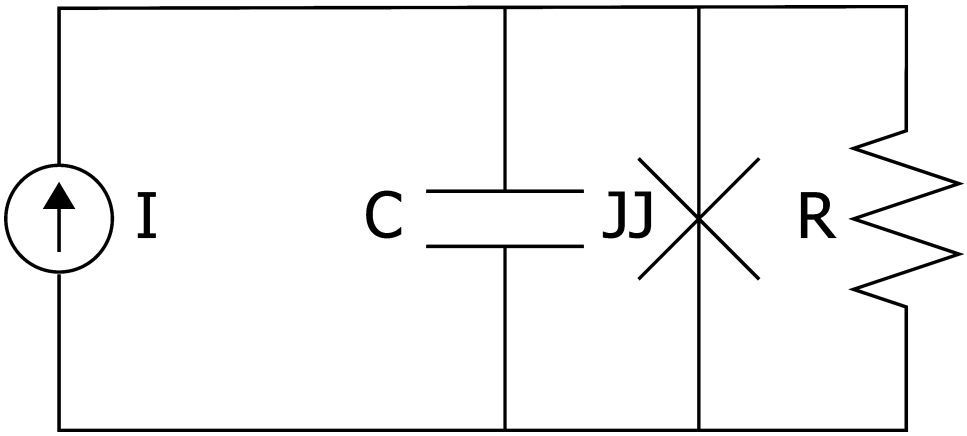

Figure 2.6 *Schematic of a resistively and capacitively shunted junction model.*

Recognizing the integrand as

$$\mathbf{E} = -\nabla\phi - \frac{\partial \mathbf{A}}{\partial t} \tag{2.24}$$

we can integrate to find the second Josephson equation, yielding the voltage-phase relation

$$\frac{\partial \varphi}{\partial t} = \frac{2\pi}{\Phi_0} V \tag{2.25}$$

where $\Phi_0 = \frac{h}{2e}$, the magnetic flux quantum. For $|J| < J_c$, V= 0; $|J| > J_c$, V$\neq$ 0.

2.4.1 RCSJ Model

As stated in the previous section, for $|I| < I_c$, there is no voltage response across the Josephson junction. However, at finite voltage, a separate model needs to be discussed, for which we turn to the Resistively and Capacitively Shunted Junction (RCSJ) model. Figure 2.6 shows an idealized electrical diagram for the RCSJ model, which treats the Josephson junction (JJ) as if it is placed in parallel with a resistor (R) and capacitor (C) [26].

In this model, the resistor acts as a shunt, and therefore only contributes at finite voltage. When $I < I_c$ (V=0), therefore, there are no losses in the resistor. The capacitor accounts for

the geometric shunting capacitance between the two superconducting electrodes. Combining all of these elements, we can describe the system's voltage-current response as

$$I = I_{c0} \sin \varphi + \frac{V}{R} + C\frac{dV}{dt} \tag{2.26}$$

and by using 2.25 we can rewrite this as

$$I = I_{c0} \sin \varphi + \frac{\Phi_0}{2\pi R}\frac{\partial \varphi}{\partial t} + \frac{\Phi_0 C}{2\pi}\frac{\partial^2 \varphi}{\partial t^2}. \tag{2.27}$$

If we multiply by $\frac{\Phi_0}{2\pi}$ we obtain

$$\frac{\Phi_0}{2\pi} I = E_J \sin \varphi + \frac{\Phi_0^2}{(2\pi)^2 R}\frac{\partial \varphi}{\partial t} + \frac{\Phi_0^2 C}{(2\pi)^2}\frac{\partial^2 \varphi}{\partial t^2} \tag{2.28}$$

where E_J is the Josephson coupling energy

$$E_J = \frac{\hbar}{2e} I_{c0} = \frac{\Phi_0}{2\pi} I_{c0}. \tag{2.29}$$

We can solve this differential equation by considering this system as a particle with mass

$$m = \left(\frac{\Phi_0}{2\pi}\right)^2 C \tag{2.30}$$

in a potential

$$U(\varphi) = -E_J \cos \varphi - \frac{\Phi_0}{2\pi} I \varphi \tag{2.31}$$

and acted on by drag force

$$F_D = \frac{m}{RC}\frac{d\varphi}{dt}. \tag{2.32}$$

This is called the "tilted washboard" model [26] and is plotted in Figure 2.7. If we consider an ideal, thermal-fluctuation-free system, the model acts as a particle trapped in a potential well for all $|I| < I_{c0}$. However, at $I = I_{c0}$, the $\cos\varphi$ term has no local minima, only inflection points. A particle in this system is metastable and can slide along with any perturbation. For all $|I| > I_{c0}$ the particle will freely slide along the curve as there are no stable equilibrium points.

It is common to also see equation 2.27 written as

$$\frac{I}{I_{c0}} = \sin\varphi + \frac{1}{Q\omega_p}\frac{\partial\varphi}{\partial t} + \frac{1}{\omega_p^2}\frac{\partial^2\varphi}{\partial t^2} \tag{2.33}$$

where we have introduced both the plasma frequency

$$\omega_p = \left(\frac{2\pi I_{c0}}{\Phi_0 C}\right)^{1/2} \tag{2.34}$$

and quality factor

$$Q = \omega_p RC. \tag{2.35}$$

Q can also be written as $Q = \beta_c^{1/2}$, where β_c is the Stewart-McCumber damping parameter [26].

For overdamped junctions, the regime in which the Josephson junctions in this work exist, $\beta_c \ll 1$. With small C, we can ignore its contribution to equation 2.27

$$I = I_{c0}\sin\varphi + \frac{\Phi_0}{2\pi R}\frac{\partial\varphi}{\partial t} \tag{2.36}$$

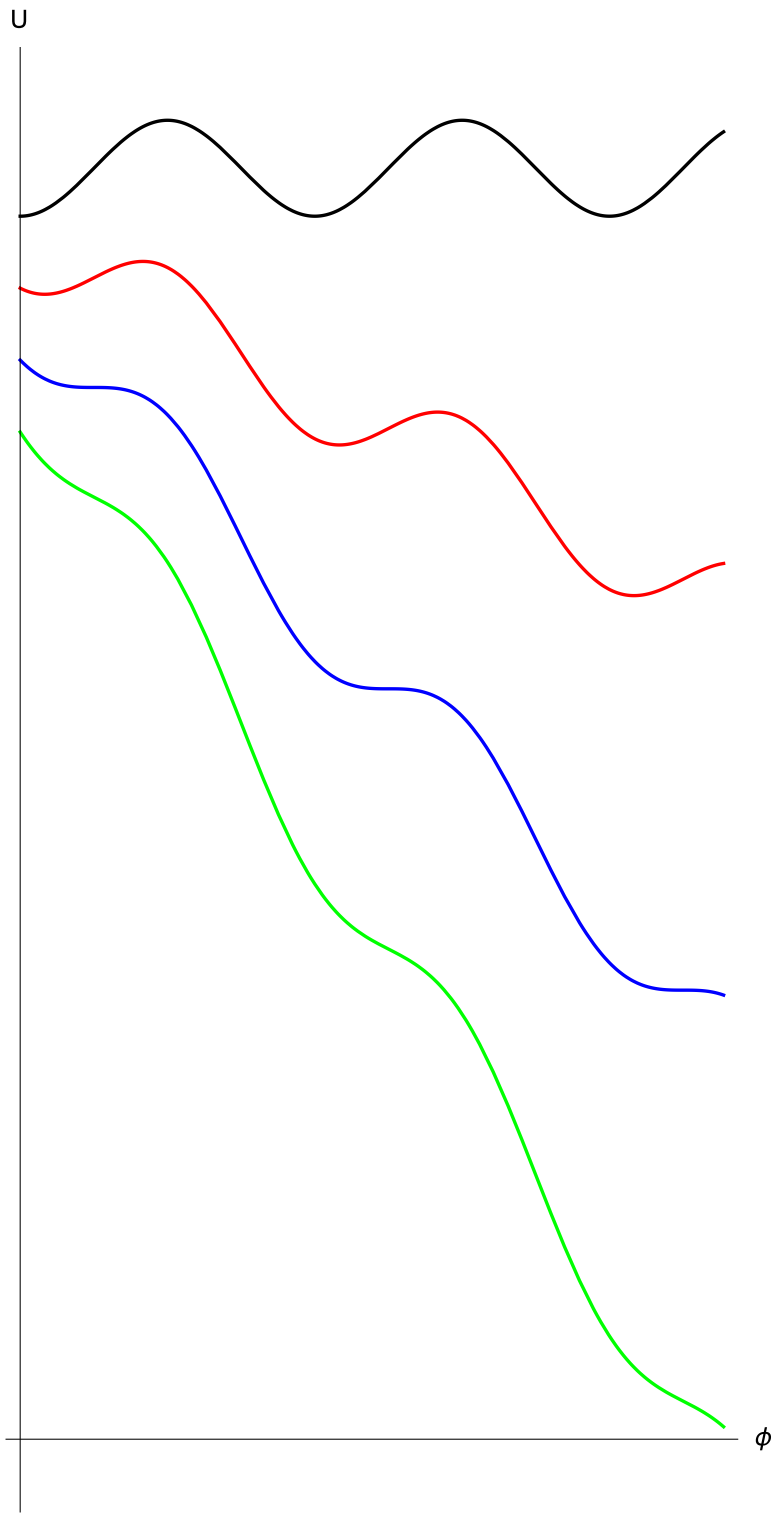

Figure 2.7 *Tilted washboard model.* A particle is trapped in the energy well when $I = 0$ (black curve) or $I < I_c$ (red curves). At $I = I_c$, the well flattens out and the particle can become unstable if given any energy (blue curve). With $I > I_c$ there are no stable states and the particle will slide along the well freely (green curve).

which we can rewrite as

$$\frac{d\varphi}{dt} = \frac{2\pi I_{c0} R}{\Phi_0}\left(\frac{I}{I_{c0}} - \sin\varphi\right). \tag{2.37}$$

For $I > I_{c0}$, $\frac{d\varphi}{dt}$ is always positive, meaning the phase is constantly changing. The size of this effect is periodic with $\sin\varphi$, winding slower if $\sin\varphi$ is positive and faster if it is negative [26]. According to Eqn 2.25, non-constant φ corresponds to an instantaneous voltage in the junction. If we integrate Eqn 2.37, we can find the time-averaged voltage as

$$|V| = R_N \cdot Re[(I^2 - I_{c0}^2)^{1/2}] \tag{2.38}$$

[26]. Here R_N is the normal-state resistance of the junction. If we look qualitatively at this equation, we see that it matches with the previously discussed phenomena of Josephson junctions. That is, when $|I| < I_{c0}$, V=0. However, very far from I_{c0} and thus far from superconducting, i.e. $|I| \gg I_{c0}$, the system responds as $V = IR$. This is plotted in Figure 2.8.

While Figure 2.8 is demonstrative of the ideal, $T = 0K$ case, measurements can sometimes exhibit thermal fluctuation effects. Thermal energy in the system could potentially excite the particle in the tilted washboard enough to escape the well before the current has reached I_{c0}. This will soften the jump at I_{c0} and round out the base of the curve, i.e. there is the possibility of measuring finite voltage below I_{c0} [43]. The I-V curve plotted in Figure 7.9b shows evidence of this rounding.

As it is mostly irrelevant to this work, I will only mention briefly the important characteristics of the underdamped RCSJ model. With an appreciable C (C> 1), the system exhibits signs of hysteresis. That is to say the current at which the system jumps from superconducting regime to that of the normal state (I_{c0}) is larger than that at which it

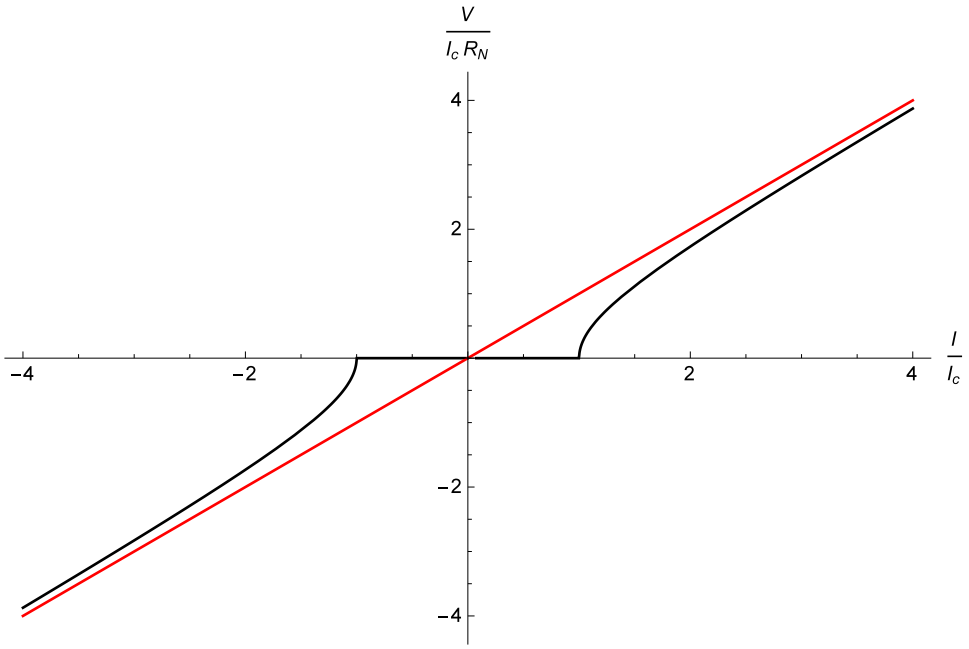

Figure 2.8 *Characteristic I-V curve for an overdamped Josephson junction.* The red curve indicates the Ohmic response for the same R_N.

goes from normal to superconducting, called the retrapping current ($I_{r0} \approx 4I_{c0}/\pi Q$) [26]. In the extreme case ($\beta_c \gg 1$), the current can be increased from $I = 0$ until it no longer superconducts ($I > I_{c0}$), but to return to its superconducting state, the current has to be decreased entirely to $I = 0$.

2.4.2 Fraunhofer Pattern

Data from this work is primarily concerned with the maximum critical current in our sample. As it will be discussed in Chapter 5, our measurement system is quite adept at measuring I-V curves. However, because there are ferromagnetic layers within our junctions, it is necessary to consider how Josephson junctions respond to a magnetic field.

Let us consider a Josephson junction with circular geometry (radius R), such as the one shown in Figure 2.9 and geometrically similar to those that were measured for this thesis. The material of the non-superconducting film between the two superconductors is not

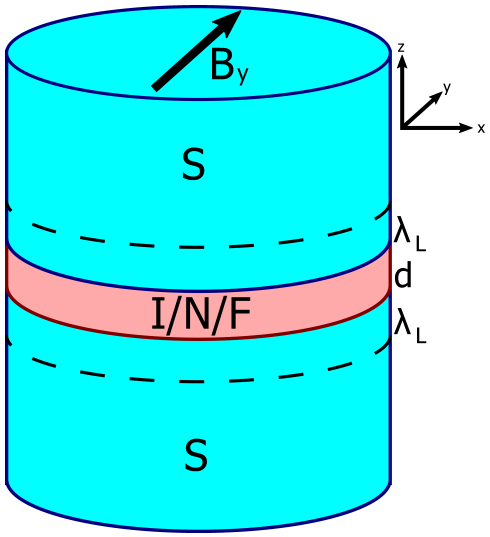

Figure 2.9 *Representation of a circular Josephson junction.* The dashed black lines represent the extent of the London penetration depth when the junction is in the presence of a magnetic field.

relevant, but let's consider it as a normal metal (N) in this example with a thickness d. In the presence of an external magnetic field with flux density and vector potential $\vec{B}_{ex} = (0, B_y, 0)$ and $\mathbf{A} = (0, 0, -B_y x)$, respectively, the superconductor will generate screening currents to suppress $\vec{B}_{ex}$, resulting in an internal field

$$B(z) = B_y \exp\left(-\frac{z}{\lambda_L}\right) \tag{2.39}$$

where

$$\lambda_L = \sqrt{\frac{m_e}{\mu_0 n_s e^2}} \tag{2.40}$$

is the London penetration depth, m_e and e are the mass and charge of an electron, respectively, μ_0 is the magnetic permeability constant, and n_s is the density of Cooper pairs [26]. The field inside N can be considered to be constant

$$B_N(z) = B_y. \tag{2.41}$$

Looking back at the gauge-invariant phase difference,

$$\varphi = \theta_2 - \theta_1 - \frac{2\pi}{\Phi_0} \int_1^2 \mathbf{A} \cdot d\vec{l} \tag{2.42}$$

we can find the phase difference across the junction as a function of position x as

$$\varphi(x) = \varphi_0 + \frac{2\pi}{\Phi_0} B_y x (2\lambda_L + d) \tag{2.43}$$

with a supercurrent density

$$J(x,y) = J_c(x,y) \sin\left(\frac{2\pi}{\Phi_0} B_y x (2\lambda_L + d) + \varphi_0\right). \tag{2.44}$$

In order to find the critical current, we must integrate over the entire junction, $I = \int\int J(x,y)dxdy$. For the circular geometry we have described,

$$I = 2J_c \int_{-R}^{R} \sqrt{R^2 - x^2} \sin\left(\frac{2\pi}{\Phi_0} B_y x (2\lambda_L + d) + \varphi_0\right) dx \tag{2.45}$$

after integrating over y. Maximizing Eqn. 2.45 with respect to φ_0 and integrating over x, we obtain

$$I_c = 2I_c(B=0) \left| \frac{J_1(\frac{\pi\Phi}{\Phi_0})}{\frac{\pi\Phi}{\Phi_0}} \right| \tag{2.46}$$

after completing the integration, where $I_c(B=0) = \pi J_c R^2$, J_1 is the Bessel function of first kind and order, and $\Phi = B_y 2R(2\lambda_L + d)$. This result is known as an Airy pattern and it is plotted in Figure 2.10. This result is for the case of a circular junction, but traditionally this is calculated for a rectangular junction, for which the result is called a Fraunhofer pattern.

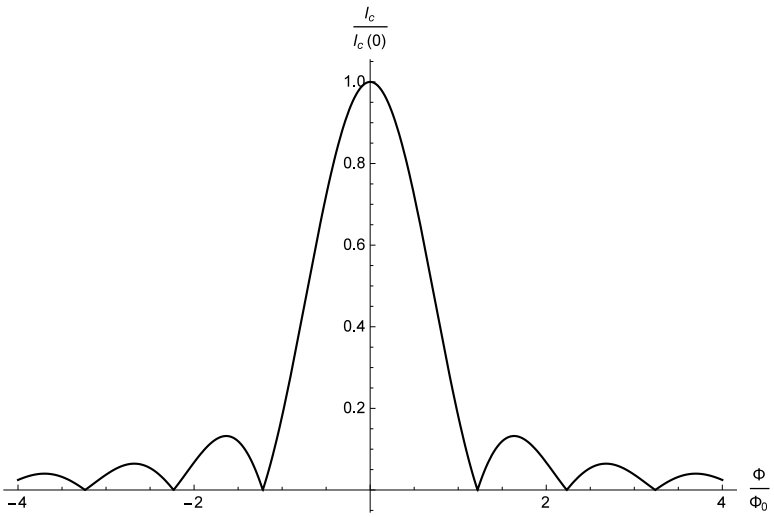

Figure 2.10 *Airy pattern.*

Throughout this thesis, the term "Fraunhofer pattern" is used in place of "Airy pattern" due to colloquialism, but I will note here that, technically, these are different functions.

2.5 Spin-Triplet Pair Correlations

As we saw in Section 2.3.2, the coherence length in S/F systems is very small, and thus any proximity effect should be very short ranged. Why, then, had 3 different groups reported evidence of long range proximity effect [44][45][46] orders of magnitude larger than expected in S/F systems? While the observed phenomena could be explained in part by surface and interface effects, the question remained largely unanswered until 2001 when two theoretical groups independently proposed a solution [47][48].

Electrons in spin-singlet Cooper pairs have opposite spin and will experience the effects of the band splitting when entering the ferromagnet, resulting in a short coherence length. If, however, the two electrons in the ferromagnet have the same spin, they would observe no band splitting and no effect from E_{ex}. To them, the ferromagnet would seem as if it were a normal metal system, and thus the coherence length would increase dramatically.

The surprising prediction of 2001 is that, in the presence of magnetic inhomogeneity in an S/F system, it is possible to generate long-range spin-triplet ($m_s = \pm 1$) pair correlations from the spin-singlet (m_s=0) Cooper pairs inside the superconductor. For clarity, the standard notation for these states are below, in the form $|s, m_s\rangle$.

$$\begin{aligned} |0,0\rangle &= \frac{1}{\sqrt{2}}\left(|\uparrow\downarrow\rangle - |\downarrow\uparrow\rangle\right) \\ |1,1\rangle &= |\uparrow\uparrow\rangle \\ |1,0\rangle &= \frac{1}{\sqrt{2}}\left(|\uparrow\downarrow\rangle + |\downarrow\uparrow\rangle\right) \\ |1,-1\rangle &= |\downarrow\downarrow\rangle \end{aligned} \tag{2.47}$$

It is possible to observe this effect in samples with intrinsic inhomogeneity, such as through domain walls [49] or spiral magnetization [50]. However, controlling the inhomogeneity extrinsically [51] has proven far more reproducible, and as it is the method used in this work, it will be the focus of this discussion. It can be achieved from well-engineered structures with multiple, non-collinear ferromagnetic layers ($F_1, F_2, ...$).

The formal approach to demonstrate the ability to create $|1,1\rangle$ or $|1,-1\rangle$ triplet components is quite complex and heavily reliant on Green's functions. Thankfully, Matthias Eschrig developed a simpler, albeit less-rigorous, explanation which will be followed here [52][53]. (For reference, Figure 2.11 depicts the system utilized in this discussion.) In this example, the second ferromagnet has its magnetization direction rotated θ relative to the first.

As stated previously, Cooper pairs inside the superconductor are spin-singlet, $|0,0\rangle$. When a Cooper pair passes from S to F_1, due to the exchange energy of the ferromagnet, the pair correlation will pick up a center of mass momentum shift, $Q = k_\uparrow - k_\downarrow$ and

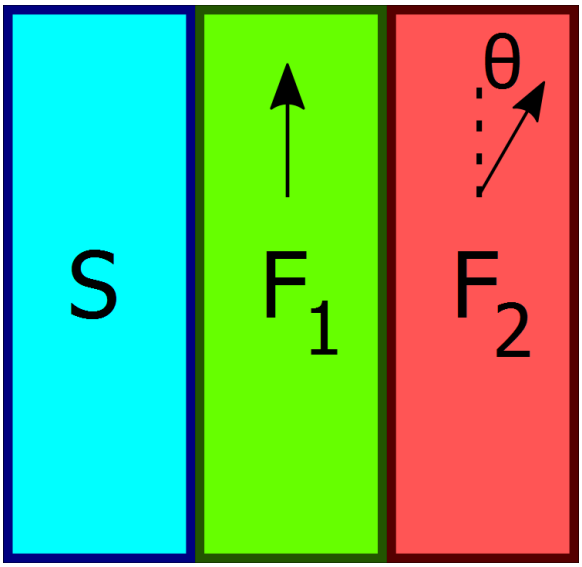

Figure 2.11 *Structure for spin-triplet generation.* The effect is only realized for $\theta \neq n\pi$.

evolve to

$$\begin{aligned} |\psi\rangle_1 &= \frac{1}{\sqrt{2}}\left[\exp\left(\frac{iQx}{\hbar}\right)|\uparrow,\downarrow\rangle - \exp\left(\frac{-iQx}{\hbar}\right)|\downarrow,\uparrow\rangle\right] \\ &= \cos Qx\,|0,0\rangle_{F_1} + i\sin Qx\,|1,0\rangle_{F_1} \end{aligned} \tag{2.48}$$

which includes both spin-singlet as well as a short-range spin-triplet pair correlations.

As this ensemble enters the second ferromagnet the spin-singlet correlations will evolve in the same way as above, yielding no long-range components. Therefore, we will ignore their contribution from here out. However, assuming that F_1 is thin enough that the short-range spin-triplet pair correlations haven't fully decayed, the $|1,0\rangle$ component will undergo a traditional basis rotation at the F_2 interface, resulting in

$$|1,0\rangle_{F_1} = \frac{\sin\theta}{\sqrt{2}}|1,1\rangle_{F_2} + \cos\theta\,|1,0\rangle_{F_2} - \frac{\sin\theta}{\sqrt{2}}|1,-1\rangle_{F_2}\,. \tag{2.49}$$

Having generated components of parallel spin, pair correlations with $|m| = 1$ represent

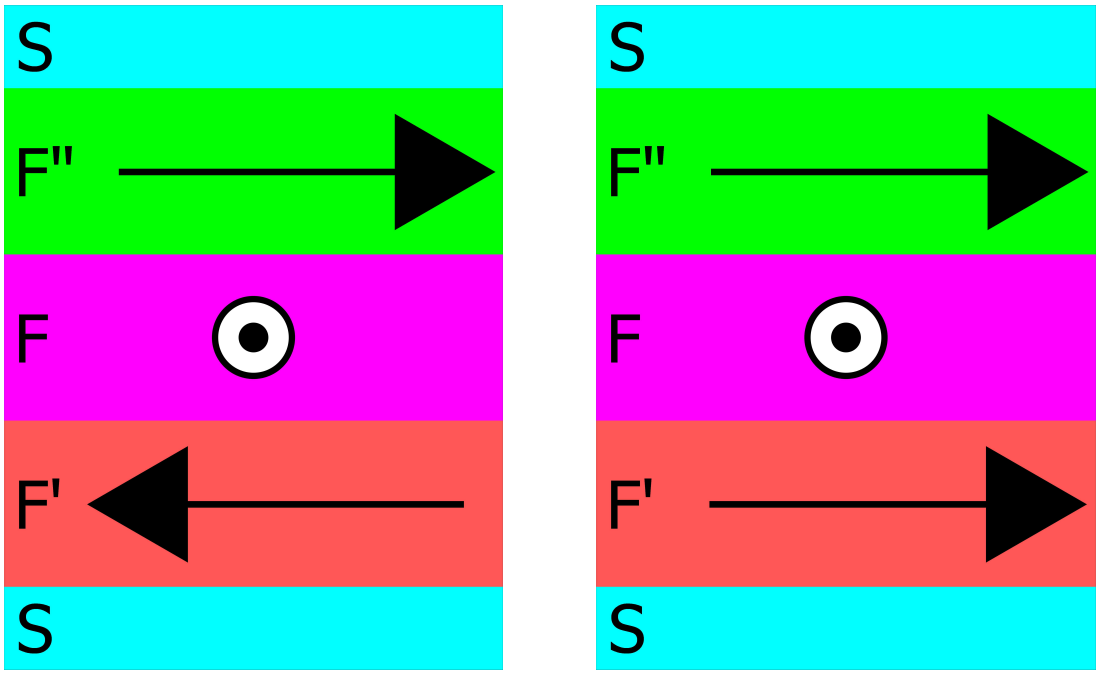

(a) 0-junction (b) π-junction

Figure 2.12 *Triplet junction phase cartoon.* The magnetization of each layer is depicted by conventional representations. The relative rotation of the magnetization direction between adjacent magnetic layers will determine the phase of the junction. A 0-junction will maintain rotation direction while a π-junction will switch rotation directions.

two electrons in the same spin band in F_2. In this way, as long as they maintain their spin, these pairs act the same in a ferromagnet as they would in a normal metal, increasing the coherence length dramatically.

In order to detect these long-range spin-triplet components effectively, we rely on measuring the Josephson characteristics, which requires us to place another superconductor after F_2. However, the superconductor can only carry spin-singlet Cooper pairs. Due to the rapid decay of both the $|0,0\rangle$ and the $|1,0\rangle$ components, there will be no more pair correlations that can rotate back to spin-singlet at the F_2/S interface. Therefore, before capping the junction with the final superconductor, one more ferromagnet layer (F_3) must be added. This final ferromagnetic layer will provide another basis rotation, once again generating some $|1,0\rangle$ components that can evolve back to spin-singlet Cooper pairs at the S interface.

Spin-triplet Josephson junction samples, therefore, have an S/F_1/F_2/F_3/S structure (often written herein as S/F'/F/F"/S), as predicted by theorists in 2007 [54]. Based on the chirality of rotation of magnetization direction of adjacent magnetic layers within, these junctions are said to have either a 0 or π spin-triplet phase. If the direction of rotation between F' and F is the same as that for F and F", the system is in a 0-state. If the rotation changes direction, the system is in a π-state. This is demonstrated in Figure 2.12.

In addition to the phase, the ability to turn on or off the spin-triplet generation mechanism also exists as a function of magnetization direction. If any two neighboring F layers have collinear magnetization, the long range terms, with an amplitude proportional to $\sin\theta$, are not generated and only the standard spin-singlet decay can be observed. However, if all neighboring layers have non-collinear magnetization, it is theoretically possible to realize a critical current enhancement of several orders of magnitude relative to that found in traditional S/F/S junctions with comparable thicknesses. As shown in Eqn 2.49, the $m_s = \pm 1$ pair correlations are maximally generated with orthogonal magnetization, minimally with parallel magnetization. Therefore, through manipulation of the relative magnetization angle between neighboring ferromagnetic layers, it should be possible to control the size of the critical current measured in S/F_1/F_2/F_3/S Josephson junctions, which follows

$$I_c \propto \sin\theta \sin\varphi \tag{2.50}$$

where θ is the angle between F_1 and F and φ is the angle between F and F_2. It is this realization, the ability to turn the critical current "on" and "off" by manipulating the magnetization direction of individual ferromagnetic layers, that motivates the work undertaken in this dissertation.

Chapter 3

Relevant Previous Work

There has been a lot of experimental work done in the spin-triplet supercurrent field since its discovery, and to ignore that would belie its importance herein. The work that is directly relevant to this thesis will be discussed in this chapter.

3.1 Initial Evidence of Spin-Triplet Pair Correlations in S/F Systems

As mentioned in the previous chapter, in the late 1990s, three different groups reported large decreases of the resistance in ferromagnetic wires attached to a superconducting electrode [44][45][46]. The size of the proximity effect in each publication was much larger than one would expect in S/F systems, and the groups claimed these results as evidence of long-range proximity effect which had no theoretical understanding at the time.

After the theoretical predictions of 2001, several groups reported evidence of supercurrent in wide ferromagnetic barrier Josephson junctions in 2006. One group made Josephson junctions on CrO_2 [55]. Being a half-metallic ferromagnet, CrO_2 is completely spin-polarized. Therefore, no spin-singlet supercurrent should be observable, and any supercurrent must arise from long-range spin-triplet pair correlations. A second group fabricated "Andreev interferometers" with Ho as a ferromagnetic wire [56]. They measured the resistance of

the Ho as a function of superconducting phase difference of the electrodes and observed modulations, claiming this was a result of long-range spin-triplet correlations in the Ho. Ho is a conical ferromagnet, so the necessary magnetic inhomogeneity occurs internally as the magnetization spirals in the direction of electron propagation.

Despite these results, the acceptance of long-range spin-triplet correlations in S/F systems had yet to be fully appreciated. In the proximity effect measurements of the 90s, too many parameters were still unaccounted for, including the change of resistance at the S/F interface. In the S/F/S experiments, neither group could control the inhomogeneity present in their system, the source of the spin-triplet components propagating through their junctions. This was a large concern, especially for the group working with CrO_2, who saw sample-to-sample variations in critical current of up to two orders of magnitude.

3.2 Reproducible Generation of the Spin-Triplet Supercurrent

Prior to 2010, skeptics within the community remained concerned by the lack of reproducible and concrete evidence supporting long-range pair correlations. With hopes of realizing a reliable method to generate spin-triplet components, Trupti Khaire and Mazin Khasawneh, members of our group, grew S/F'/F/F"/S Josephson junctions [57][58] (Figure 3.1), relying on the extrinsic magnetic inhomogeneity of multiple ferromagnetic layers [54] (see Section 2.5). (In this thesis, F' and F" are also referred to as the "spin-mixer" layer.)

Data from these experiments, summarized in Figure 3.2, clearly demonstrate the emergence of spin-triplet supercurrent. In this figure, samples without an F' layer were measured to demonstrate the typical decay of the spin-singlet in S/F/S Josephson junctions. However,

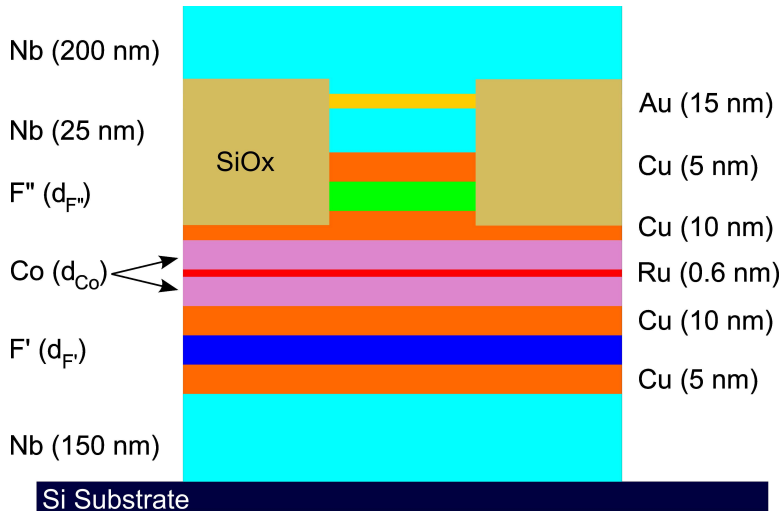

Figure 3.1 *Spin-triplet pillar schematic.* F' and F" are the spin-mixer layers, initially a weak ferromagnetic alloy (PdNi or CuNi). Layer thickness not to scale. Figure adapted from [57]

when fabricated with PdNi(4 nm) as the spin-mixing layer, the critical current became much larger, surpassing two orders of magnitude for a total Co thickness of 20 nm (Figure 3.2).

Work started by Trupti Khaire and continued by Caroline Klose and Yixing Wang demonstrated an enhanced supercurrent in similar S/F'/F/F"/S Josephson junctions to the one in Figure 3.1 by magnetizing them in large external magnetic fields. Any flux that may be trapped in the Nb was removed by raising the temperature of the sample above the critical temperature (T_c) of Nb before measuring the Fraunhofer pattern. This effect can be seen in references [59] and [61]. In the data, not only has the size of the critical current been enhanced, but the Fraunhofer pattern has also become more pronounced. In some samples, magnetizing the junction before measurement demonstrated a 20-fold increase in the critical current [59].

This enhancement is due to the organized domain structure that emerges after magnetization, as demonstrated in Figure 3.3. Because these junctions have large areas, they have multiple domains within the pillar, each pointing in it's own direction (a). The domains can be organized by applying a large magnetic field (b), which will align them parallel to the

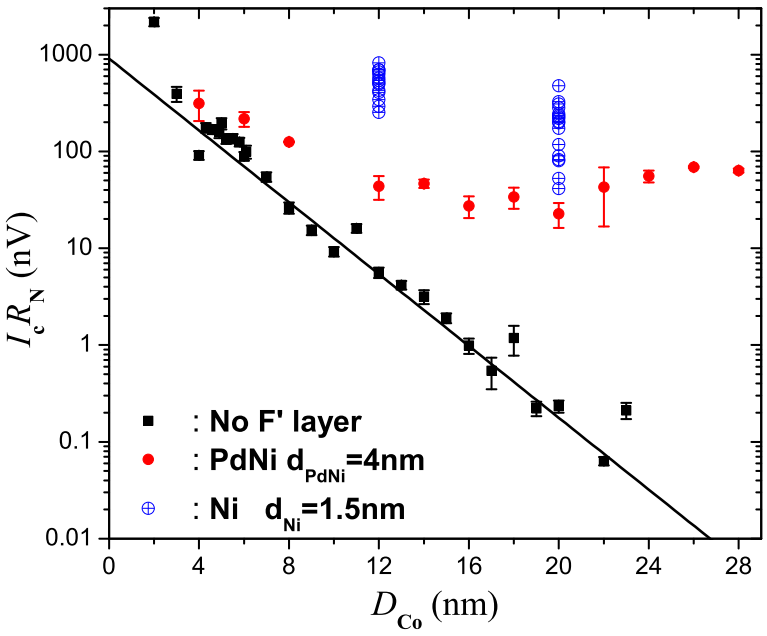

Figure 3.2 *Plot of initial spin-triplet emergence.* The x-axis, D_{Co}, represents the total thickness of Co in the SAF ($D_{Co} = 2d_{Co}$). The black curve is without an F' layer, so measures the typical decay in an S/F/S Josephson junction. The red and blue curves show enhanced I_cR_N that results from generation of spin-triplet components. The blue curve has also been magnetized for more enhancement. The black, red, and blue points were taken by Mazin Khasawneh [57], Trupti Khaire [57], and Yixing Wang [60], respectively.

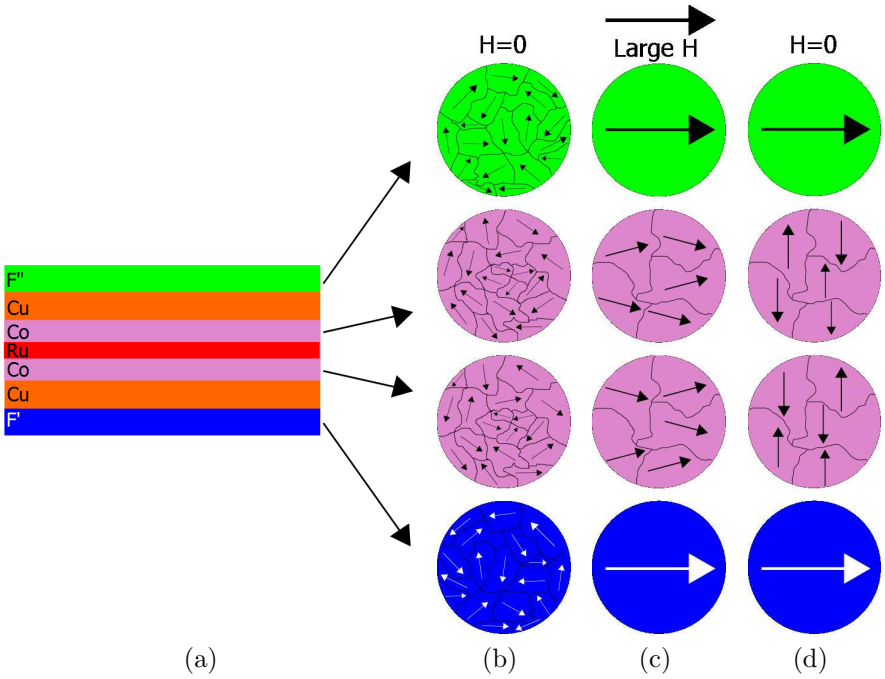

Figure 3.3 *Schematic of layer magnetization.* Initially, domains will point randomly throughout each layer (b). Applying a large field will cause all domains to (mostly) align to it (c). When removed, the spin-mixer domains magnetization will remain parallel to the field while the SAF will spin flop perpendicular to it (d). This organization of the domains gives rise to the enhancement of spin-triplet critical current.

field. Therefore, when the field is removed (c), the spin-mixer layers will remain aligned in this direction, but the Co/Ru/Co will spin-flop perpendicular to them (see Section 6.2 for more information on the spin-flop mechanism).

As mentioned in Section 2.5, S/F'/F/F"/S Josephson junctions will have an overall phase related to the chirality of magnetization directions between adjacent ferromagnetic layers. In the unmagnetized state, the system initializes as a mixture of 0 and π phases. However, after magnetizing, the system fully enters a π phase, enhancing the critical current. Beyond aligning the layers from a random orientation, magnetizing the sample also causes each adjacent layer to have orthogonal magnetization, the optimal situation for long-range spin-triplet generation (as was discussed in Section 2.5).

3.3 Characterization of Spin-Mixer Layers

It is necessary to thoroughly characterize each ferromagnetic layer, and original work done to accomplish this is discussed in Section 6. However, two ferromagnetic materials that were used in this project, Ni and NiFeMo, were characterized by previous group members, and will be discussed in this section.

3.3.1 Ni

3.3.1.1 Generation

When our group started fabricating Josephson junctions that demonstrated spin-triplet supercurrent, Ni was one of the first materials used as a spin-mixer. As such, its ability to generate spin-triplet pair correlations had been optimized early on by Caroline Klose [59] and Yixing Wang [61]. The blue points in Figure 3.2 plot the critical current measured in samples fabricated with Ni as a spin-mixer layer, which demonstrates the increased critical current when compared to samples made without a spin-mixer layer (black points). In magnetized samples, this enhancement was maximized for Ni thicknesses about 1.0-1.5 nm [62].

3.3.1.2 Switch Field

As mentioned in Section 3.2, an enhancement of the critical current in spin-triplet-supercurrent samples has been observed by magnetizing them before measurement. The onset of this effect required magnetic fields with magnitudes of 50-100 mT, depending on thickness. Samples with thicknesses of 1.0 and 1.5 nm, close to the 1.2 nm Ni thickness used in this

work, demonstrated supercurrent enhancement starting at ≈100 mT.

Ni samples were also fabricated and measured in a Quantum Design DC SQUID Magnetometer, a measurement device which is capable of measuring M vs H curves similar to the one demonstrated in Figure 2.1. These data are plotted in Figure 3.4 for Ni thicknesses of 1.0 and 1.5 nm [62]. To obtain approximately the same total magnetization between samples, multiple Ni layers are deposited in each sample, separated by Cu buffer layers. From these data we can determine that the coercive field for 1.2 nm Ni, which will fall between that of 1.0 and 1.5 nm samples, is between 40-60 mT.

Additionally, the magnetic field required to demagnetize spin-triplet-supercurrent samples has been measured [61]. After magnetizing the samples in a positive magnetic field, incrementally larger negative fields were applied, measuring the critical current after each iteration. The data suggest that 1.5 nm Ni requires ≈60 mT to demagnetize.

Measured three separate ways, these experiments demonstrate the hardness of Ni when used as a thin spin-mixer layer. All measurements suggest that it takes at least 40 mT to demagnetize Ni, a field much larger than that the one that is required to rotate the magnetization of softer layers.

3.3.2 NiFeMo

Because my work relies on rotation of magnetic layers, softer ferromagnets than Ni or Co were sought. One option for a softer ferromagnet was NiFeMo, a material that group-member Bethany Niedzielski had been working with at the time.

Similar to the pair correlation of S/F systems discussed in Section 2.3.2, S/F/S Josephson junctions will either be considered a 0 or a π junction [63], an effect of the oscillating nature of the pair correlation wavefunction in S/F systems (Figure 2.4b). Control of junction phase

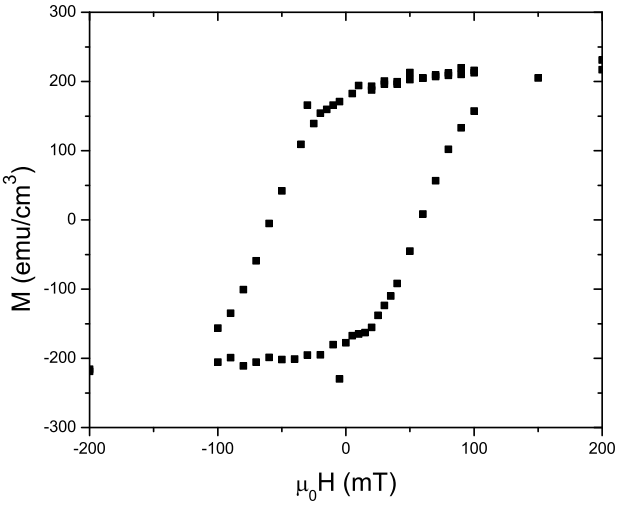

(a) $d_{Ni} = 1.0$ nm

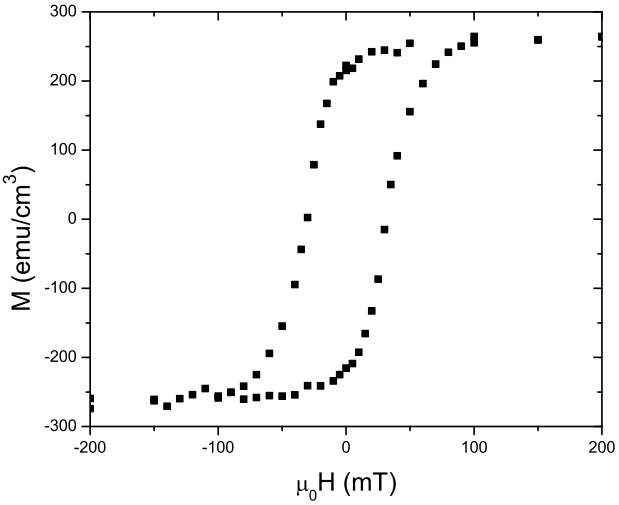

(b) $d_{Ni} = 1.5$ nm

Figure 3.4 *Ni DC SQUID Magnetometer data.* Ni layer thickness labeled for each plot. Layers were repeated to maintain approximate total magnetization between samples. $H_c \approx$60, 40 mT for Ni thickness 1.0, 1.5 nm, respectively. Data taken by Caroline Klose [62].

can also be done in S/F'/F/F"/S triplet-junctions due to the chirality of rotation of the magnetization layers (see Section 2.5). This bi-modality can be quite useful in memory applications [64], and determining reliable control of spin-singlet and spin-triplet Josephson junctions was the initial goal of Bethany's work.

Although our motivations were different, many of the results from her work were incorporated in the onset of this project, especially regarding NiFeMo as a spin-mixer layer.

3.3.2.1 Generation

To determine the ability of NiFeMo to generate spin-triplet supercurrent, samples were fabricated consisting of Nb(150)/Cu(5)/Ni(1.2)/Cu(10)/Co(6)/Ru(0.75)/Co(6)/Cu(10)/ NiFeMo(x)/Cu(5)/Nb(20)/Au(15)/Nb(150)/Au(10), where x varied from 0.8-2.4 nm (as well as samples with 0 nm NiFeMo to use as a control). These were large area, circular junctions with diameters measuring between 3 and 48 μm. These samples underwent the typical Fraunhofer pattern measurement, an example of such a pattern can be found in Figure 3.5. In this case, Ni was left as the other spin-mixer as its optimal thickness to generate triplet supercurrent had already been measured.

For these measurements, the size of the critical current is not as relevant as the $I_c R_N$. I_c scales proportionally with area while R_N scales inversely. Therefore, this product yields a characteristic parameter for a Josephson junction dependent only on the materials used and should account for sample-to-sample variations in things like area and resistance differences. The I_c for each run is taken as the maximum value of the Fraunhofer pattern, while R_N can be determined as the slope the I-V curve asymptotically approaches far from the supercurrent regime. To obtain a more accurate value, this slope is generally determined from an I-V curve with very small critical current, often at high field to suppress the critical current as much

as possible.

The I_cR_N product is plotted against NiFeMo thickness in Figure 3.6 [65]. As NiFeMo gets thicker, the supercurrent is suppressed in the same way it would be in a typical S/F/S Josephson junction. Therefore we see a linear decay on a log-linear plot. For very thin samples, we also see a decrease in I_cR_N. We can see from Eqn 2.48 that the amount of $|1,0\rangle$ pair correlations generated is proportional to $\sin Qx$. Therefore, the spin-mixer layer cannot be too thin, as the long-range triplet components are generated from the $|1,0\rangle$ pair correlations. The peak of Figure 3.6 is determined to be the ideal thickness of NiFeMo for generating spin-triplet. In this case, NiFeMo is optimally about 1.0 nm thick.

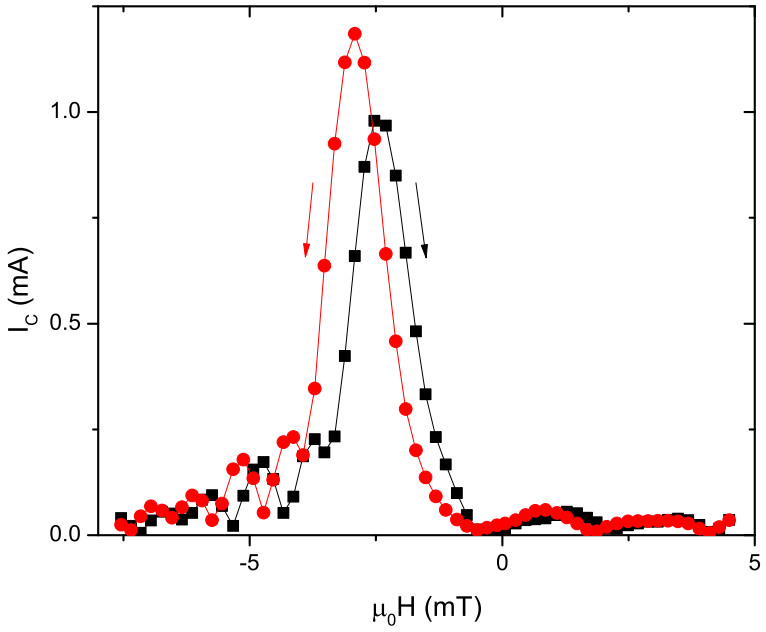

Figure 3.5 *Example of Fraunhofer pattern for NiFeMo generation samples.* The black and red curves indicate measurements taken with different sweep directions, as depicted by arrows. Sample composition: Nb(150)/Cu(5)/Ni(1.2)/Cu(10)/Co(6)/Ru(0.75)/Co(6)/Cu(10)/NiFeMo(0.8)/Cu(5)/ Nb(20)/Au(15)/Nb(150)/Au(10) [65].

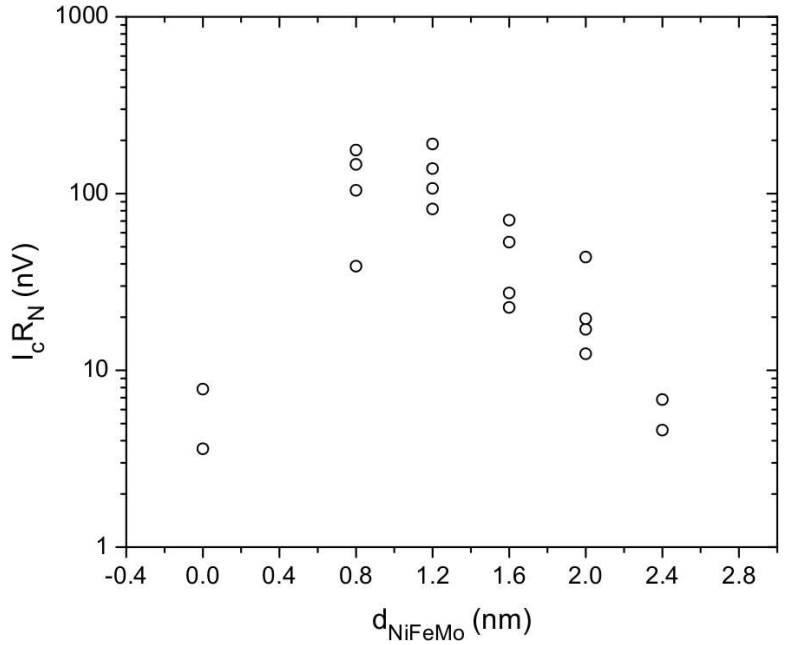

Figure 3.6 *I_cR_N vs NiFeMo Thickness.* The maximum I_cR_N for each sample is labeled as a point, and multiple samples were measured for each thickness. Sample composition: Nb(150)/Cu(5)/Ni(1.2)/Cu(10)/Co(6)/Ru(0.75)/Co(6)/Cu(10)/NiFeMo(x)/Cu(5)/ Nb(20)/Au(15)/Nb(150)/Au(10), 0.8 nm $\leq$ x $\leq$ 2.4 nm [65].

3.3.2.2 Switching Field

For the work she was doing, Bethany's project involving NiFeMo moved away from spin-triplet and into spin-singlet samples, which consisted of Josephson junctions with a single ferromagnetic layer. In order to better confine the direction of magnetization, these samples were made with an elliptical geometry. The ellipse, which is patterned with aspect ratio of 2.5 and total area of 0.5 μm^2, is small enough to be single domain. This should make the 180-degree switch in magnetization direction very abrupt, while the aspect ratio creates a shape anisotropy that confines the magnetization direction along the long axis. An example of these ellipses and their magnetization can be seen in Figure 3.7.

Still interested in the maximum critical current, Fraunhofer patterns were measured for these elliptical single-layer samples. An example of such a sample can be seen in Figure

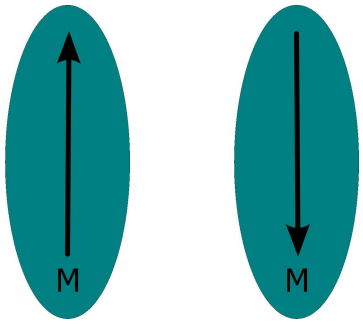

Figure 3.7 *Ellipse pattern geometry.* Due to the small size, the elliptical pillars are single domain, with magnetization pointing along the long axis due to shape anisotropy.

3.8 [66]. Critical current measurements at the same field in the positive and negative sweep direction do not overlap the whole time due to the change of NiFeMo magnetization direction. Depending on how the magnetization is aligned, the flux through the junction changes direction, resulting in a shift in the central peak of the pattern. The shift alternates between positive and negative fields, depending on the direction of the magnetization (blue and red curves, respectively). We can see that measurements of both sweep directions overlap when the magnitude of the field is greater than 5 mT, implying that the NiFeMo magnetization direction is the same for those fields. These data inform us that the field required to flip NiFeMo magnetization 180 degrees is about 5 mT. Looking forward, rotation of a circularly patterned NiFeMo pillar should require no more than 5 mT as well, at least for single magnetic-layer junctions.

3.4 External Work

While our group has reported a lot of interesting work in this field, we are not the only ones looking at spin-triplet supercurrent and the research possibilities therein, nor are we the only group looking at rotation of layers. For example, quite a bit of work is being done

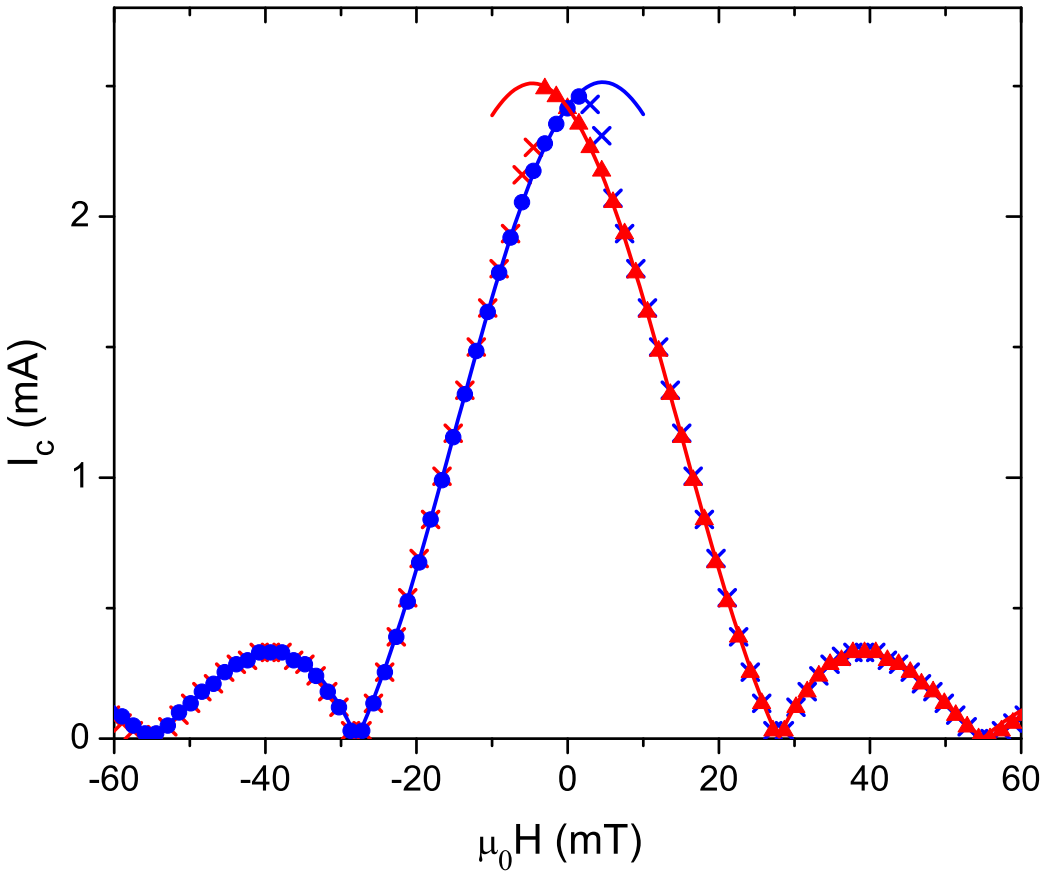

Figure 3.8 *NiFeMo Switching Field.* When Fraunhofer patterns overlap, NiFeMo is pointing in the same direction for each sweep. The magnetization points in the opposite direction in regions where the patterns deviate. The switching field, that which flips the NiFeMo so that both magnetizations point the same direction, is that which brings the patterns back together. This occurs at about 5 mT in this singlet sample. Data taken by Bethany Niedzielski [66].

investigating the effects of magnetization direction on superconducting critical temperature.

3.4.1 Spin-Triplet Josephson Junctions

Shortly after the initial reporting of spin-triplet supercurrent observations in S/F'/F/F"/S Josephson junctions (as discussed in Section 3.2 above), several other groups reported phenomenologically similar results. Using Ho as a spin-mixer layer, one group measured junctions with Ho/Co/Ho which demonstrated a large enhancement in critical current, with little decay as the Co thickness increased [67]. They also were able to show that this effect was dependent on the thickness of Ho, a result caused by the spiral magnetization of Ho. Another group used the Heusler alloy Cu_2MnAl in S/I/F/S Josephson junctions and demonstrated an increase in critical current for certain thicknesses [68]. Starting at 7 nm Cu_2MnAl, the critical current decay rate changes dramatically, almost plateauing. This is due to an inhomogeneous magnetization at the interface between the alloy and adjacent materials. However, with thicknesses above 10.3 nm, the strength of the field becomes too great and the interfaces no longer maintain inhomogeneity, causing the critical current to fall back to sizes reminiscent of singlet decay.

Two more groups demonstrated long-range supercurrent in S/F/S Josephson junctions. In one experiment, superconducting electrodes were deposited on single crystal Co wires via focused ion-beam (FIB) deposition [69]. In the other, CrO_2 samples were fabricated on various substrates [70], similar to the work done in [55]. Although these materials and geometries have no characteristic magnetic inhomogeneity, the fabrication procedure for each requires rather aggressive etching techniques, especially FIB. It is presumed that, while creating a clean interface between materials, these techniques can also damage the surface of the magnet, creating inhomogeneous magnetization at the interface.

All of these results were remarkable evidence that magnetic inhomogeneity, regardless of whether it emerges extrinsically, intrinsically, or at the interface, will generate spin-triplet pair correlations, bolstering the theoretical claims made almost a decade prior.

3.4.2 Rotating Magnetization in Pseudo Spin Valves

Theoretically, S/F/F' pseudo spin valves with an S layer thinner than the BCS coherence length can demonstrate a change in critical temperature (T_c) dependent on the relative magnetization of the two ferromagnetic layers [71]. As the angle between the two magnetization directions increases from 0 to 90 degrees, the efficiency of spin-triplet generation increases, allowing for more supercurrent to leak into the F layers. This additional channel for pair leakage decreases the critical temperature of the superconductor.

This effect was first reported experimentally in 2012 with a $\Delta T_c = T_c(90^\circ) - T_c(0^\circ)$ of -50 mK [72]. Several other groups reported similar results [73][74], with $\Delta T_c = -120$ mK being the largest at the time [75]. Recently, a group measured $|\Delta T_c| > 1$ K [76], by far the largest effect reported at the time of writing this thesis.

3.4.3 Field Dependent Spin-Triplet Amplitude Modulation

More directly related to the project described in this thesis is work being done by the Blamire group at the University of Cambridge [77]. They are also hoping to manipulate the spin-triplet supercurrent by rotating magnetic fields and recently published some work demonstrating that phenomena. However, it differs greatly from the work described in the rest of this thesis in some important areas; one very notable difference is that they are only able to see the effect as they sweep the external magnetic field. This means that,

in the presence of no external field, they are not able to measure both states, spin-triplet supercurrent on and off.

Samples are fabricated with rectangular geometry, using Permalloy (Py), a NiFe alloy consisting of 80% Ni and 20% Fe, as their spin-mixer layer and Co as their central ferromagnet [Nb(250)/Cu(5)/Py(1.5)/Cu(5)/Co(5.5)/Cu(5)/Py(1.5)/Cu(5)/Nb(250)] (Figure 3.9). The magnetizations of Co and Py will align collinearly in a large magnetic field. Therefore, at those fields, the critical current is entirely short ranged and immeasurable in their system.

The key to generating spin-triplet generation in these samples is that the magnetization of the Py layers and Co layer rotate at different thresholds. Therefore, by sweeping from large positive to negative field, the rotation of the Py relative to Co will create a non-collinearity, generating spin-triplet supercurrent. Because of this they are able to detect an increase in critical current at certain field values. To validate their claims, they were able to mimic their data (Figure 3.10a) through the use of micromagnetic simulations (Figure 3.10b). They also simulated the magnetization of each magnetic layer as the field was swept, which is demonstrated in Figure 3.10c.

While this enhanced critical current can be held as long as the external field remains, any changes to the field will continue to rotate the magnetization, potentially removing the non-collinearity and diminishing the effect of spin-triplet supercurrent. To reset the magnetizations and recover the spin-triplet, a large field needs to once again be applied and swept back to the field where the magnetizations become maximally unaligned. Unfortunately, this does not occur at the remnant (zero-field) state, and thus the system is not bi-modal unless in the presence of a specific external field.

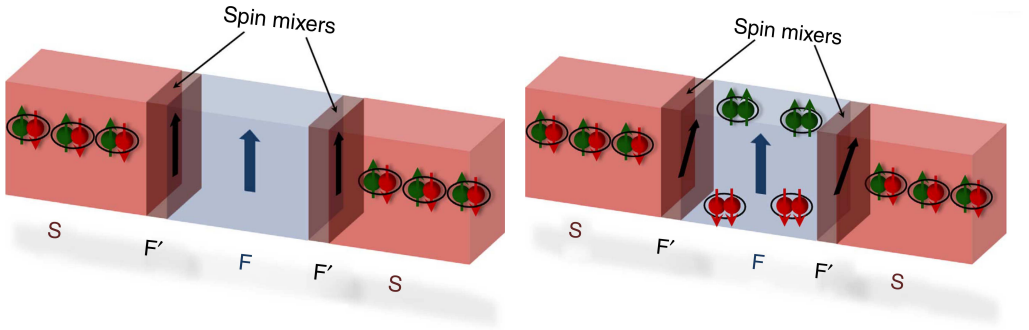

(a) (b)

Figure 3.9 *Junction used by the Blamire group* [77]. In (a), all magnetization directions are aligned and therefore no critical current is observed. In (b), the F' layers rotate relative to F, thus creating a spin-triplet supercurrent to pass through the F layer. Adapted by permission from Macmillan Publishers Ltd: *Nature Communications* **5**, 4771, copyright 2014. [Available online – http://www.nature.com/nature]

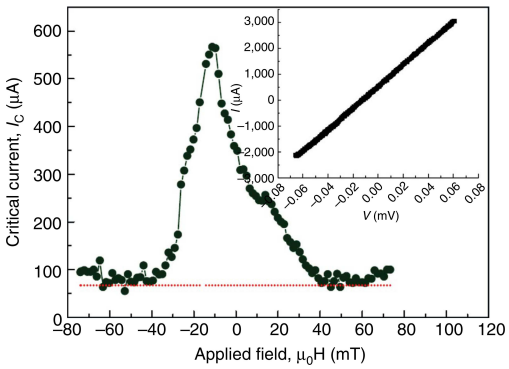

(a) Fraunhofer pattern the Blamire group measured as it swept from positive to negative field. Offset from zero, shown by the dotted line, artifact of measurement system, as shown to have zeo critical current for some fields (inset).

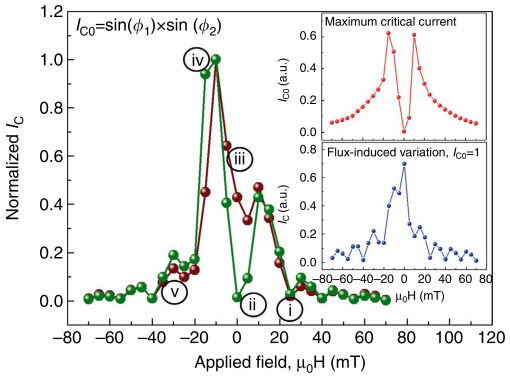

(b) Simulations of expected critical current with this sample geometry. Green curve accounts for sign of $\sin\phi_1 \sin\phi_2$ (ϕ is the relative magnetization angle for neighboring magnetic layers).

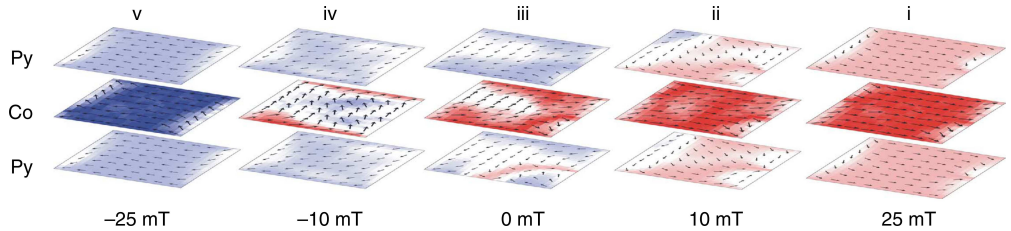

(c) Magnetic simulations of individual layer magnetization at various moments of the Fraunhofer pattern sweep. (i-v indicate the moment indicated in (b).). In both i and v, the field is enough to rotate all magnetizations co-linear. However, in the process of rotating, certain moments have non-colinearity.

Figure 3.10 *Data taken and simulations run by the Blamire group* [77]. Adapted by permission from Macmillan Publishers Ltd: *Nature Communications* **5**, 4771, copyright 2014. [Available online – http://www.nature.com/nature]

3.5 Additional Background Information

While the previous work mentioned above covers a fair amount of the work relevant to this thesis, it should come as no surprise that it is merely the tip of the iceberg when it comes to S/F systems, spin-triplet pair correlations, and efforts to rotate magnetization. If more information is desired, three recent review articles have been recently published to which I direct the reader [78][79][11].

Chapter 4

Sample Fabrication

To investigate the phenomena discussed in this work, micro- and nano-scale devices must be fabricated and measured. This requires the use of sophisticated equipment and time to optimize the process. In this chapter, I will describe the equipment used and the resulting process developed in order to fabricate samples.

4.1 Fabrication Equipment

The equipment used to fabricate our samples and optimize the fabrication process will be discussed in this section, and will be structured in roughly the same order as fabrication takes place: lithography techniques will be discussed in Section 4.1.1; material deposition and milling techniques will follow in Section 4.1.2; microscopy techniques used to characterize issues and optimize the process will conclude the discussion in Section 4.1.3.

4.1.1 Lithography

In this section I will discuss both photo-, or optical, lithography (Section 4.1.1.1) as well as electron beam lithography (EBL) (Section 4.1.1.2). While the equipment is very different, the basic principle is the same. Lithography is a process that utilizes polymers, called resist, that react in one of two ways: positively or negatively. A positive resist is one that will develop if exposed to light; negative resist develops unless it is exposed. After exposing only

the desired pattern, the unwanted resist can be developed away, leaving room to deposit material, as discussed in Section 4.1.2. The lithography process is a way to make a stencil with very fine features.

4.1.1.1 Photolithography

Photolithography is a very common, efficient, and reliable technique in sample fabrication, using UV light to react with a photo-sensitive resist, typically S1813. We use an ABM Mask Aligner that emits UV and deep UV (405 nm and 365 nm light, respectively). With this lithographer, we can make features down to $\sim 3\mu m$. Features finer than this will be discussed in the following section.

To expose a specific pattern, it must first be created on a photomask which is typically a piece of glass with a chrome plate on one side. The chrome plate is cut into a desired pattern that will allow light to pass through, exposing the resist below to the UV light and transferring features. Because these plates are made from durable chrome-on-glass, they reliably reproduce the same pattern for each exposure.

A chip or wafer is placed and aligned below the mask. Often alignment requires no more than visual inspection to make sure the substrate is under the pattern. However, when it becomes important (as in Section 4.2.4), the aligner has an optical microscope with up to 20x magnification that can be used to determine proper alignment.

After the substrate is aligned, it is brought into contact with the mask to reduce the amount of diffracted light distorting fine features. Proper contact can be determined by seeing a thin film interference pattern in the resist, visible through the open areas of the mask. Only now is the substrate ready to be exposed, which is timed automatically as defined by the user, about 10-12 seconds for this work. After exposure, the substrates are

ready to undergo development to remove unwanted resist, leaving only the desired pattern.

4.1.1.2 Electron Beam Lithography

Despite taking quite a bit more time, there are multiple advantages to using electron beam lithography instead of optical lithography. Firstly, line widths as narrow as 50 nm can be resolved in EBL systems, allowing for much finer patterns to be fabricated. Also, EBL patterns are designed in CAD software, meaning that, unlike with the expensive and rigid masks used in optical lithography, EBL patterns can be easily modified, and they often are.

The lithographer we use is a JEOL 840 Scanning Electron Microscope (SEM). The writing capabilities of the JEOL will be highlighted here; for a more detailed description of the imaging capabilities of SEMs, see Section 4.1.3.1. Unlike the UV sensitive polymers mentioned in the previous section, the resists in EBL react to electrons. These electrons are generated with a tungsten hot-cathode filament and accelerated through 35 kV, resulting in a beam resolution of about 8 nm. To write our patterns, an external program called Nanometer Pattern Generation System (NPGS, colloquially known as "Nabity") controls the raster of the beam and directs it according to the user-defined pattern. Given a desired dose and beam current, NPGS determines the dwell time of the beam on each point, typically on the order of microseconds. Typical doses are about 2-4 nC/cm for lines and 200-800 μC/cm^2 for areas.

It should be noted here that dosing is a crucial step and needs to be thoroughly tested in advance. The affected area isn't exactly the same size as the beam, as backscattering off the substrate creates a slight teardrop shape in the resist. The amount of spread is a function of the beam current, but should always be considered when adjusting patterns. Because there is a bit of proximity dosing that occurs, nearby patterns may affect each other and alter the

necessary doses to obtain the desired pattern.

Alignment is generally another concern when writing fine features, so it is worth mentioning here. Patterns are typically written at 1000x magnification, but the dose obtained by the raster required to image the sample at this magnification is intense enough to expose the resist. Therefore, alignment marks are generally deposited along with previous features. Two sets of these are written around the area of interest, one set within the field of view at 200x and one set within the field of view at 1000x. Imaging at 200x is typically not intense enough to expose resist, so positioning these alignment marks on the screen will not affect dose times. (I say typically because, if left long enough, even low intensity can give enough dose to change necessary doses, but allowable times at this magnification are long enough that no issue should arise.)

With the sample positioned at 200x, the user blanks the beam (deflects it away from the sample) and gives control of the beam to Nabity. After aligning at 200x and with the beam still blanked, the magnification can be turned up to 1000x to more precisely align the sample while keeping the beam from sensitive areas. This also ensures alignment is done at the same magnification at which the pattern is being written. With alignment complete, the user defined pattern can now be written onto the sample. Like in the previous section, after the writing is done, substrates can be placed into developer to remove all but the desired pattern.

4.1.2 Deposition and Milling

If lithography was done correctly, one should have a substrate that has a desired pattern for material deposition defined by the remaining resist. We typically use two types of additive deposition, thermal evaporation (Section 4.1.2.1) and sputtering (Section 4.1.2.2), and one

type of subtractive patterning, ion milling (Section 4.1.2.3). The milling removes unwanted material and defines important features, and can be thought of as negative deposition.

Independent of the deposition technique, the samples go through a liftoff process to dissolve the remaining resist and, with it, remove the unwanted sputtered material. The resist used will determine which chemical and process is appropriate for development. Specific details can be found in Section 4.2 and the corresponding subsections.

To continue the artist and stencil analogy from Section 4.1.1, the deposition step would be applying the paint on the stencil, and liftoff would be removing the stencil to leave behind just the painted work.

4.1.2.1 Thermal Evaporation

If heated to sufficiently high temperature, metals will melt and radiate atoms. These will propel spherically away from the source, and eventually deposit on whatever material they hit. This is the fundamental principle of thermal evaporation, and the more energy applied to the metal, the more material will evaporate from it.

Like most thermal evaporators, our Edwards Auto306 Turbo applies heat by pushing a current (usually about a few amps) through highly resistive boats, typically tungsten or molybdenum. With the desired material for deposition sitting in and making thermal contact with these boats, the current in the resistive boats will generate enough heat to melt and evaporate the metal.

As mentioned, the material will radiate spherically away from the boat. However, with sufficient distance from the boat, momenta of the material becomes mostly parallel, and deposition can be assumed to be collimated. To achieve this, the substrate is mounted tens of centimeters away from the boats such that the material is incident on the substrate surface

(90 degrees between the plane of the substrate and the momenta of the material). This angle, with the natural collimation of the deposition, yields very sharp edges of the material on the substrate. However, at times a taper (useful if depositing a second layer in the future) or angle evaporation (useful to deposit particular overlap regions) are desired. To achieve this, the sample surface can be tilted up to about 60 degrees as well as rotated about it's planar axis.

It has been mentioned that the evaporated material is collimated over several tens of centimeters, but this assumes the mean free path is large enough. At low enough pressures, or more importantly in the 10^{-5} torr regime at which the evaporator is operated, the mean free path of the evaporated molecules is on the order of several meters. These pressures are achieved by a combination of mechanical and turbo pump; the former used as a roughing pump, bringing the pressure down from atmospheric pressure while the latter brings it low enough to start evaporation. This transition is seamless because the Auto306 switches from roughing to turbo automatically.

Pumping down to low enough pressures can take several hours, but if one desires speeding the process up, the evaporator has a Meissner trap, or cold-trap, used to freeze out water in the system. When brought to liquid nitrogen temperatures, water molecules that make contact to the trap will stick to the trap, effectively removing them from the environment. Using this trap can save hours for the user, effectively dropping the pumping time by a factor of 2. However, because the water is just frozen out and not removed from the system completely, the cold-trap needs to remain cold for the duration of the evaporation.

To determine the thickness on the sample, a film thickness monitor (FTM) is mounted in the chamber. A film thickness monitor is a crystal oscillator that responds to mass loading. That is, as more material is deposited on the crystal, its thickness increases. Being

a sensitive piezoelectric, this causes the frequency of oscillations in the crystal to decrease. By measuring this change, and with a known surface area and material density, the thickness deposited on the monitor can be determined. The FTM is offset from the vertical to avoid shadowing the substrate holder, but because the evaporation profile is nearly spherical, this position does not affect the thickness reading much. However, because material density is distance dependent ($\rho\, \alpha\, \frac{1}{R^2}$), there are still calibration concerns. To ensure calibration is accurate, a film can be grown in the system and measured in a profile microscope, such as an atomic force microscope (see Section 4.1.3.2). When comparing this result to the FTM, the calibration ratio can be confirmed.

4.1.2.2 Sputtering

While there are many advantages to thermal evaporation, for this work that technique is primarily used to deposit SiOx in the ion mill chamber, as well as to test doses and patterns in the thermal evaporator. Ferromagnets are strictly forbidden in the evaporator lest it become contaminated. Therefore, we need another deposition technique, for which we turn to sputtering. Where evaporation utilizes heat to thermally vaporize metal, sputtering relies on atoms from a metal target being released via collisions with ions in a plasma.

Argon gas is bled into the system near the guns, the areas where material is sputtered from. Each gun can have its own target, the material desired for deposition. The argon molecules that are pumped in interact with electric and magnetic fields intersecting above the target, creating a plasma of positively charged Argon ions (Ar^+) and electrons. The Ar^+ ions are then attracted to the target by applying a negative bias voltage to the target. The ensuing collision is energetic enough to knock atoms of the target free, which spread away from the gun towards the substrate above.

In the sputtering system, there are two types of guns: DC triode magnetron and DC magnetron. Both function as described above, but use different sources of electric and magnetic fields. They are also different sizes, with 2.5" targets for the triode gun and 1" targets for the other. The main difference between these is the beam profile, thus defining the acceptable tolerance of sample position above the gun. For the smallest guns, the profile is sharp enough that samples need to be positioned above the gun within a quarter inch of center. It is therefore important to calibrate the position of all sample and gun combinations for the 16-sample, 8-gun system (4 DC triode magnetron guns, 3 DC magnetron guns, and 1 ion mill), a process that was completed by myself as well as Victor Aguilar (when a new sputtering program user interface was created). Our sputtering chamber is shown in Figure 4.1.

The sputtering process is not a collimated one. Because collisions require a flow of gas, the pressure is much higher than in an evaporation system; typically low 10^{-3} torr. Therefore the mean free path of the sputtered material is not longer than the $\sim$10 cm between target and sample. Due to the amount of undercut in the resist profile, this is not a large concern for the samples discussed here. However, this was a major issue with the work discussed in the appendix and will be discussed further there.

Because deposited material is generated in collisions with the ionized Ar atoms, the rate will be dependent on the frequency and energy of these events. The three main ways to increase this rate are: increase Ar gas flow, resulting in more ionized Ar above the target; increase target voltage, attracting more ions; increase ionization current, increasing probability of ionizing Argon atoms. Of these, only the last is completely favorable. By increasing the flow of argon, the amount of collisions between gas and sputtered material lowers the mean free path, thus lowering the amount of material that reaches the sample. Increasing

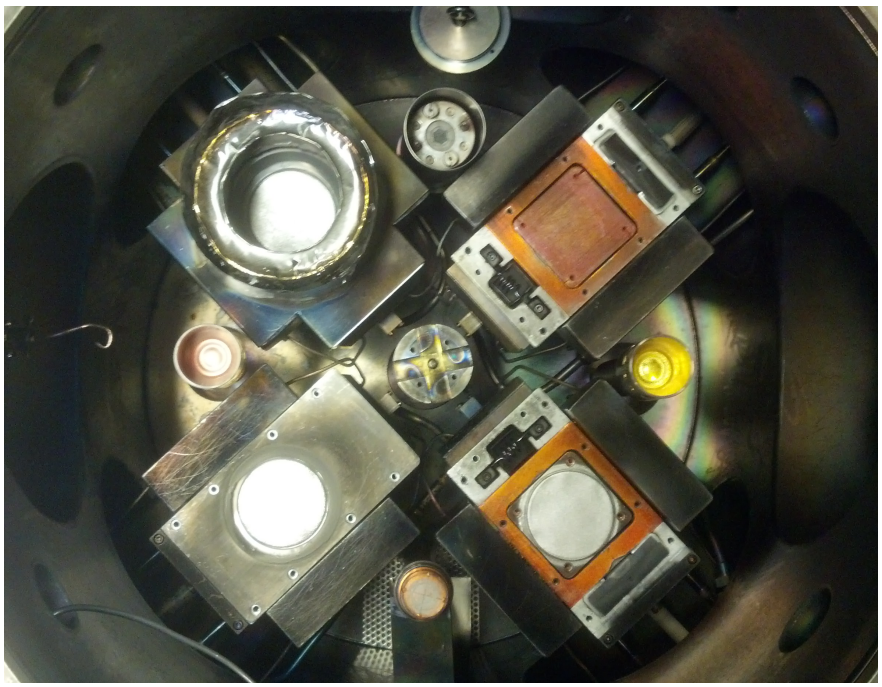

Figure 4.1 *Photo of sputtering chamber.* The triode guns, located in the northeast, southeast, southwest, and northwest corners, are shown at different stages of target installation. Starting at the NE and rotating clockwise: unloaded gun; target loaded in the gun; aluminum housing loaded over the target; fully loaded gun with a chimney over the aluminum housing. The magnetron guns are located at the east, west, and south. The southern gun is unloaded, while the east and west are loaded with Au and Cu, respectively. The ion mill is shown at the north, with its cap just north of it. To the far west, the tool used to open and close the shutters, the wobble stick, is shown.

the target voltage could increase the amount of ions attracted, it could also increase the energy of collisions. The more energetic sputtered atoms could alter the consistency of the deposition, resulting in a less ideal final device. Increasing the current, though, increases the likelihood of ionizing Ar. This increased amount of Ar^+ increases the frequency of collisions without saturating the environment or adjusting the energy.

The deposition rate for each gun is determined by an FTM and is checked immediately before the sputtering program is run for each chip. This works much like described above in Section 4.1.2.1. The main difference is that the rate is not being constantly measured during deposition, but checking after each chip typically shows consistent rates throughout the run.

Since the chamber holds up to 16 samples, but only one is fabricated at a time, there is a need to protect the other chips. To prevent material from being errantly sputtered, there are two shutters: one for the chamber, which is situated between the targets and the samples; another for each sample holder, which are manually opened and closed by the user. This happens immediately before and after each run so that only the desired sample is exposed to deposition. Once the sample-holder shutter is opened, a clever combination of the chamber shutter plate and sample position is required so that the sample never passes over exposed guns, changing the structure and material deposited.

Because run-to-run contamination was a concern when discussing evaporation, it would be incomplete to not mention something about it here. To prevent material from past sputtering runs contaminating the deposition, all exposed common surfaces have the excess previously deposited material removed. For the sample holders, that involves soaking parts in a Nitric Acid bath for 30-40 minutes, adding hydrofluoric acid (HF) to the sample shutter parts if necessary. Chimneys around the guns and the chamber shutter plate are wrapped in aluminum foil before sputtering. Therefore, after sputtering, the foil is removed and chimneys

re-wrapped with a clean layer. The gun parts themselves are dedicated to a specific material, so no contamination arises from these.

4.1.2.3 Ion Milling

The deposition techniques mentioned above can be thought of as additive, as material is being grown on the substrate. Ion milling is a subtractive process, as material is milled away from the sample. Although it is not exactly a deposition technique, I have included it here as it is vital to sample fabrication; the pattern and geometry of the Josephson junction pillars are defined through ion milling.

As in the sputtering system, ion milling uses ionized argon gas and accelerates it towards a target, scattering material from that target in the ensuing collision. However, the distinction arises when considering what the ions are colliding with. In a sputtering system, the target is the material to be deposited on the sample, collisions being the mechanism to knock them loose and send them towards the sample. In the ion mill it is the sample itself with which the ions collide, material to be removed from it.

There are two ion mills that are used frequently in sample fabrication: one in the sputtering chamber and one in a dedicated milling chamber. The one in the sputtering chamber is primarily used as an *in situ* cleaning technique before sputtering and the one in the independent chamber is used to mill and pattern samples. While they are functionally the same, specific details in this section will focus on the independent chamber mill unless otherwise noted.

Argon gas is fed into the discharge chamber, a section of the mill that houses a cathode and anode. Applying a voltage difference between the two, typically between 150 and 300 V, and a current to the cathode generates an electron beam that will ionize argon gas. Once

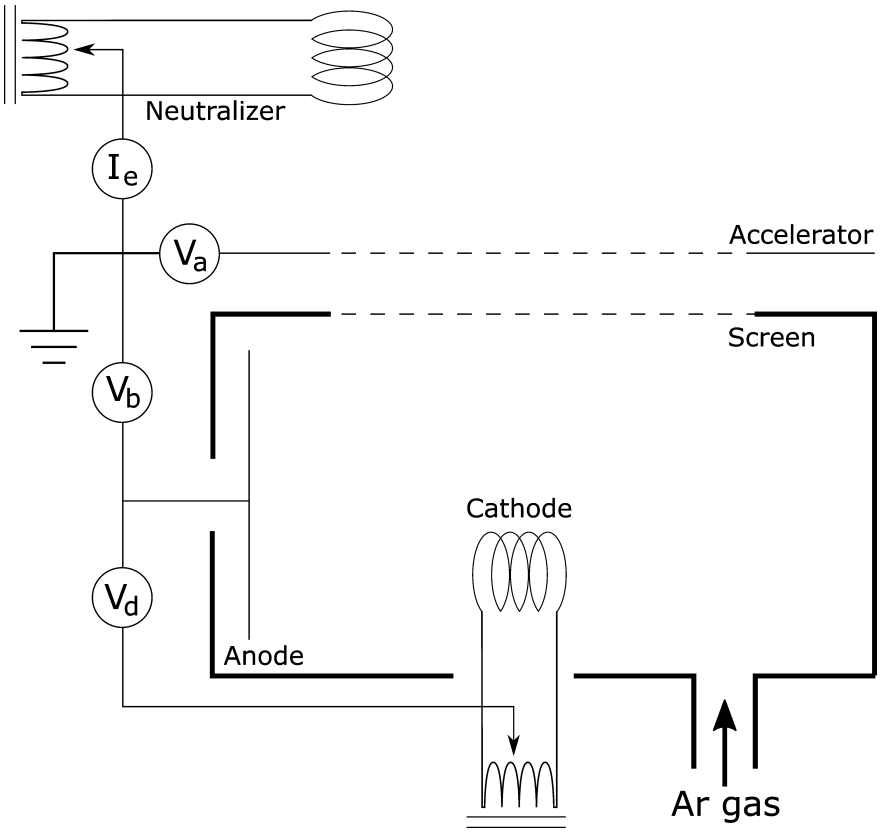

Figure 4.2 *Schematic of ion mill chamber.* The thick solid line represents the ion mill housing while the dashed line represents the grid the ions pass through to reach the sample. User controllable parameters labeled in the diagram: V_a – Accelerating Voltage; V_b – Beam Voltage; V_d – Discharge Voltage; I_e – Neutralizer current [80].

ionized, Ar^+ atoms are accelerated by a potential difference applied to the accelerating grid, typically between 50-100 V. This grid is perforated to adjust the beam profile and somewhat collimate it. To maintain collimation of the like-charged argon atoms in the beam, a neutralizer is located just above the grid that adds electrons to the beam.

To determine the milling rate, an FTM and a gold sputtering gun are located in the milling chamber as well. After getting gold deposited on it, the FTM is moved over the mill and the rate can be determined as a negative deposition. By knowing the desired mill depth and rate, total mill time is calculated by the user.

A major concern is that milling rates are material dependent. While we can measure the

milling rate for gold, every material that needs to be milled through will have a different rate. To account for this, rates for each material are measured in advance by measuring milled depth in an atomic force microscope, as discussed in Section 4.1.3.2. Using this ratio, the thickness of each layer can be converted to an effective thickness, relative to gold, and timed appropriately.

Also located in the mill chamber is a silicon monoxide (SiOx) thermal evaporator. The evaporator functions as described in Section 4.1.2.1. It is used to deposit SiOx on the sample after milling and isolates future top leads from the bottom leads everywhere except through the patterned pillars. This is described further in Section 4.2.3.

4.1.3 Microscopy

To optimize the fabrication process, it is important to be able to see the fine details and differences that change as we adjust various lithography or deposition parameters. This section will talk about two main ones we use during fabrication analysis and optimization: Scanning Electron Microscopy (Section 4.1.3.1) and Atomic Force Microscopy (Section 4.1.3.2).

4.1.3.1 Scanning Electron Microscopy

The pillar junctions discussed in this work have diameters of 1 μm or less, so to characterize and optimize the fabrication process, an imaging resolution far below that (and that of optical microscopes) is needed. To image our samples, we utilize a Hitachi S-4700II Scanning Electron Microscope (SEM) with an upper magnification limit of 500,000x. While there are many imaging techniques possible with most SEMs, our Hitachi displays signals from secondary electrons and will be the main technique described here.

As with the JEOL mentioned previously (Section 4.1.1.2), primary electrons are generated

from an electron source. Unlike the JEOL, which uses a hot-cathode filament, the Hitachi uses the sharp tip of a field emission gun, a cold-cathode filament. If exposed to an electric field, an electron cloud will form around this tip. These electrons are then funneled away through the Wehlnet cap, a negatively charged enclosure with an opening pointing towards the imaging chamber. These are further accelerated toward the anode, a positively charged plate with a hole in it, through which (some of) the electrons pass. While accelerating voltages of 30 kV are possible, our machine is typically run at 15 kV, allowing for resolutions as fine as 1.5 nm. On their way to the sample, this beam of electrons will pass by a number of condenser lenses, magnetic lenses which confine and focus the beam.

Just before the beam gets to the sample, it passes through deflection coils and an objective lens. The former is used to position the beam on the sample while the latter focuses it one final time, creating a very fine and resolved electron beam directly onto the sample. There are also eight electromagnetic coils that determine the stigmation, a measure of circular distortion of the beam. After passing through one final aperture, which removes any unfocused electrons, this focused and sharpened beam hits and scatters on sample surface.

There is enough energy from this impingement to scatter low-energy electrons (3-5 eV) from the material in the sample. Initially scattered in all directions, they are attracted to a charged Faraday cage, part of an Everhart-Thornley detector. Once inside the cage, these electrons get accelerated into a scintillator, the light of which is amplified in a photomultiplier. Due to the focus of the beam, the signal from the photomultiplier gives an effective brightness for just one point on the sample, effectively one pixel of the image. The beam is therefore rastered across the sample, with signals being processed for each position of the beam (and corresponding pixel on the screen for the user).

An advantage to this imaging technique, which gives rise to the ability to further char-

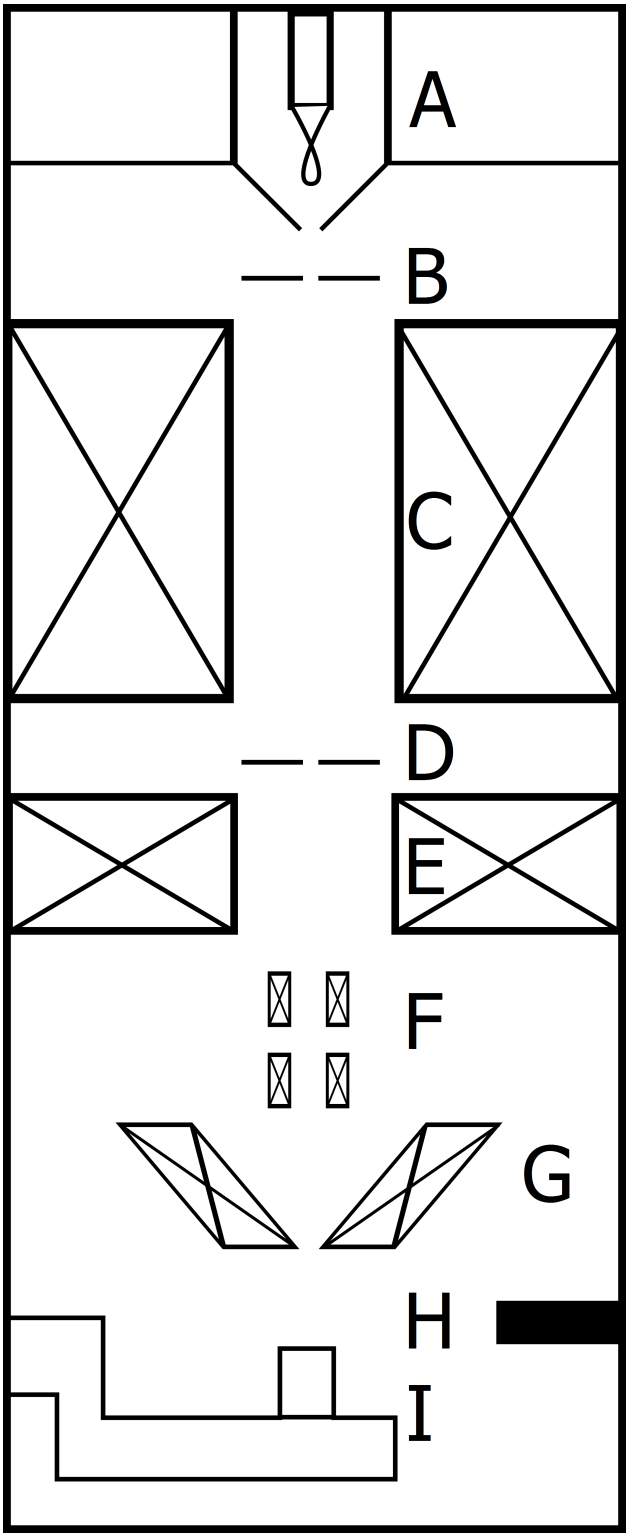

Figure 4.3 *Schematic of Hitachi SEM.* A) Electron gun; B) Beam monitor aperture; C) First condenser lens; D) Objective aperture; E) Second condenser lens; F) Deflection coils; G) Objective lens; H) Detector; I) Sample stage. Stigmation coils (not pictured) are located left of (H).

acterize the sample, comes from the result of this scattering. The secondary electrons that scatter from the sample leave vacancies at lower energy states. Higher energy electrons can transition to these vacancies, emitting an x-ray, called a characteristic x-ray, in the process. The energies of x-rays emitted this way are unique to the element which emitted it, so measuring this energy can give information on the material present and the concentration thereof. Fortunately the Hitachi system used in our cleanroom is equipped with an energy-dispersive x-ray spectroscopy system (EDS or EDX) to do just that, which is very useful to determine and confirm alloy concentrations in our samples.

The S-4700II has a number of other features, but the last one I will discuss here is that of its tilt and rotation controls. Our system can tilt a sample up to 50 degrees with holders that can load samples in-plane or edge-on to the beam. This, with the ability to rotate the sample holder, allows for imaging at any angle. While most imaging is done without any tilting, it becomes a very useful tool when investigating undercut profiles or tapering on edges. Like the EDS system, this proves more helpful in the early efforts of development than when making samples to measure, but without it our sample fabrication process would be far less regulated.

4.1.3.2 Atomic Force Microscopy

Atomic Force Microscopy (AFM) is a technique to primarily measure the surface morphology of a sample. Naively, atomic force microscopy (AFM) can be best described as the act of dragging a fine point over a surface and measuring the vertical deflection of the tip. This description might be appropriate if it were able to convey the sensitivity of this technique: errors of measurement are on the order of half an angstrom.

For AFMs like ours, a Dimension 3100 Scanning Probe Microscope (SPM), this “fine

point" is a sharp tip (about 4 μm diameter for us, but in some systems it can be atomically sharp) on the end of a cantilever arm (about 100-200 μm long). This lever arm has a force constant (in N/m) which determines the amount of surface forces needed to deflect it. Of these surface forces, the interactions with the greatest effect are electrostatic, dipole-dipole, and van der Waals forces. A laser that shines on the back of the cantilever is reflected into a detection system of photodiodes, and minor changes in intensities can be interpreted as tip deflection. Through this mechanism, very fine resolution, like the aforementioned half-Angstrom, can be obtained.

While the description above is a rough idea of how contact mode works, a more sophisticated measuring technique, tapping mode, was used in the development of this work. In this mode, instead of keeping the tip static and dragging it over the surface, it is vibrated near its resonant frequency (usually around 300kHz). Interacting with the surface at every approach, the oscillations can become dampened. The height of the tip is therefore adjusted to maintain optimum oscillation amplitude. As this scans the surface of a sample, these height adjustments are the direct measure of the surface profile.

While AFM systems are a very effective way of measuring a surface profile, they can also be used to determine other sample characteristics. The one that played the biggest role in this work is that of magnetic force microscopy (MFM). When using this characterization technique, special tips that are coated in a magnetic material are used. These MFM tips have the same properties as AFM tips when it comes to the surface profile, while the force constant will again determine how much or how little force is needed to deflect the tip. However, unlike standard AFM tips, the magnetic material coating on the tip gives rise to another source of deflection: magnetic forces. While the coating can be soft or hard (depending on user needs), attractions (repulsions) between the magnetic material in the sample and the tip will

register as "low" ("high") height adjustments. When running in MFM mode, a surface scan is carried out just like in AFM mode, followed by a secondary scan probing these magnetic interactions. The tip is lifted slightly above the surface, following the previously measured profile, measuring only the magnetic deflections on the second pass. When comparing this to the standard surface scan, the system can determine location of poles in the magnetic material, which has been useful for this work when studying domain structures or determining size needs for single domain pillars.

4.2 Procedure

At the risk of trivializing the efforts needed to create functioning samples, a simplified process is below:

1. Protect and dice wafer
2. Define base layer with photolithography
3. Sputter base multilayer and lift off resist
4. Pattern submicron pillars with electron beam lithography
5. Ion mill, evaporate silicon monoxide, and lift off resist
6. Define top leads with photolithography
7. Sputter top layers and lift off resist

The entire process is shown in Figure 4.4. Whenever possible, samples were protected from contaminants, such as dust particles, by processing them inside a cleanroom environment. Whenever necessary to bring these samples out of the cleanroom, such as sputtering or

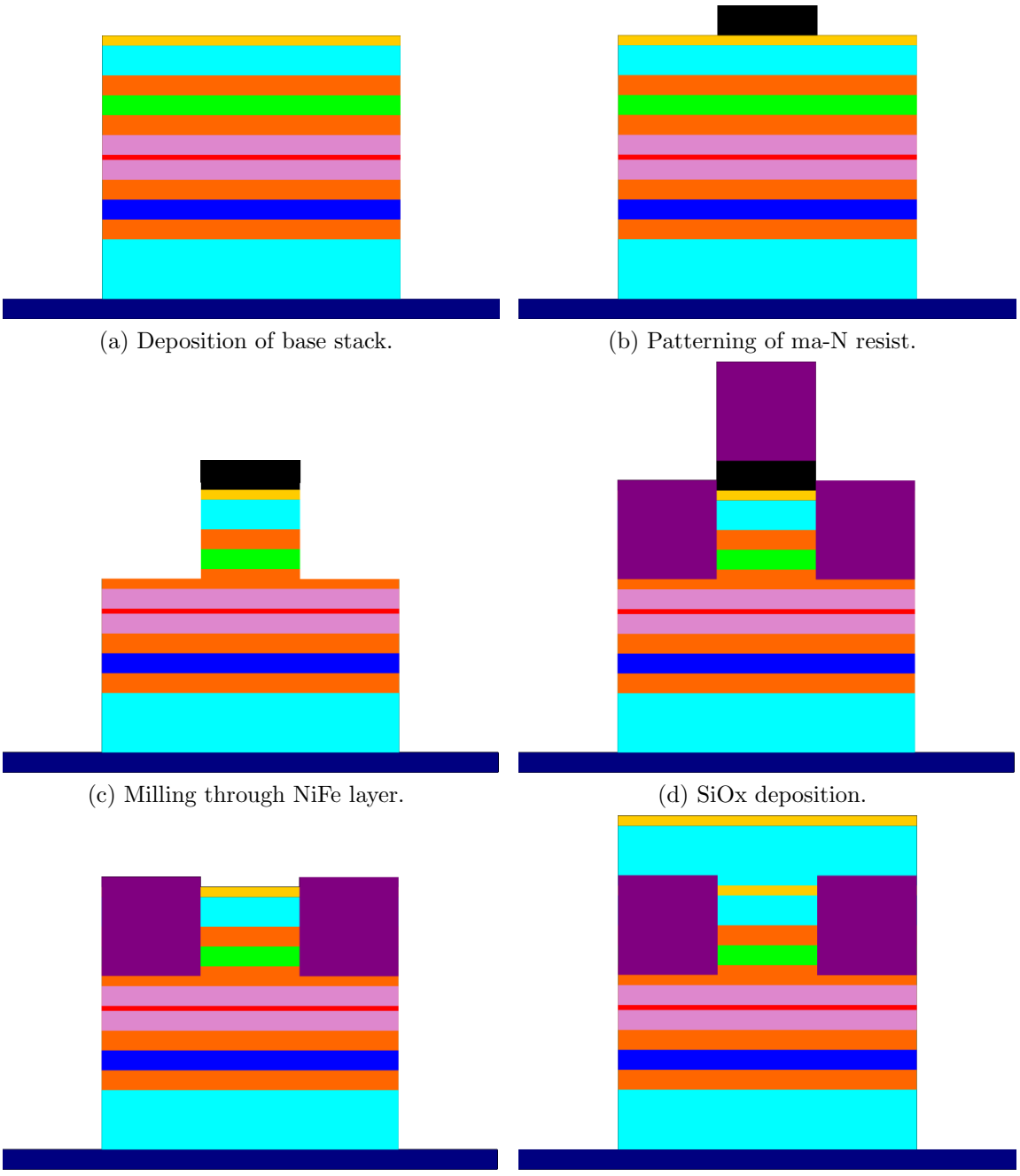

(a) Deposition of base stack.

(b) Patterning of ma-N resist.

(c) Milling through NiFe layer.

(d) SiOx deposition.

(e) ma-N liftoff.

(f) Top lead deposition.

Figure 4.4 *Cartoons of sample fabrication steps.* Layer thicknesses are drawn for clarity and are not to scale. Colors from bottom up: Dark blue – Si substrate; Light blue – Nb; Orange – Cu; Blue – F' (typically Ni); Light purple – Co; Red – Ru; Green – F" (typically NiFe); Yellow – Au; Black – ma-N resist; Purple – SiOx.

ion milling, the samples were kept free from contaminants with multiple protective barriers, such as sealing them in nitrogen filled bags and isolating them with shutters.

4.2.1 Wafer to Chip

We fabricate samples on <100> p-type Boron-doped Silicon chips with resistivity 1-10 Ω-cm. These 3" wafers must be diced into 1/2" x 1/2" substrates on the dicing saw. To protect the chips from silica dust and other contaminants, a protective layer of S1813, a typical photoresist, is spun coat onto the wafer before dicing. Unlike during the lithography steps described in Section 4.1.1, consistency of the S1813 is unimportant so long as resist covers the entire wafer.

After dicing, chips are cleaned thoroughly before use. To do so, we place them in acetone, warmed to 90 °C on a hotplate. The chips are then ultrasonicated for 5 minutes, followed by 5 minutes of ultrasonication in isopropyl alcohol (IPA) to remove acetone residue. These chips are then rinsed in de-ionized (DI) water before being blown dry with dry N_2 gas. After ensuring each chip is clean by looking at it in the optical microscope, the substrates are ready for processing. If there is any remaining residue, previous cleaning steps are repeated until the chip is clean.

4.2.2 Fabricating Base Layer

Chips are spun coat with S1813 at 5000 rpm for 50 seconds, resulting in a photoresist thickness of 1.3 μm. They are then baked on a 110 °C hotplate for 1 minute to remove solvent. Coated chips can now be exposed through the base lead mask. Visualized in Figure 4.5, this mask patterns three necessary features of the base lead: the base wire that will make up our Josephson Junction pillars, as discussed in this section; alignment marks for the electron-beam lithography step, as discussed in Section 4.2.3; and alignment marks used during the photolithography of the top leads, as discussed in Section 4.2.4. After ensuring

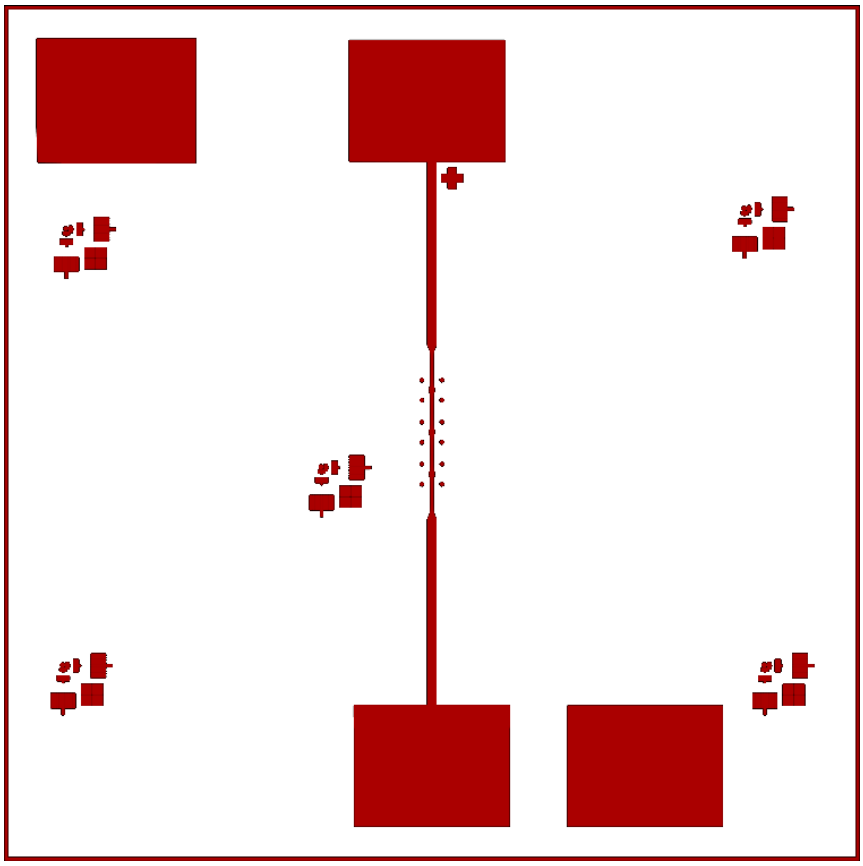

Figure 4.5 *Schematic of base lead mask.* Aside from patterning the base lead wire, optical alignment marks (Vernier alignment marks spread around the chip) and EBL alignment marks (small crosses near the wire) are also deposited for upcoming fabrication steps.

proper centering via optical microscope, each chip is exposed to UV light for 11 seconds.

To develop, the chips are first dipped in chlorobenzene for 5 minutes, agitating for the first 10 and final 30 seconds of the dip. This process hardens the surface of the S1813, making it less susceptible to development and giving the photoresist profile its undercut. They are then wafted in MF 352 solution for 45 seconds to develop, stopping development by wafting in DI water for 30 seconds and blowing dry with N_2 gas. All samples are then inspected under an optical microscope to ensure development has been completed. If residual resist remains in the pattern, the sample is returned to the MF 352 for a few seconds longer, and repeated until the pattern development is thoroughly finished.

Now ready for deposition, these chips are loaded into sample holders for the sputtering chamber. The full Josephson junction stack, Nb(100)/Cu(5)/Ni(1.2)/Cu(10)/Co(4)/ Ru(0.75)/Co(4)/Cu(10)/NiFe(1)/Cu(5)/Nb(20)/Au(15) (from bottom to top), is sputtered in this step. Depositing the entire multi-layer in this way never breaks vacuum, ensuring that the interfaces between layers are as clean as possible. However, the process therefore requires ion milling as a subtractive technique to define the pillars. This will be discussed in the next section. The top 20 nm Nb is enough to superconduct, and is coated in 15 nm Au to prevent oxidation and exposure when removed from the sputtering chamber.

Attached to the sputtering holders is a permanent rare-earth magnet, creating a field in which the multilayer stack is grown. Given that the pillars are circular, there is no favorable direction for the magnetization to point (see Section 2.1.1). Growing it in a field is an attempt to constrain it, at least somewhat. The magnetocrystalline structure may develop an anisotropy favoring the field direction. While this might make the NiFe point more easily in the growth direction, which is also the "on" direction, it simultaneously makes it a bit harder to point in the perpendicular, or "off" direction. Given that the NiFe will develop an anisotropy regardless, just one that would be random, growing in a field is worth the trade-off. At least one of the directions is favored in this way, and as they say, "better the devil you know than the devil you don't."

To liftoff the photoresist mask, chips are placed into acetone warmed to 90 °C for at least 10 minutes. When it appears that the liftoff process is complete, chips are placed in the ultrasonicator once again to ensure all residual S1813 or sputtered material is removed. They are then rinsed and ultrasonicated with IPA to remove any residual acetone and blown dry with N_2 gas to remove all IPA residue.

4.2.3 Defining and Milling Josephson Junction Pillars

At this point, the vertical Josephson junction runs along the entire length of wire, so we must mask only our desired pillars and ion mill everything else. Because the dimensions of the 0.3-1.0 μm diameter circular pillars are too small for optical lithography, we rely on electron beam lithography (EBL) to pattern the ion mill mask. To do so, we spin a single layer of negative e-beam resist, ma-N 2401, at 3000 rpm for 40 seconds, baking it for 120 seconds on a 90 °C hotplate.

These chips are then placed in the JEOL 840 SEM for patterning. Alignment becomes crucial in these steps, so marks deposited during the previous sputtering run are used to ensure the pillars are located accurately. Tests that were run previously show that a dose of 500 μC/cm^2 is sufficient exposure for the ma-N. Patterned near the pillars are two useful features: a pinwheel and a large, 3 μm diameter disk. The pinwheel helps determine the quality of the SEM stigmation while the disk helps during liftoff, as discussed later in this section. After EBL, chips are developed in AZ 300 MIF for 30 seconds and rinsed in DI water for 20 seconds to stop development. The exposed ma-N should still remain, as shown in Figure 4.6.

These samples are then loaded into ion mill holders with a 5 mm x 5 mm mask, exposing the center for milling. Overheating the resist makes liftoff almost impossible, so a small drop of diffusion pump oil is placed between the sample and the heat sink to ensure good thermal coupling. At relatively high milling energy, 300 V, samples are milled halfway through the second Cu layer (from the top), which patterns the Py as well. This allows for easier Py switching, as discussed in Section 6.1.2. While each chip takes about 5 minutes of milling, mainly due to the slow rate of milling Nb, each chip is milled for no longer than 2 minutes

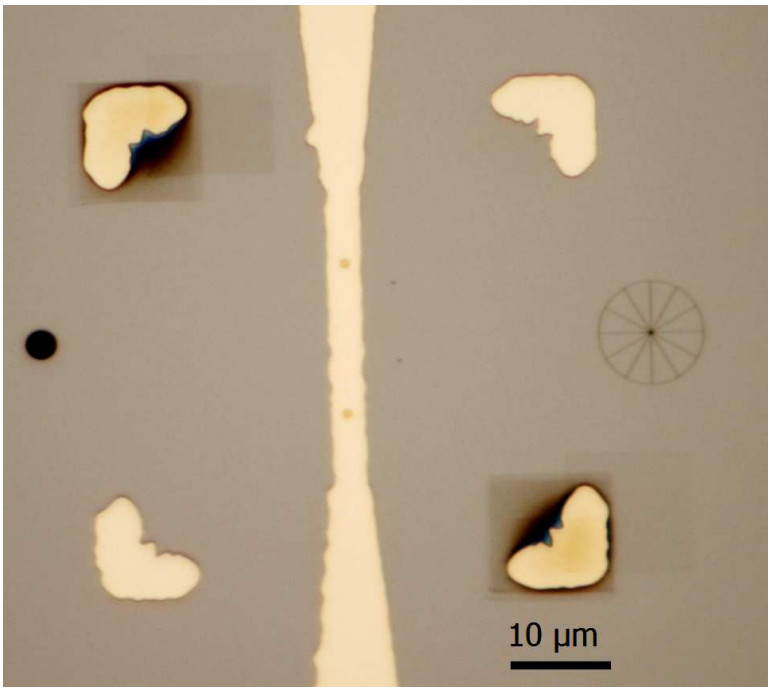

Figure 4.6 *Image of ma-N pillars.* The dots on the vertical gold wire are pillars made of ma-N resist. The resist will prevent the wire underneath from being milled, defining the circular junctions.

at a time, once again to prevent the resist from overheating.

After milling is completed, 50 nm of Silicon Monoxide (SiOx) is deposited to isolate the bottom wire from the future top leads. Assuming no pinholes exist in the SiOx, this forces any current through the pillar and defines the geometry of the junction. Because the pillars are so small, some SiOx may creep along the sides of the resist, prohibiting clean liftoff. To try to reduce the likelihood of liftoff issues, the samples are loaded into side-mill holders. These rotate the sample so that there is a 3-degree angle between the mill and the surface of the substrate. Each sample is milled at this glancing angle for 2 minutes, flipped 180 degrees so that both sides of the pillar are exposed, and milled for another 2 minutes.

To liftoff the ma-N, the chips are then placed in a beaker of PG remover warmed on a 110 °C hotplate. After about 10 minutes in the warm remover, the chip is rubbed vigorously with a cotton swab to break apart any remaining SiOx covering the pillar resist. The beaker

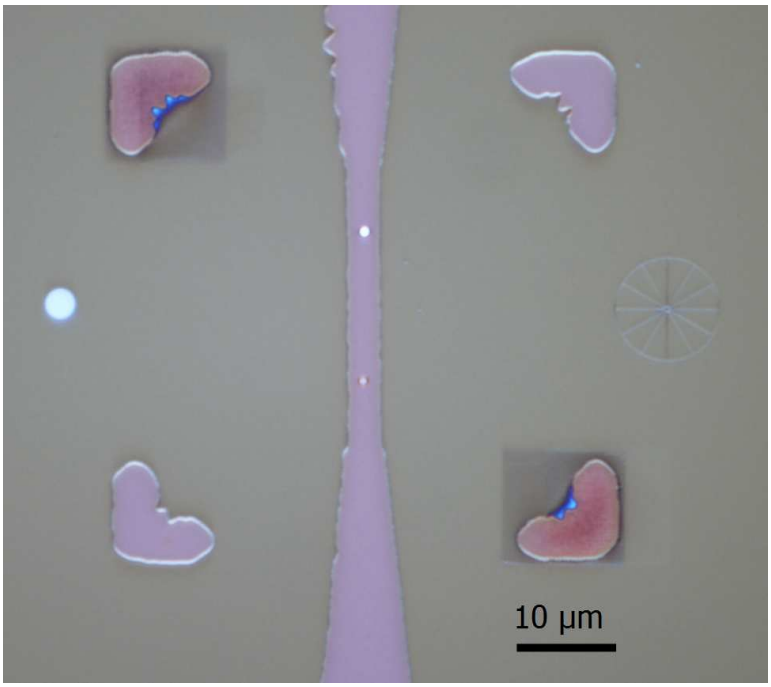

(a) Unsuccessful liftoff of ma-N.

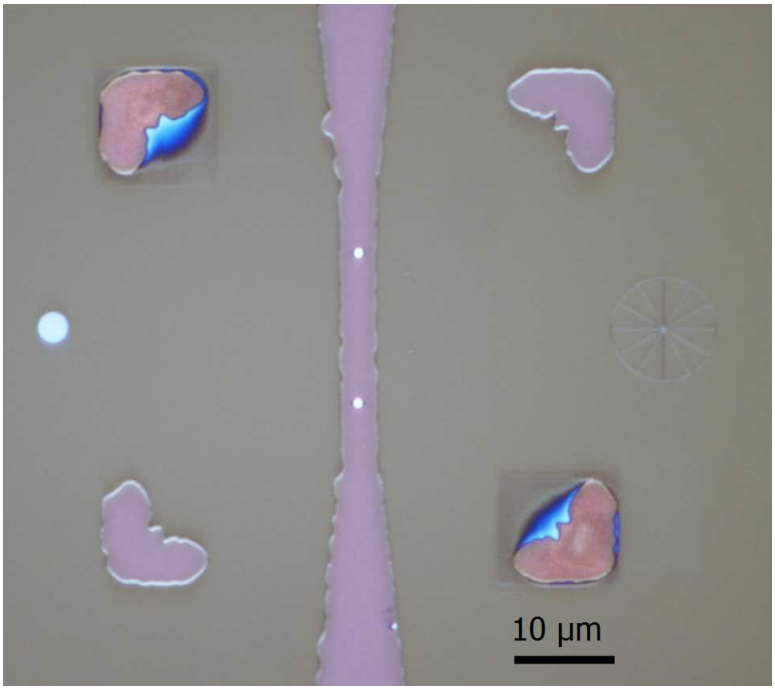

(b) Successful liftoff of ma-N.

Figure 4.7 *Images of ma-N liftoff.* In both images, the top pillar has successfully lifted off. However, in (a), the bottom pillar is still covered in resist.

is covered in aluminum foil to raise the temperature of the PG remover slightly higher and let sit for another 5 minutes before putting it in the ultrasonicator for a final 5 minutes. Chips are then rinsed in DI water, blown dry with N_2 gas, and inspected under the microscope. Because the pillars are often too small to see clearly, the larger pillar patterned on the side will show whether the sample needs more time in the liftoff or not. If so, the process is repeated, and sometimes left in PG remover overnight. At this point, any further attempts have been shown to be fruitless, and any clogged pillars are sacrificed. What a successful liftoff looks like under the microscope is shown in Figure 4.7b.

4.2.4 Fabricating Top Leads

The samples are now ready for top lead deposition, so they are once again spun and baked with a S1813 monolayer, described in Section 4.2.2. Exposure and development are the same here as well, but with an added emphasis on alignment. Because alignment for the top leads is once again crucial, a lot of time is spent adjusting the position and rotation of each chip so that the Vernier alignment marks (Figure 4.8) are aligned.

After development, the samples are placed in the plasma etcher to clean the surface of the pillar and clear off remaining resist residue. The etcher is previously cleaned by running it empty at 300 W and 500 mTorr O_2 gas for 5 minutes. After cleaning the system, the chips are exposed to an 100 W, 500 mTorr O_2 plasma etch for 90 seconds before being loaded once again in the sample holders for sputtering.

After pumping down the sputtering chamber, the samples are ion milled at a low energy (175 V) to clean any remaining residue on the surface of the pillar. This is done *in situ* with the sputtering process, which deposits Nb(150)/Au(20) on top of the pillars. Liftoff once again is the same as described in Section 4.2.2. After the liftoff process, the chips are

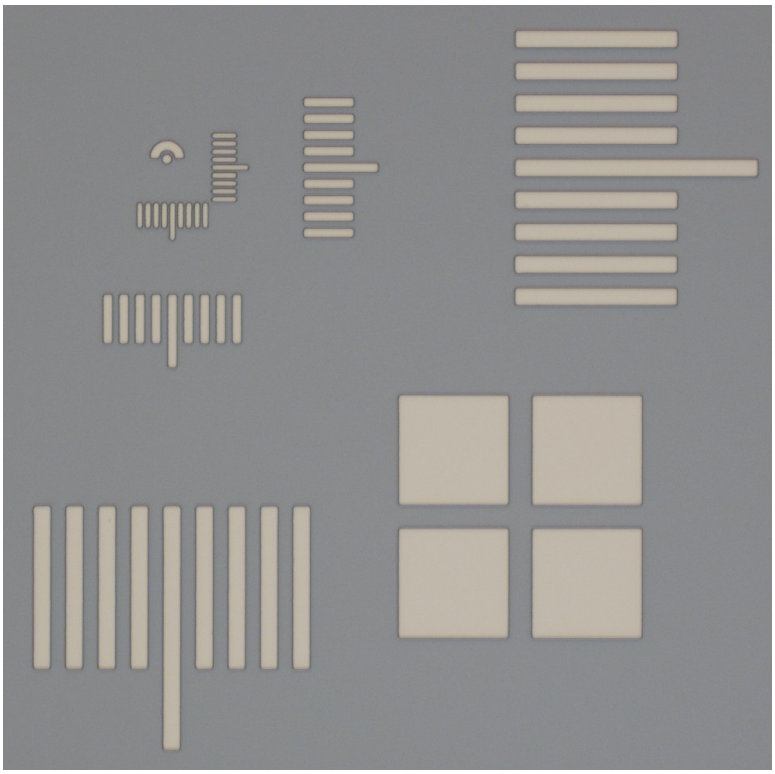

Figure 4.8 *Image of Vernier alignment marks.*

completed and ready to be measured. The entire sample fabrication (to make eight chips, each with six pillars) typically takes between two and three weeks.

Chapter 5

Measurement

When conducting research at low temperatures, the required temperature range for the project will determine what refrigeration technique is required [81]. For temperatures down to 4.2 K, the simplest solution is to dip samples directly into liquid helium-4. By pumping on it, the evaporation of helium-4 can bring temperatures down to about 1 K. If we pump on helium-3, temperatures of about 0.3 K can be achieved. However, below this, use of a dilution fridge is required. By using a mixture of ^{3}He and ^{4}He, experimentalists can measure to temperatures as low as 2 mK.

As the temperature range decreases, the cost, both in terms of money and time, to run the experiments increases dramatically. The work discussed in the appendix required at least a system that could achieve 0.3 K, perhaps even colder. Thankfully, the work discussed in the bulk of this thesis could be done at 4.2 K, and the measurement scheme and equipment used for this experiment will be described in this chapter.

5.1 Quick Dipper II

In order to be measured, the devices in this work must have access to current and voltage leads, for 4-terminal measurements, as well as external magnetic fields in at least two orthogonal directions, to rotate the magnet. Since none of these are present in a liquid helium storage dewar, special probes needed to be developed. In the 1990s, Dr. William Pratt, Jr.

meticulously engineered and created these probes in house, called Quick Dippers, which can be dipped into standard 60-liter liquid helium storage dewars. There are several of these probes we use today that are designed for various purposes; the most basic system has the ability to attach up to 6 current and 6 voltage leads on a substrate, useful to switch between different samples on the same chip, while one of the most complex has a separate He-3 pot and charcoal pump to bring sample temperatures down to 0.4 K and below.

For this work, Quick Dipper II (QD-II) was primarily used as it has had been built with two orthogonal magnetic coils: a longitudinal coil that can supply a field along the dipper (hereto forth referred to as the y- or longitudinal-axis) and a transverse coil that supplies a field across the dipper (x- or transverse-axis).

The longitudinal coil has a coil constant of 22.58 (+/- 0.15) mT/A while the transverse coil's is 8.74 (+/- 0.04) mT/A, allowing for fields greater than 450 and 170 mT, respectively, when attached to the 20 A Kepco Bipolar Operational Power Supply (BOPS). Considering the only time during the experiment that we apply larger than 20 mT to our sample is when magnetizing (done at 260 mT), these fields are much more than sufficient. A superconducting persistence loop allows for current to flow without a constant external supply, potentially decreasing the noise in the system. This switch needs to become heated (driving it normal) to change the field. Because this is a sensitive switch, the measurement programs discussed later control it automatically, preventing users from destroying it accidentally.

Mounting a sample in the system is a bit more complex than most of the other dippers, but is not difficult to become accustomed to. Up to a half-inch sample can be mounted by first placing it on the brass sample plate and tying it down with string. This is done to minimize any movement or shifts of the sample as it cools in the dewar. Current and voltage leads are then pressed onto the superconducting pads with indium solder, as shown

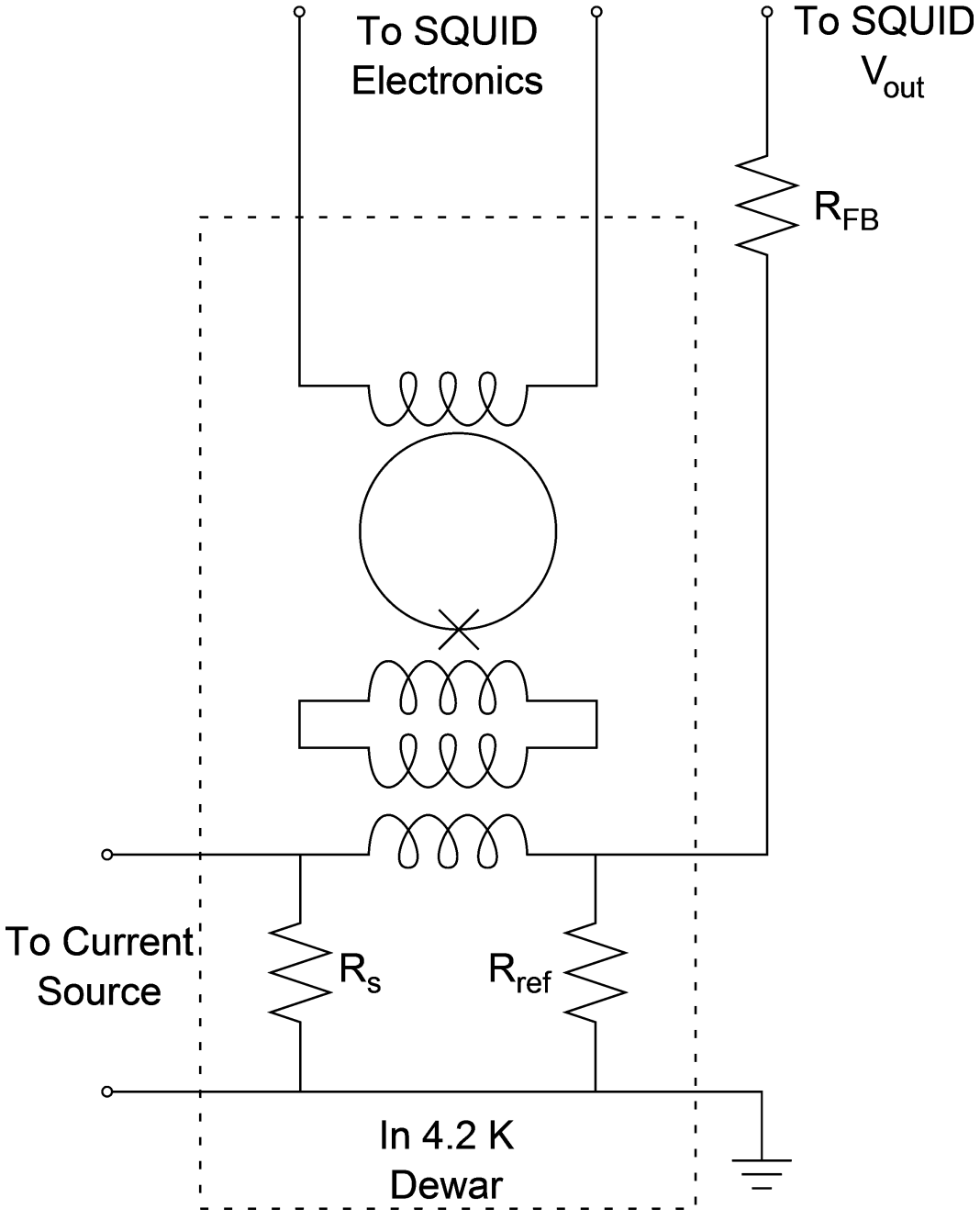

Figure 5.1 *Schematic of Quick Dipper-II.* Electronics for magnetic coils have been omitted.

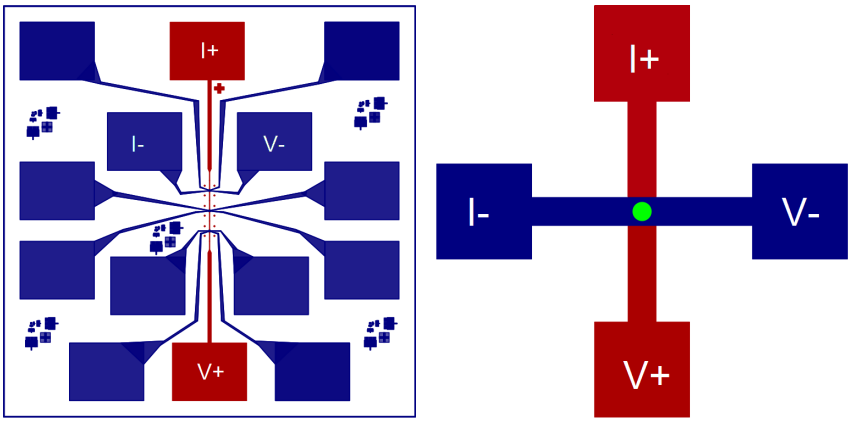

(a) Schematic of chip geometry.

(b) Cartoon representation of lead orientation across pillar.

Figure 5.2 *Top-down representations of lead geometry across sample.* The current is driven from the base lead (red) through the Josephson junction (green) and along the top superconducting lead (blue). Voltage is measured across the pillar.

in Figures 5.2 and 5.3b, with one current and one voltage lead on each side of the pillar (top and bottom leads). Although the top lead geometry allows for it, each wire does not need its own pad because the leads are superconducting. As long as the wires don't share the same solder joint or normal leads, the voltage drop will only be measured across the pillar.

Once the leads are secure, the longitudinal and transverse coils that had been previously pulled back to allow access to the sample plate (Figure 5.3c) can be slid into position over the sample (Figure 5.3d). Guide rods are then unscrewed from the base and replaced with screws that tighten the coils to the sample plate. This is done one at a time to prevent rotation of the coils and tangles in the lead wires. At this point, the longitudinal magnet is set, but the transverse coils are still loose. The two coils are designed to splay out, giving them room to slide up and down the dipper. However, these must be tied together when mounting to ensure that each coil is static when creating a field, maintaining the expected field at the sample.

After the coils are in place, all of the slack in the magnetic leads needs to be protected.

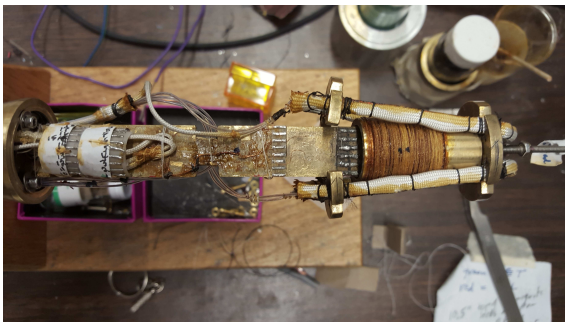

(a) QD-II before mounting.

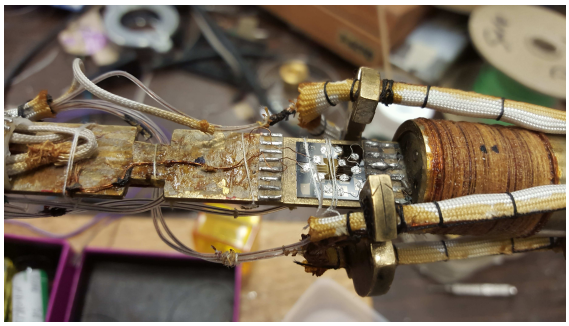

(b) Sample mounted on QD-II

(c) QD-II magnet coils ready to be slid up.

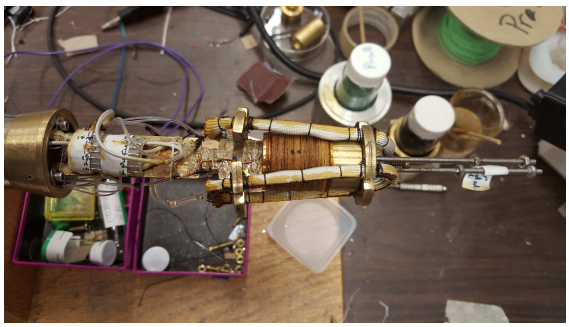

(d) QD-II magnet coils slid to cover the sample.

(e) Closing the clamshell to protect the magnet leads.

(f) Fully closed QD-II.

Figure 5.3 *Mounting QD-II.* The sample is first mounted on the dipper (a to b), then the magnetic coils are slid over the sample (c to d). After the transverse coils are tied together (e), the clamshell is closed around the magnetic leads and tied to secure it (e to f).

A clamshell-like protective enclosure is placed around these leads and covers all electronics still exposed, from the base of the dipper to the top of the coils (Figure 5.3e). This prevents any leads from getting tangled around something if they move in the dewar during dipping/removal of the probe. This clamshell is then tied down with a lot of string, keeping it shut tight. Lastly, the knots are secured with a dab of GE Varnish to make sure they can't come untied, making the shell useless (Figure 5.3f). Once the varnish dries, the sample can then be dipped into the dewar.

Along the path of the voltage leads, there are a number of other elements that are characteristic to each dipper. They include reference and feedback resistors (R_{ref} and R_{FB}) and a superconducting quantum interference device (SQUID) current comparator circuit. These can be seen in Figure 5.1 and will be discussed in the following sections.

5.2 SQUID Electronics

5.2.1 Overview of SQUIDs

Superconducting quantum interference devices (SQUIDs) are circuit elements consisting of superconducting loops with a small Josephson junction on each limb, as shown in Figure 5.4. These systems are very sensitive to magnetic flux and therefore very useful tools for data collection. They are in no way the focus of this work, but the data collected herein are taken with a SQUID comparator circuit, and therefore a brief description of SQUID physics is useful.

A single Josephson junction has a periodicity in its critical current based on flux through the junction, as discussed in 2.4.2. By putting two junctions in parallel, we maintain this

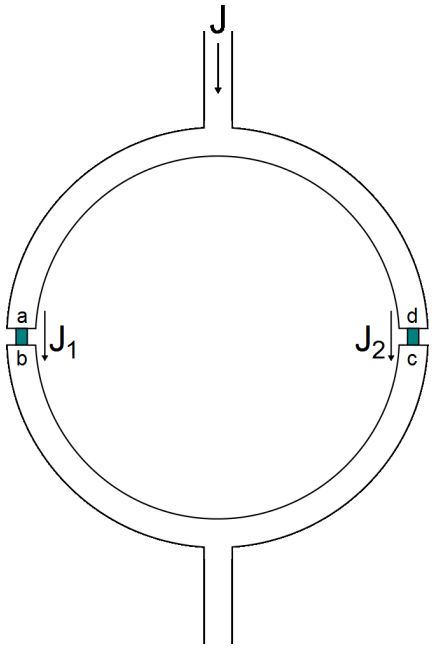

Figure 5.4 *SQUID Loop.* The current that enters the loop splits between both Josephson junction (blue) branches. The flux in the loop determines the interference between the junctions and thus the size of the critical current through the loop.

periodicity, but obtain a second as well [82]. This additional oscillation is due to the flux passing through the superconducting loop (Fig. 5.4). Looking at a path around the loop, $a \to b \to c \to d \to a$, we find expressions that are analogous to a Josephson junction in a magnetic field [83] (see Section 2.4). If the superconducting film is thicker than the London penetration depth, the integral of current density along the entire loop will vanish, and we are left with only the phase gradient term of Eqn 2.19.

Integrating over the entire loop, the total gauge-invariant phase difference $\varphi = 2\pi n$. Therefore we find, from Eqn 2.20,

$$2\pi n = \varphi_2 - \varphi_1 - \frac{2\pi}{\Phi_0} \oint_C \mathbf{A} \cdot d\vec{l} \tag{5.1}$$

where φ_n is the phase difference in the nth Josephson junction. The integral of the vector potential along the enclosed path yields the flux within the loop, and thus Eqn 5.1 can be

simplified as

$$\phi_2 - \phi_1 = 2\pi n + \frac{2\pi\Phi}{\Phi_0}. \tag{5.2}$$

From the discussion in Section 2.4, we know the current-phase relationship is

$$J_n = J_{C_n} \sin\phi_n \tag{5.3}$$

with total current

$$\begin{aligned} J &= J_{C_1} \sin\phi_1 + J_{C_2} \sin\phi_2 \\ &= J_{C_1} \sin\phi_1 + J_{C_2} \sin\left(\phi_1 + \frac{2\pi\Phi}{\Phi_0}\right). \end{aligned} \tag{5.4}$$

If we maximize this current with respect to phase, and consider the simplest case where $J_{C_1} = J_{C_2}$, we can find the superconducting current in the loop and the external magnetic flux are related by

$$J = 2J_C \left|\cos\left(\frac{\pi\Phi}{\Phi_0}\right)\right|. \tag{5.5}$$

This result implies that the supercurrent in a SQUID will oscillate from a maximum to a minimum within one flux quantum, $\Phi_0 = \frac{h}{2e} = 2.0678... * 10^{-15}$ Wb! With practical DC SQUIDs, changes as low as $10^{-6}\Phi_0$ can be detected [84].

5.2.2 SQUID Current Comparator Circuit

With sensitivity at this level, it's no surprise SQUID circuits have found their way into measurement systems. For our experiments, we use an RF SQUID [85]. Still a very sensitive

device, capable of measuring changes in flux down to $10^{-5}\Phi_0$, RF SQUIDs differ in their measurement scheme compared to that of DC SQUIDs mentioned above. RF SQUIDs couple a single Josephson junction to an LC circuit. An oscillating current in the inductor generates an oscillating voltage in the SQUID, which is periodic in applied flux (Φ) with a period Φ_0.

Our system uses a Quantum Design 2010 SQUID Control that talks to the SQUID in the Quick Dipper, trying to keep the voltage across the sample and reference resistor equal. As the current through the pillar exceeds the critical current, a voltage drop develops in the sample. This, in turn, generates a current in the loop created by the sample (R_s), the reference resistor (R_{ref}), and the inductor between them (see Figure 5.1). Through the transformer that couples this loop to it, the SQUID loop experiences a change in magnetic flux, which is read in the electronics box.

In an attempt to cancel this flux, the SQUID electronics box outputs a voltage which, after dropping across the feedback resistor (R_{FB}), drops across R_{ref}. The electronics box tunes the voltage in R_{ref} until it exactly matches that which is across R_s, which eliminates the current in the inductor. By measuring the output voltage of the SQUID electronics and knowing that (for QD-II) $R_{ref} = 126\mu\Omega$ and $R_{FB} = 2\text{k}\Omega$, we can determine the voltage in the sample by

$$\begin{aligned} V_s &= V_{out}\frac{R_{ref}}{R_{ref}+R_{FB}} \\ &\approx V_{out}\frac{R_{ref}}{R_{FB}}. \end{aligned} \tag{5.6}$$

5.3 System

With the complexities of the Quick Dipper and the SQUID device covered, the rest of the measurement system is relatively straight forward and is depicted in Figure 5.5.

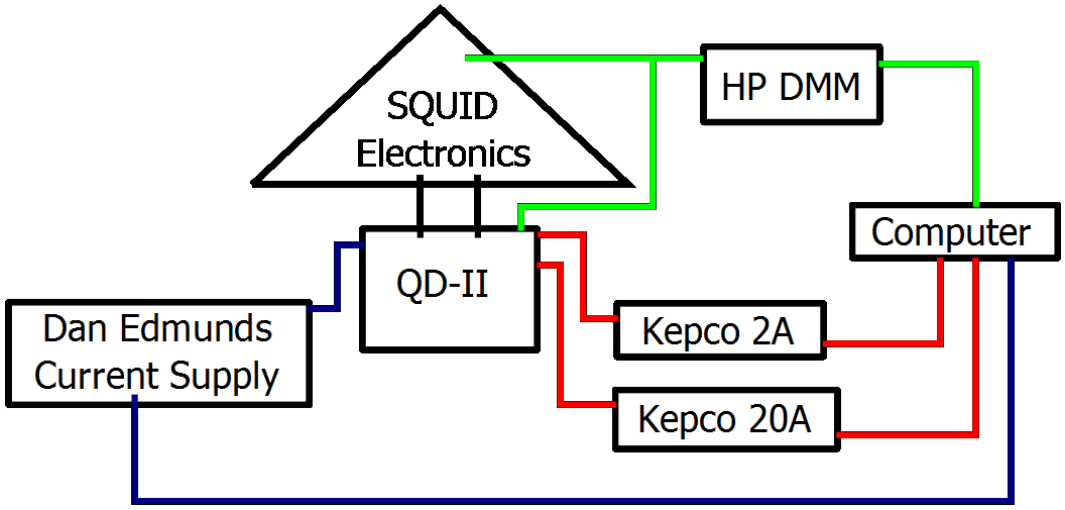

Figure 5.5 *Schematic of measurement set-up.* Color code: red wires – magnetic control; blue – current control; green – SQUID output/voltage measurement.

The external current to the sample is supplied by an analog power supply driven by 12V motorcycle batteries. These are very stable as long as they are charged, which is done continuously when not operating. During operation, the charging adds a little noise, so for very sensitive measurements it is advantageous to disconnect the batteries from the charging source. This power supply system was created in house by Dan Edmunds.

As the current increases and drives the sample normal, the SQUID Comparator Circuit adjusts its output to match that across the sample (as described in Section 5.2.2). The SQUID output voltage is measured with at HP 34401A digital multimeter which can be read by the computer.

The current is stepped with counterpart voltage read to measure an entire I-V curve for a specific magnetic field. This field is driven by supplying a current to the appropriate

magnetic coil (transverse or longitudinal) via the Kepco BOPs discussed previously (Section 5.1) and is read by the computer by passing the current through a small resistor (0.1 Ω or 0.01 Ω) and measuring the voltage drop with a Fluke 45 Digital Multimeter.

When adjusting the field, a small amount of heat is applied to the persistent switch, driving it normal and passing the current into the magnetic coils. This is turned off once the desired field is reached, limiting the fluctuations and noise from the magnetic field current within the measurement.

Once completed, the magnetic field is stepped and a new curve is measured, which is done repetitively until an I-V curve is taken for the entire range of desired external magnetic fields. These data can then be analyzed and fit to the appropriate function (as shown in Eqn 2.38) to find the critical current for each curve. Plotting I_c vs $\mu_0 H$ yields the Fraunhofer pattern for the sample in its current magnetic state, which can then be adjusted (i.e. magnetization rotated) and the process repeated to determine a new pattern.

All of the measurements, as well as critical current extrapolation program, are automated with LabVIEW programs developed in house. These were originally programmed by Nate Verhanovitz and later modified by Trupti Khaire, Yixing Wang, Eric Gingrich and myself. This automation, besides alleviating the monotony of the routine, is particularly important when considering the persistent switch control. Without appropriate current matching before and after opening, the persistent switch can vaporize, rendering the dipper little more than an elongated paper weight until it is repaired.

Chapter 6

Characterization

While evidence of spin-triplet switching should be clear in the data, we must be careful as other effects could give a similar signature. To be sure that the cause of the supercurrent modulations are due to the rotation of an individual layer's magnetization, it is important to characterize the properties of the various materials.

6.1 Use of NiFe

The first samples made for this experiment had NiFeMo as the soft ferromagnetic layer, characterization of which was discussed in Section 3.3.2. Addressed in Section 7.3.3, these samples had NiFeMo as both spin mixer layers. Presumably, if the magnetizations of both layers rotated, the effect would be quite large. However, samples made with this material did not behave quite right for two reasons: the field necessary to rotate NiFeMo in the full system seemed to be a bit higher than expected and any form of switching seemed to be very messy; also, the signal was very small. At this point, NiFe was considered as a spin-mixer, but in order to justify its use, it needed to be characterized as the NiFeMo had been.

6.1.1 Generation

In order to compare the spin-triplet generation capabilities of NiFe to NiFeMo, the sample geometries and structure (material thickness, etc) had to match. With this in mind, samples

of Nb(150)/Cu(5)/Ni(1.2)/Cu(5)/Co(6)/Ru(0.75)/Co(6)/Cu(5)/NiFe(x)/Cu(5)/Nb(20)/Au(15)/Nb(150)/Au(10) were fabricated using the group's standard photolithography pattern, where x varies from 0.8-2.4 nm. With this mask, 6 circular pillars (diameters of 3 μm, 6μm, 2x 12μm, 24 μm, 48 μm) are milled from a wide base lead (300 μm). While there are a number of differences between this structure and those used in the final experiment, the relative amount of spin-triplet we can generate is not affected by any of these differences.

Due to fabrication issues, not every pillar had acceptable normal state resistances. However, every NiFe thickness had at least one pillar that was measurable, allowing for a complete mapping of the spin-triplet generation for these thicknesses.

In the same manner the data in Section 3.3.2.1 were taken, a Fraunhofer pattern was measured for each NiFe thickness. An example of these measurements is shown in Figure 6.1. Due to the softness of the NiFe and the size of the pillar, we believe much of the noise in the pattern is due to domains rotating independently through the sweep as opposed to all at once. However, the expected width of the central peak is about 8 mT, so the minima of the black curve at 1.2 and -6 mT likely define the central lobe of the Fraunhofer pattern.

The maximum measured critical current is taken from each measurement, multiplied by the sample's normal state resistance, and plotted against thickness of the NiFe (Figure 6.2). As expected, the $I_c R_N$ decays with increasing NiFe thickness. The decrease at low thicknesses is due to a lack of magnetization for NiFe thicknesses of less than 1.0 nm, similar to what was observed in NiFeMo samples (see Section 3.3.2.1).

It is likely that the values obtained from these data are less than the maximum possible critical current due to the poor quality of the Fraunhofer patterns. However, because this measurement is intended to determine the optimum NiFe thickness to generate spin-triplet Cooper pairs, this underestimate is not likely to alter the trend and not a major concern.

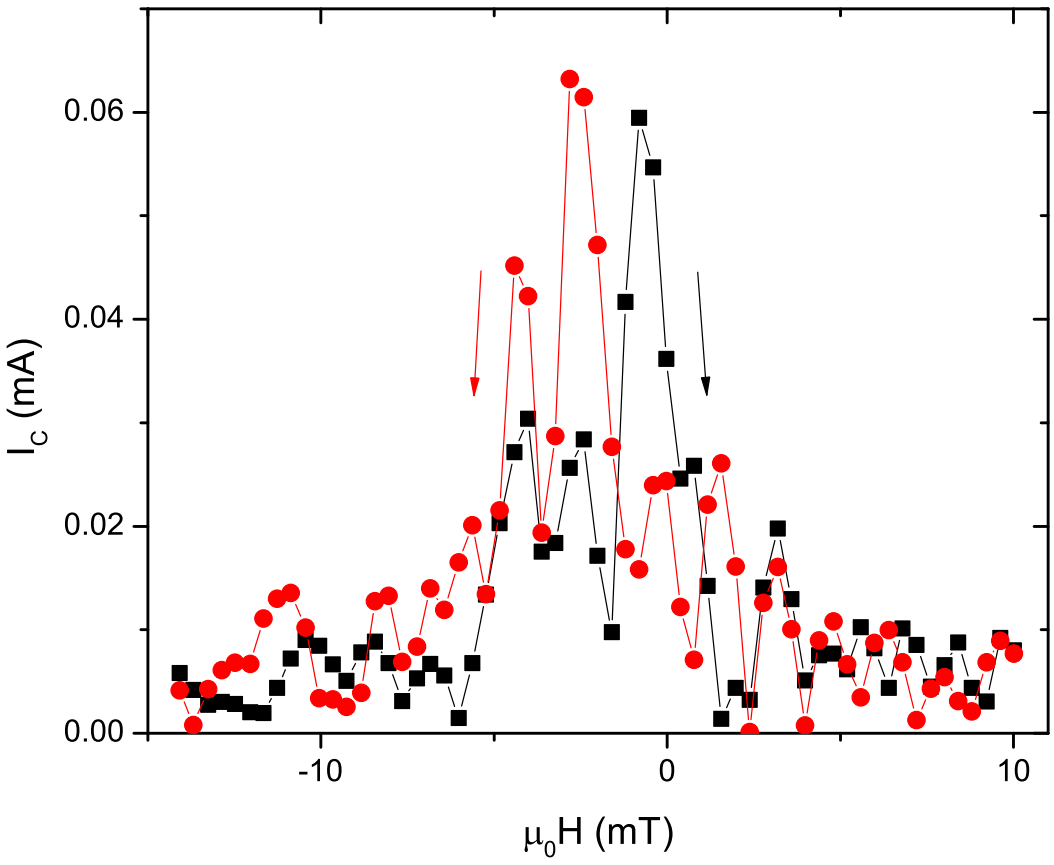

Figure 6.1 *Example of Fraunhofer pattern for NiFe generation samples.* The red and black curves represent Fraunhofer patterns taken with different magnetic-field-sweep directions, as depicted by arrows. Composition: Nb(150)/Cu(5)/Ni(1.2)/Cu(5)/Co(6)/Ru(0.75)/Co(6)/Cu(5)/NiFe(0.8)/Cu(5)/Nb(20)/ Au(15)/Nb(150)/Au(10).

From the data, we choose a 1.0 nm as the optimum NiFe thickness.

6.1.2 Switching Field

With the thickness determined, the next thing to figure out is how large an external field is required to rotate 1.0 nm NiFe. The easiest way to measure this property, as seen in Section 3.3.2.2, is by fabricating elliptical pillars and measuring Fraunhofer patterns in fields along the long axis of the ellipse. These samples had the same geometry as those discussed in Section 3.3.2.2 as well, so the confined magnetization was still useful (see Figure 3.7).

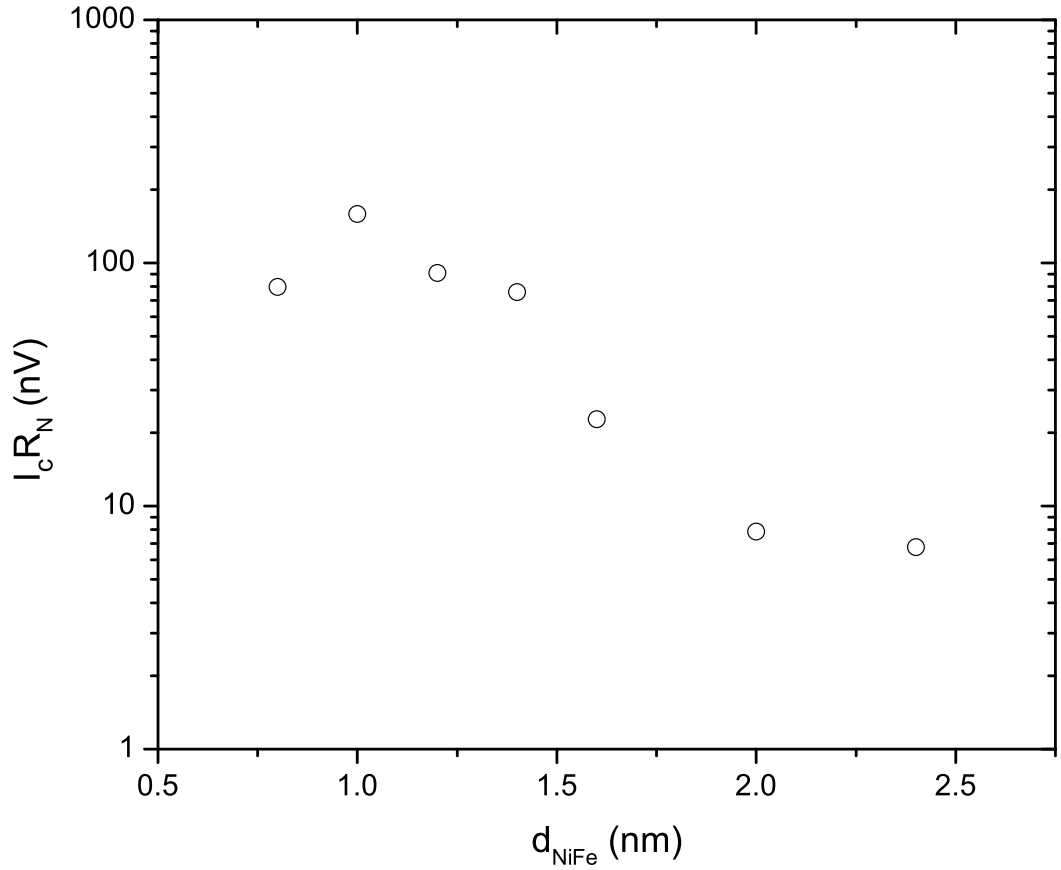

Figure 6.2 I_cR_N *vs NiFe Thickness.* Composition: Nb(150)/Cu(5)/Ni(1.2)/Cu(5)/Co(6)/Ru(0.75)/Co(6)/Cu(5)/NiFe(x)/Cu(5)/Nb(20)/Au(15)/Nb(150)/Au(10). $0.8nm \leq x \leq 2.4nm$.

One major difference between these measurements is that, because these were spin-triplet samples, they had three magnetic layers (here, and elsewhere in this thesis, we are considering the Co/Ru/Co synthetic antiferromagnet (SAF) to be a single layer), with non-collinearity between adjacent layers generating the measured supercurrent. All magnetizations would point along the long axis if patterned as an ellipse, so only the top NiFe could be patterned. This resulted in less clear switching signatures, which can be seen in the data. However, because the NiFe should still switch abruptly, its switching field is still evident. This is shown in Figure 6.3; there is a rather clear change in critical current around -10 mT (10 mT) in the negative (positive) sweep direction.

6.2 Co/Ru/Co

As important as it is to determine the field required to rotate NiFe, it is equally important to determine how much field can be applied without rotating the Co/Ru/Co synthetic antiferromagnet (SAF). A SAF is a multilayer of two ferromagnets separated by a thin non-magnet, typically a normal metal (Figure 6.4). Due to the band structure of Ru, there exists a long range exchange coupling between Co layers, causing them to align anti-parallel [86].

In an external field, the magnetic layers will start to bend in the direction of the field. If strong enough, this will cause the magnetization to point in a scissor-like manner in the direction of the field. As the field is turned down, the scissoring between layers will release and the magnetization will realign anti-parallel to each other. This process, known as spin-flopping, will cause the magnetization of the two ferromagnetic layers to align perpendicular to the direction of the external field, as shown in Figure 6.5.

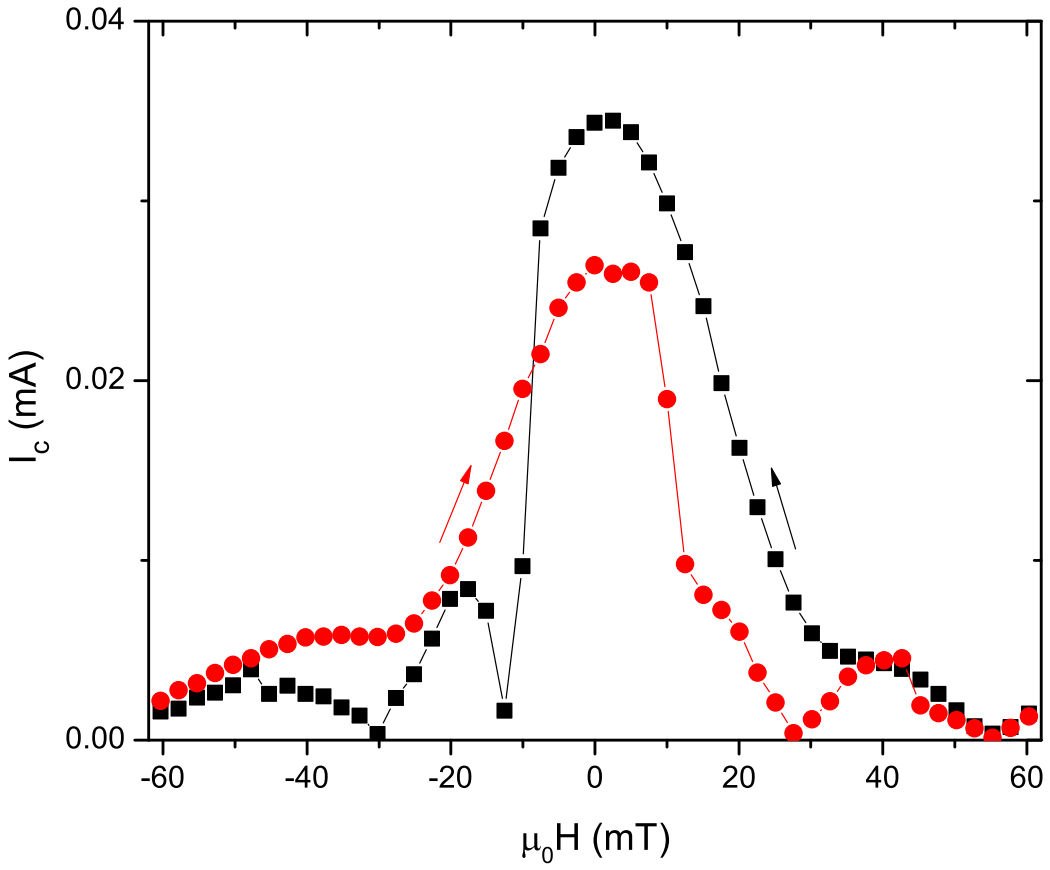

Figure 6.3 *NiFe switching field.* The abrupt drop in critical current is due to the NiFe ellipse flipping magnetization direction. The black curve is measuring from 60 to −60 mT while the red curve is opposite. Composition: Nb(150)/Cu(5)/Ni(1.2)/Cu(10)/Co(4)/Ru(0.75)/ Co(4)/Cu(10)/NiFe(1)/Cu(5)/Nb(20)/Au(15)/Nb(150)/Au(10).

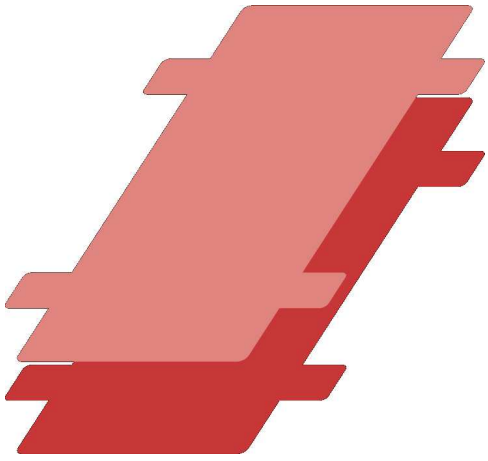

Figure 6.4 *SAF cartoon.* The cutaway shows the two Co layers. Ru layer not shown.

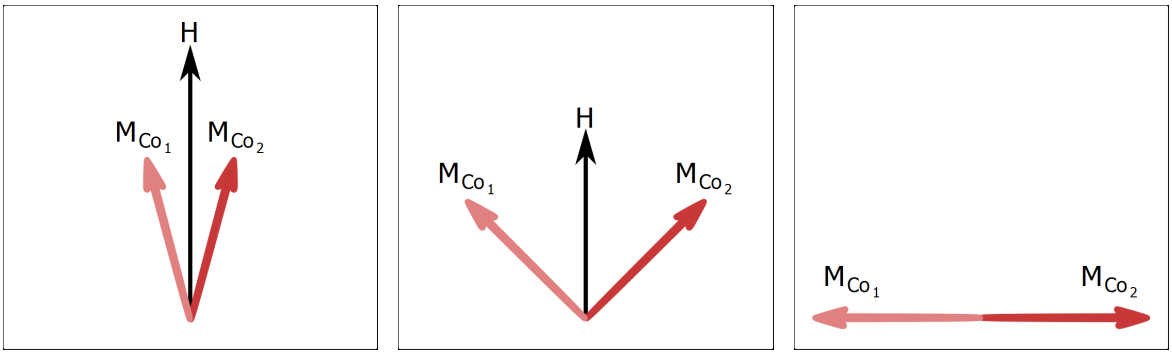

(a) SAF scissoring with large external field.

(b) SAF starting to spin-flop with reduced external field.

(c) Full anti-alignment after external field removed.

Figure 6.5 *Spin-flop mechanism.* In a large enough external magnetic field, SAF magnetizations scissor in the direction of the field. As the field decreases, the SAF starts to release, flopping anti-parallel with each other until the field is completely gone and the magnetizations are anti-aligned. The final orientation of the magnetizations is independent of their initial orientations, but rather depends only on the direction of $\vec{H}$

6.2.1 Anisotropic Magnetoresistance

To measure the rotation of the SAF due to external field, we rely on a phenomena known as anisotropic magnetoresistance (AMR). This arises from the interplay between the magnetization of the material and the spin-orbit interaction of the current. In short, the resistivity (ρ), and thus resistance, of the material is dependent on the angle between the magnetization and current (φ),

$$\rho(\varphi) = \rho_{\perp} + (\rho_{\parallel} - \rho_{\perp}) \cos^2 \varphi. \tag{6.1}$$

The resistance is maximum for parallel orientation and minimum for perpendicular orientation.

Because of the spin-flop mechanism in the SAFs, this means that an external field parallel (perpendicular) to the current will result in perpendicular (parallel) magnetization. This is demonstrated in Figure 6.6. Also shown is the mounting in a standard 4-terminal measurement of a sample with this geometry.

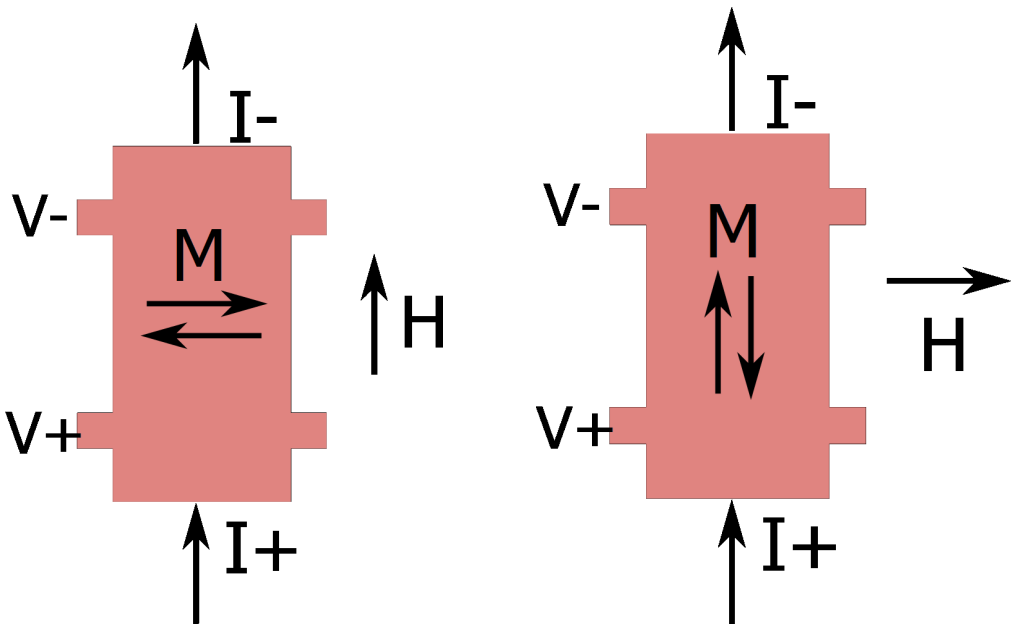

(a) SAF magnetization perpendicular relative to current due to longitudinal (y-) field.

(b) SAF magnetization parallel relative to current due to transverse (x-) field.

Figure 6.6 *Cartoons of SAF magnetization due to field.* I±, V± shown to indicate mounting geometry for resistance measurements.

6.2.2 AMR Procedure

Measurements of AMR are no more complicated than applying a known current and measuring the voltage response of the sample. To see the difference as the SAF rotates, a magnetic field can be applied and removed, measuring the change in output voltage caused by the field. The system is initialized in a 260 mT field (the same field our on/off-control samples will be initialized at) but only measured up to 160 mT, the maximum field of the transverse coil.

The current to the sample is driven from the output voltage of a lock-in amplifier (Stanford Research Systems Model SR830 DSP) connected to a variable ballast resistor. By measuring the output voltage, the resistance is simple to determine with Ohm's Law: $R = \frac{V_{out}}{I_{in}}$. However, the difference of resistance with parallel current-magnetization orientation ($R_{\parallel}$)

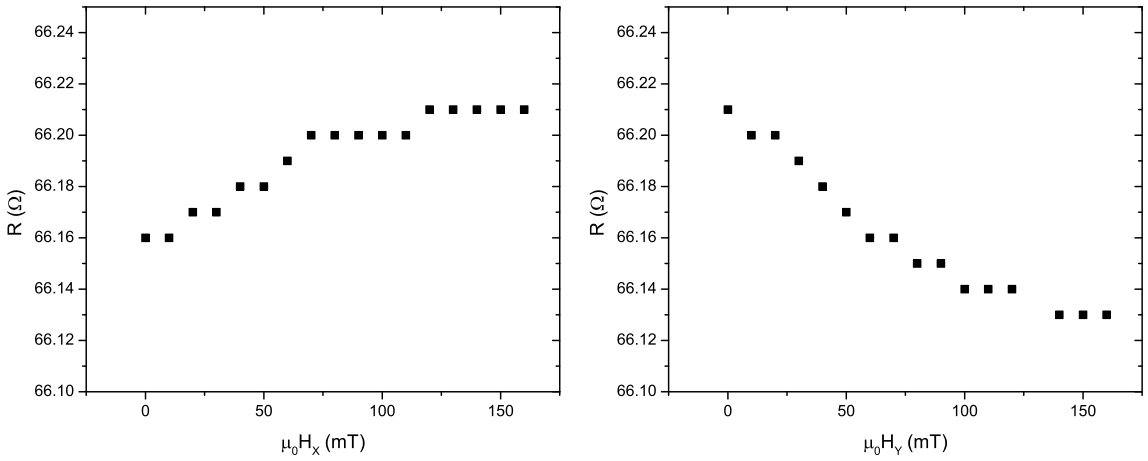

(a) AMR with increasing perpendicular field. (b) AMR with increasing parallel field.

Figure 6.7 *Resolution issues of lock-in amplifier.* Minor changes in the sample resistance are masked by the sensitivity ceiling of the lock-in.

and resistance of the perpendicular orientation ($R_\perp$) is very small, between 0.05% and 0.6%, depending on the Co thickness. Therefore, the resolution of the lock-in amplifier is 1 part per 10,000, or 0.01%. While the overall trend is measurable, minor changes in the resistance as the field increases can go unnoticed (see stepping signature in Figure 6.7).

To obtain better resolution, a ratio transformer (Singer RT-61) is connected to the circuit as a voltage divider. The result is a subtraction of the normal output voltage measured at the sample. By removing most of the signal, the sensitivity of the lock-in amplifier can be increased, measuring to far better resolution. The circuit diagram for this set-up is demonstrated in Figure 6.8.

6.2.3 AMR Data

Now that the measurement system is tuned, samples of various Co thicknesses can be measured. Fabrication of these samples used a mechanical mask to define the sample geometry. Samples were grown with structure of Nb(2.5)/Cu(3)/Co(x)/Ru(0.75)/Co(x)/Cu(3)/ Nb(2.5), where x is 2, 4, 6, or 8 nm. The copper layers are necessary in fabrication, as Co

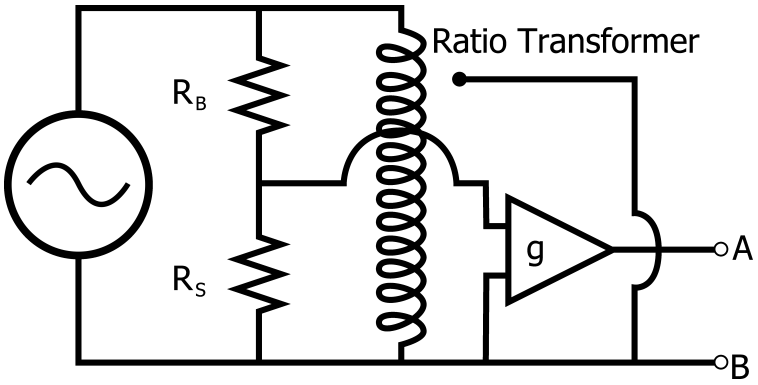

Figure 6.8 *Circuit diagram of a ratio transformer.* A and B go to the input terminals of a lock-in.

grows smoother on Cu than on Nb. They are, though, kept thin to limit parallel channels for the current. Niobium is also kept thin to prevent it from becoming superconducting. Two samples of each thickness were made, and one sample of each was grown in an external magnetic field while the other was not. Because all of our on/off-control samples are grown in a field, it is useful to know the difference (if any) an external field has.

The data is plotted in Figures 6.9 and 6.10. A field is applied in either the perpendicular or parallel direction, then removed. In zero field, resistance is measured and plotted relative to the field applied. Initially, a large (260 mT field) is applied parallel to I, initializing the system in the way control samples are measured (see Chapter 7). The field is stepped in 10 mT increments to 160 mT, first in the perpendicular direction, followed by the parallel direction (black curves). To obtain more resolved data at low fields, the process is followed again with smaller steps for small fields (red curves).

From the data, it is evident that rotation of the SAF is a true concern, especially as the thickness increases. It also appears that growing in a field softens the SAF (makes it easier to rotate), but the cause of this is not entirely understood. Keeping the SAF thin is important, but if it's too thin, the suppression of spin-triplet supercurrent will be too weak.

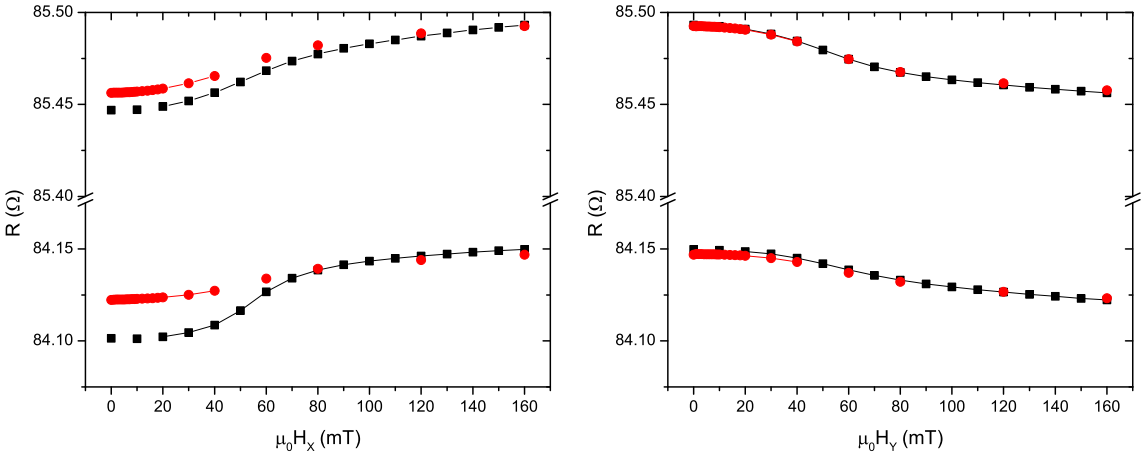

(a) Co(2) with H applied perpendicular to I. Upper curves were grown in a magnetic field.

(b) Co(2) with H applied parallel to I. Upper curves were grown in a magnetic field.

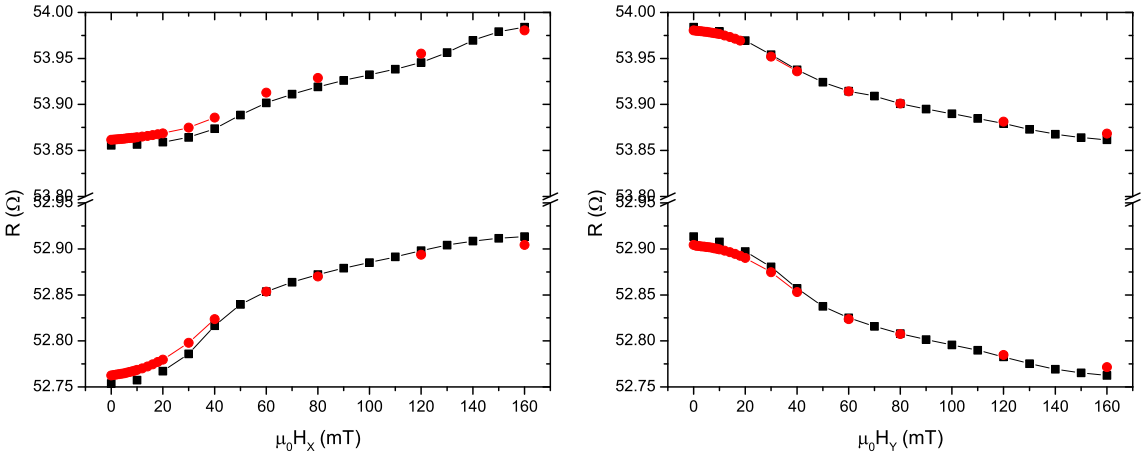

(c) Co(4) with H applied perpendicular to I. Lower curves were grown in a magnetic field.

(d) Co(4) with H applied parallel to I. Lower curves were grown in a magnetic field.

Figure 6.9 *AMR data for Co(2) and Co(4).* Each measurement was undertaken twice, starting with the black curve.

For the work described herein, a Co thickness of 4 nm was chosen as a good balance between hardness and thickness.

There is a slight difference for some samples between the first and second measurement (black and red curves, respectively), but only in the perpendicular direction (i.e. the first time it is rotated). We believe this is due to slight changes in the domain structure of the bulk sheets of Co. The system is first initialized in the parallel state to large (260 mT) fields, but any domain changes as the SAF is rotated up to 160 mT may not reinitialize

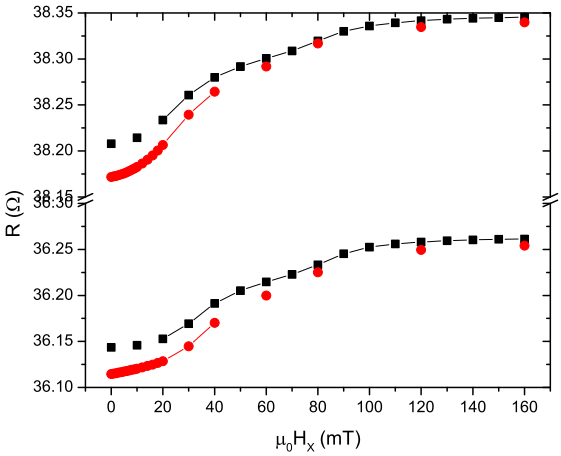

(a) Co(6) with H applied perpendicular to I. Upper curves were grown in a magnetic field.

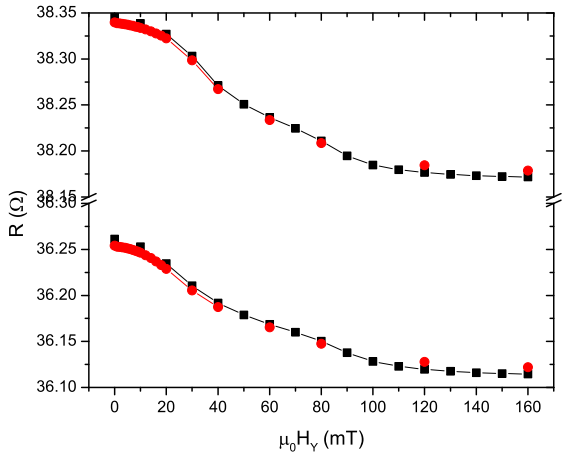

(b) Co(6) with H applied parallel to I. Upper curves were grown in a magnetic field.

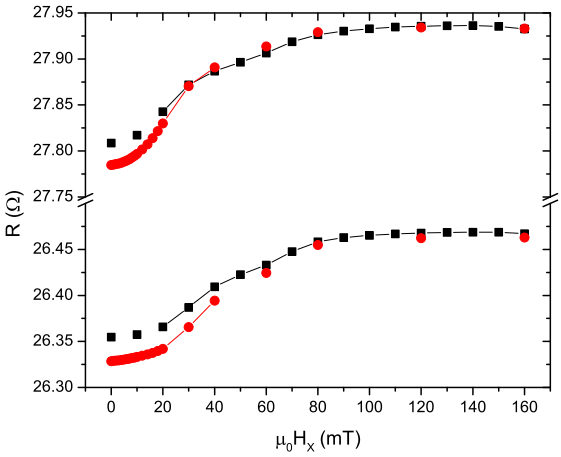

(c) Co(8) with H applied perpendicular to I. Upper curves were grown in a magnetic field.

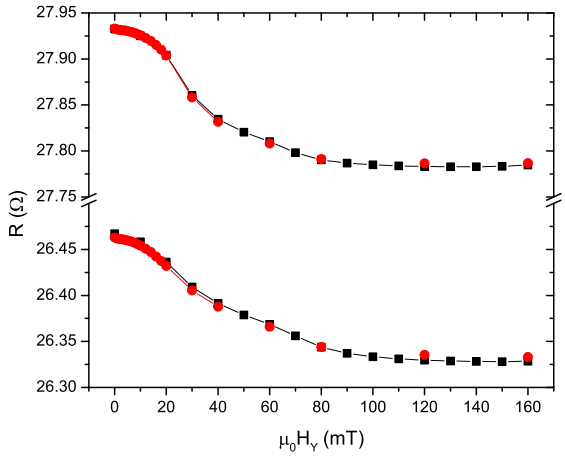

(d) Co(8) with H applied parallel to I. Upper curves were grown in a magnetic field.

Figure 6.10 *AMR data for Co(6) and Co(8).* Each measurement was undertaken twice, starting with the black curve.

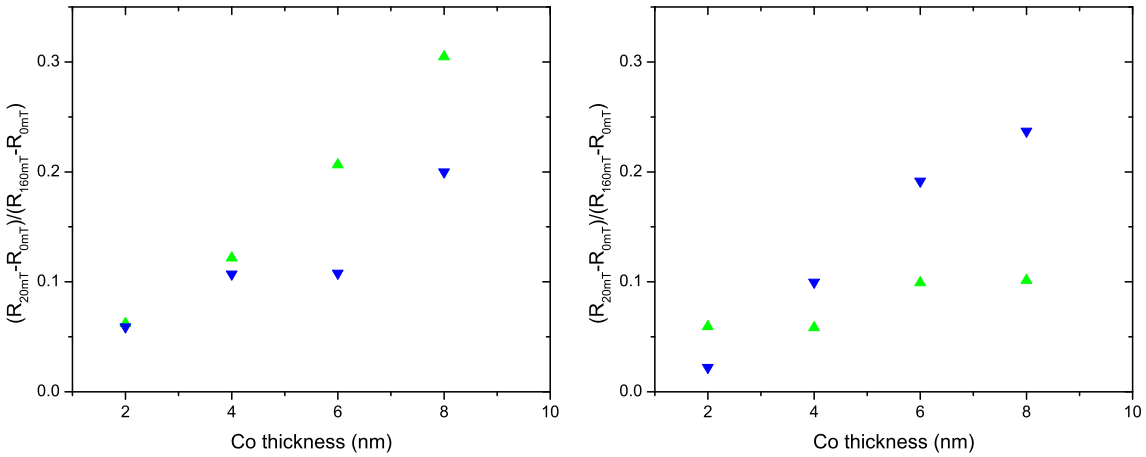

(a) Summary of samples grown in a magnetic field.

(b) Summary of samples grown in the absence of a magnetic field

Figure 6.11 *AMR Summary.* The relative percent change in resistance in the first 20 mT compared to the full 160 mT. Only the second run of each sample is used for calculations. Green: H⊥I; Blue: H∥I.

fully. However, the data seems reproducible after the first rotation, evident in the first and second parallel measurements aligning.

Since we can rotate the NiFe within the first 20 mT, knowing the relative rotation of the SAF is useful within that range. Calculating the resistance change in the first 20 mT relative to the full 160 mT, we can obtain a percent change, which is plotted in Figure 6.11. Due to the slight differences of the measurements, as noted above, only the second sweep values were used in these calculations.

It is clear that rotation of the SAF is a real concern when measuring these samples. It seems as though any field, even if very low, is enough to move the magnetization a little bit. While the effect is smaller for thinner Co, and relatively small if the field is kept below 20 mT, it appears that the magnetization will never be fully stable. This means that the magnetization directions of adjacent layers may never be completely collinear, and therefore the spin-triplet pair correlations may never fully vanish. However, if the rotation is kept small, the amplitude of pair correlations should also be very small, and therefore we should

be able to realize amplitude control in S/F/S Josephson junctions.

Chapter 7

Control of Spin-Triplet Supercurrent

To better understand the data presented here, this chapter will begin with a discussion of the procedure followed to measure our samples. Afterwards, to jump directly to the successful samples and data, which show the ability to control the spin-triplet supercurrent in S/F/S Josephson junctions, would leave many unanswered questions as to how the decisions leading to those samples were made. The initial efforts and stumbles that directly led to our successes will be discussed in the first section. The final data will follow.

7.1 Procedure

Because so much of the following discussion relies on rotating magnetic layers, it is useful to talk about the measurement procedure here. This section, with the aid of cartoon representations, will hopefully help the reader become familiar with the potentially confusing discussion about magnetization direction.

7.1.1 Initial Fraunhofer Pattern

The system is first initialized by applying a large magnetic field (260 mT) longitudinally along the sample. This aligns the Ni and NiFe magnetizations in the direction of the applied field, while the Co/Ru/Co SAF spin flops so that each layer's magnetization is perpendicular to the applied field, as depicted in Figure 7.1. Because adjacent magnetization layers

are perpendicular to each other (Ni $\perp$ Co/Ru/Co $\perp$ NiFe), there is maximum spin-triplet generation and thus the pillar initiates in the on state.

A magnetic field of this size is large enough to trap some flux in the Nb top and bottom leads, adding an unknown element to our measurements (not to mention making the Fraunhofer pattern look lousy). To remove the trapped flux, we slowly raise the dipper slightly out of the helium to allow the Nb to go normal, verified by measuring sample resistance with a hand-held digital multimeter (DMM). As soon as the Nb goes normal, the sample resistance jumps up, at which point the DMM is removed and the sample is redipped into the dewar. Although this step seems unsophisticated, it is not a careless one as it is vital that the temperature of the sample be kept as cold as possible. Raising the temperature above the Curie temperature of any magnetic layer will cause it to lose its magnetization, forcing the user to re-initialize and remove flux again.

At this point, a simple Fraunhofer measurement is taken from 20 to -20 mT and back again (assuming initial magnetization was positive, order of sweeps flipped if negative). This is done to make sure the sample is behaving normally as judged by a number of its characteristics: that the peak of the Fraunhofer pattern has a large enough critical current and isn't shifted too far off center, that the normal state resistance matches what had been previously measured, that it responds to a magnetic field, and that is shows signs of switching the NiFe magnetization direction 180 degrees (see Figure 7.1c). If any of those criteria are not met, the sample is reinitialized and measured again. If the results consistently show poor behavior, the sample is removed and a new sample is mounted instead.

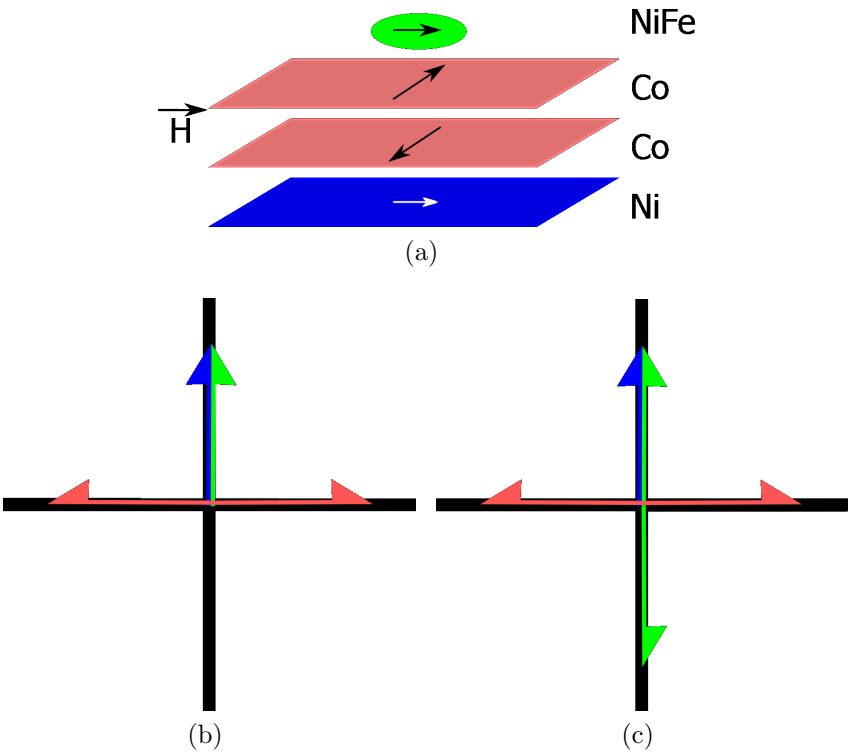

Figure 7.1 *Representations of magnetization direction in the on state.* Blue: Ni; Pink: Co/Ru/Co SAF; Green; NiFe. (a) represents a skewed view of the stack, while (c) and (d) represent the top-down view. (d) also shows the switching of the NiFe as it switches in positive and negative field, but remaining orthogonal to the SAF.

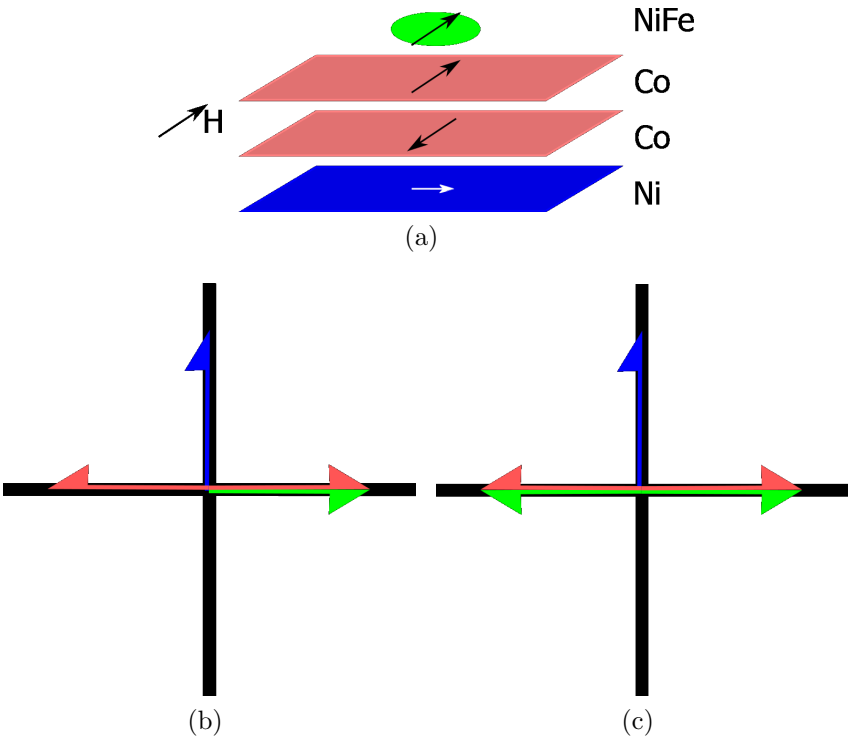

Figure 7.2 *Representations of magnetization direction in the off state.* Blue: Ni; Pink: Co/Ru/Co SAF; Green; NiFe. (a) represents a skewed view of the stack, while (c) and (d) represent the top-down view. (d) also shows the switching of the NiFe as it switches in positive and negative field, but remaining parallel to the SAF.

7.1.2 Switching: Zero-Field Measurements

At this point, the critical current at zero field should be large and near the peak of the Fraunhofer pattern. As we rotate the NiFe 90° to become parallel with the Co/Ru/Co SAF (Figure 7.2), the spin-triplet component, and thus the total critical current, should drop dramatically. To check for this, we apply a magnetic field in the transverse direction and measure the critical current at zero field. As the magnetization starts to rotate, the critical current should drop until it floors (when the pillar is fully rotated).

The exact same procedure is done in reverse to measure the rotation of the NiFe as a longitudinal field is applied. In this case, as the NiFe rotates back to its initial direction, the critical current should increase until it levels off at a maximum. This is when the pillar is fully rotated longitudinally, bringing the system back to its on state.

7.1.3 Switching: Fraunhofer Measurements

To better compare with the initial data, this same rotation is measured as a Fraunhofer pattern. If successful, the critical current should drop as the transverse field is increased. At which point, a full sweep can be taken to show that the sample stays low during the entirety of the sweep. This sweep done in the off state should show a dramatic difference when compared to the initial (on-state) Fraunhofer pattern.

For completeness, this same measurement is done again in the longitudinal direction. The critical current should start in a low state, eventually rotating to the high state at higher fields. After rotation, the critical currents in the Fraunhofer pattern should be much larger than in the off state, and if done fully without effecting other magnetization layers, this final pattern should match the initial pattern taken.

7.1.4 On/Off Switching

While the above should be enough to demonstrate the switching capabilities of the pillars, one final measurement is undertaken: measuring only the critical current after each iteration of switching the spin-triplet supercurrent on and off. To do this, a field large enough to switch the NiFe (as measured in Section 7.1.2) is applied, alternating between the longitudinal and transverse directions. Effectively, this should turn the spin-triplet on and off, resulting in a large and small critical current, respectively, when measured in zero field. If the sample is behaving properly, the critical currents should also be reproducible between concurrent on (off) measurements.

7.2 Right Place at the Right Time

As mentioned numerous times already, the work discussed herein requires rotating the magnetization of specific ferromagnetic layers between two axes. A main reason it had never been attempted before, despite the pioneering spin-triplet pair correlation work and discovery 4 years prior (see Section 3.2), is that we had no way to control an external magnetic field in two directions. Therefore the importance of QD-II and its ability to generate the necessary magnetic fields (as discussed in Section 5.1) cannot be overstated. Finishing the magnetic wiring of the probe, completed just before the onset of this project, was the key to opening this area of investigation.

Another facet that allowed for relatively rapid results is that spin-triplet supercurrent has been a major focus of the group recently, meaning much of the work necessary to optimize the fabrication, magnetic layer characterization, etc. had been done previously. While individual

aspects still needed to be taken further (see Chapter 6), a lot of the details had been fine tuned prior to my initial involvement.

7.3 Early Attempts

7.3.1 Rotate the SAF

Knowing it to be naive, the first attempt to measure control of the spin-triplet was done with samples made by Yixing Wang that had Ni for both spin-mixer layers and a Co/Ru/Co SAF as the central ferromagnet [Nb(150)/Cu(5)/Ni(1.2)/Cu(5)/Co(6)/Ru(0.75)/Co(6)/ Cu(5)/Ni(1.2)/Cu(5)/Nb(20)/Au(15)/Nb(150)/Au(20)]. Aware of the magnetic hardness of Ni, as it requires a field >200 mT to fully initialize the magnetization direction, the hope was to rotate the SAF, causing the Co/Ru/Co to spin flop parallel or perpendicular to the Ni, and thus putting the junction into an off or on state, respectively.

I claim this was a naive task, but in reality it was undertaken with a bit of forethought. First off, we already had access to samples like this. *If* this type of sample worked, there would be no reason to spend time fabricating duplicates. Secondly, while we were not expecting them to work outright, we hoped we would discover potential concerns and be able to ameliorate them while fabricating the next samples.

What we found was a promising trend without concrete results. The initial Fraunhofer patterns, Figures 7.3a and 7.3b, show that the flux produced by the Ni shifted the peak away from 0 mT. While we hoped to get a peak near 0 mT, we could always develop a program that allows us to measure in a small field and hit the peak. So instead of getting too concerned with that right away, we decided to press on with the rest of the measurements.

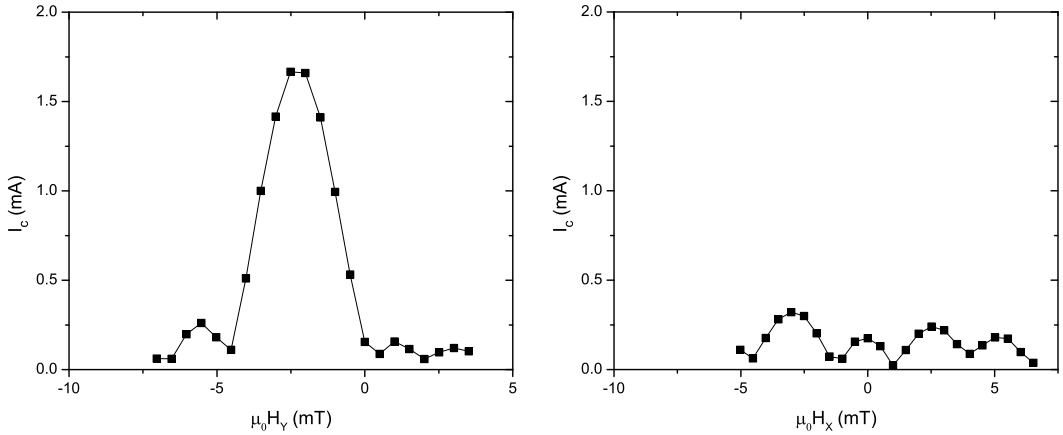

(a) (b)

Figure 7.3 *Initial Fraunhofer pattern measurements for Ni/SAF/Ni samples.* In (a) and (b), the field is applied in the on and off directions, respectively.

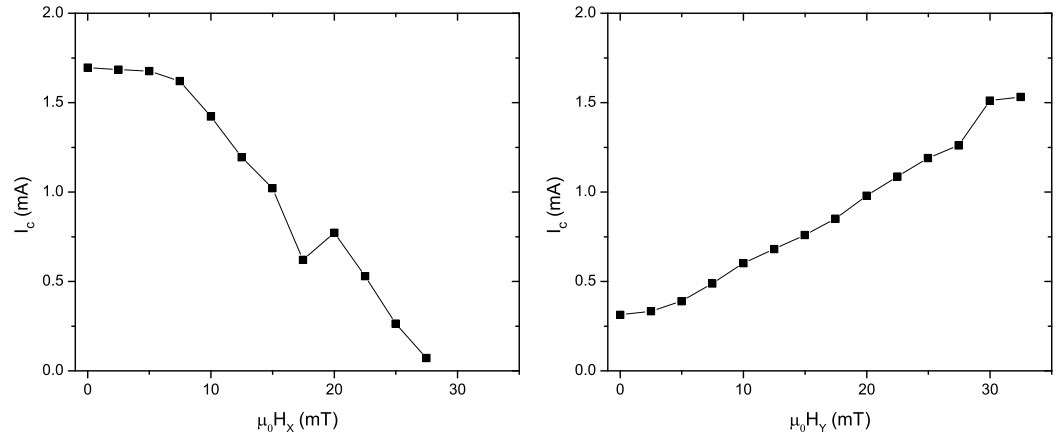

(a) (b)

Figure 7.4 *Initial switching behavior of Ni/SAF/Ni samples.* All measurements are taken in zero field after a rotating field is applied in the x (a) or y (b) direction.

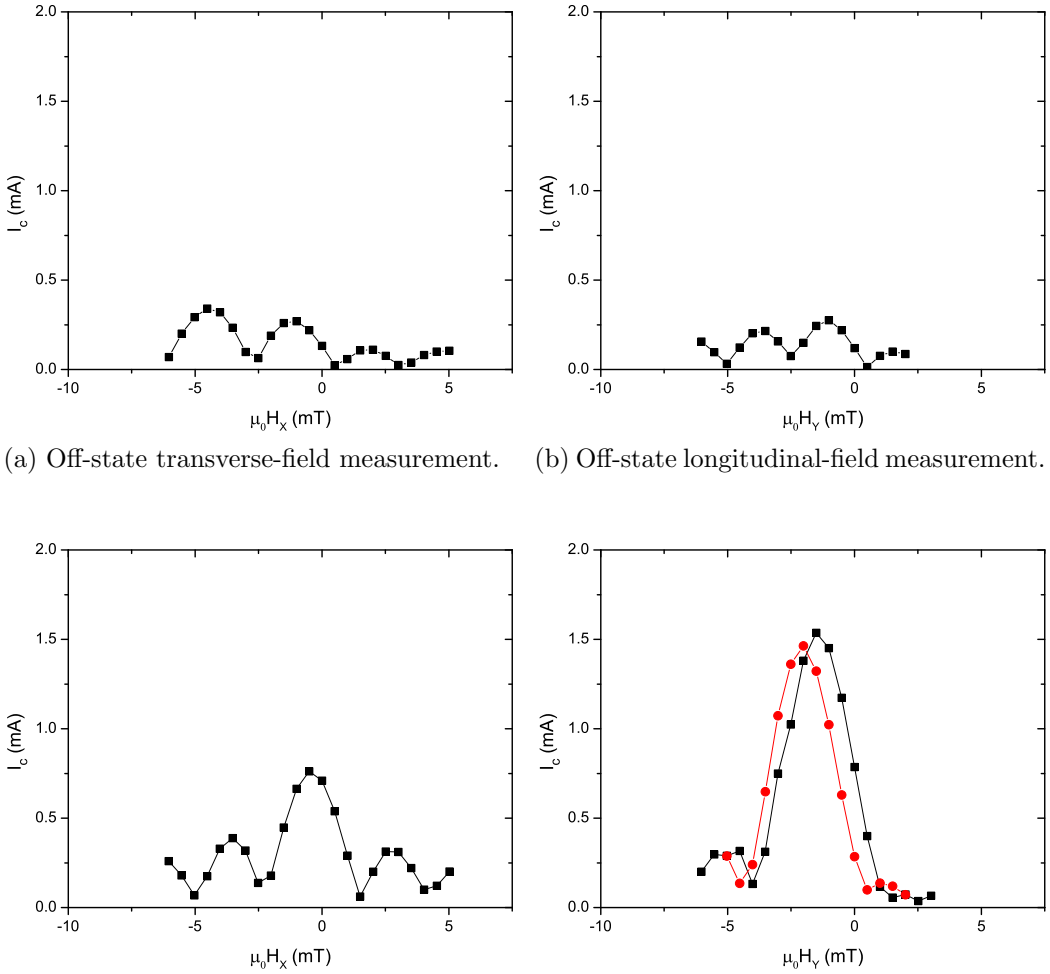

(a) Off-state transverse-field measurement.

(b) Off-state longitudinal-field measurement.

(c) On-state transverse-field measurement.

(d) On-state longitudinal-field measurement. The red and black curves are measured in the same sweep direction. The lack of overlap is evidence of some domain motion in the Ni.

Figure 7.5 *On- and off-state measurements for Ni/SAF/Ni samples.*

Measuring in zero field, we can see that the Fraunhofer pattern peak decreased with a large x-, or off-, field (Figure 7.4a), and increased again with a similar-magnitude y-, or on-, field (Figure 7.4b), as we hoped.

We had even been able to measure the Fraunhofer patterns in the low and high states, as shown in Figure 7.5. However, we didn't know enough about the stability of the nickel and how it is effected by fields as large as 30 mT. Could the behavior shown in Figure 7.4 be due to some combination of Ni and Co/Ru/Co rotation? Is there any way to be sure that

the Co/Ru/Co is rotated fully, either?

Running the final Fraunhofer pattern a second time, as shown as the red curve in Figure 7.5d tells us that we have enough Ni domains moving to cause a problem, as there is a shift in the peak (and zeros) between the two runs. Even if only a small fraction of domains rotated in that field, it is apparently enough to alter the internal flux of the junction, moving the central peak position. This appears as a decrease in critical current at zero field, in this case by a factor of roughly 3. Since our critical current is measured at a fixed field (typically 0 mT), movement of the Fraunhofer peak causes a lot of problems moving forward. To make sure we are always at the peak, we would have to map the entire 2-D field space for every measurement. Otherwise we could never be sure if we were controlling the spin-triplet supercurrent, as desired, or just moving the position of the central peak in the Fraunhofer pattern.

We knew that a full 2-D map wasn't feasible. So moving forward, although the data were not exactly what we hoped for, it did reveal the three main issues we knew we had to address:

1. Are we altering the Ni, the Co/Ru/Co, or both? Can we limit our rotation to only one of those?

2. Are we observing "switching" due to moving the central peak rather than tuning the spin-triplet supercurent?

3. Are the rotations clean enough to be sure minima are real and not just noise from individual domains moving around?

A solution to the first issue was simple, making it the obvious first one to try. The required field to fully rotate the Co/Ru/Co SAF was too high to be sure we weren't simultaneously

affecting the Ni, so it became necessary to incorporate a softer ferromagnet to rotate while leaving the others alone.

7.3.2 Large NiFeMo Pillars

Being undertaken concurrently with this project, other group members were looking at controlling the 0-π phase of ferromagnetic Josephson junctions, as mentioned in Section 3.3.2, measurable in superconducting SQUID loops. In junctions containing two or three ferromagnetic layers, the phase can be flipped by rotating one layer magnetization by 180° (Fig 2.12). Therefore the properties of soft ferromagents, such as the ability to generate spin-triplet supercurrent and the required switching field (the field necessary to flip the magnetization 180 degrees), were already being investigated (see Section 3.3.2). Of the sampled materials, NiFeMo pillars seemed to meet our needs as it generates enough critical current and has a low switching field. In the hope of revealing results, the decision was made to measure these samples [Nb(150)/Cu(5)/Ni(1.2)/Cu(10)/Co(6)/Ru(0.75)/Co(6)/Cu(10)/NiFeMo(1)/Cu(5)/ Nb(20)/Au(15)/Nb(150)/Au(20)] instead of fabricating new ones. While we still had other potential concerns (namely questions 2 and 3 above), if these samples worked, fabrication would again be unnecessary time and effort; if they didn't, perhaps we could figure out why and fix it while fabricating the next batch. Once again, this simple check revealed valuable information before making new samples.

As before, we see that the center of the Fraunhofer pattern is shifted from 0 mT, but now we can clearly see that the NiFeMo is flipping its magnetization direction. This can be seen in that the two longitudinal sweep directions (Figure 7.6a), one starting from -5 mT and increasing and the other from 2 mT and decreasing (direction denoted by colored arrows), have peaks that have moved relative to each other. As the NiFeMo switches, its

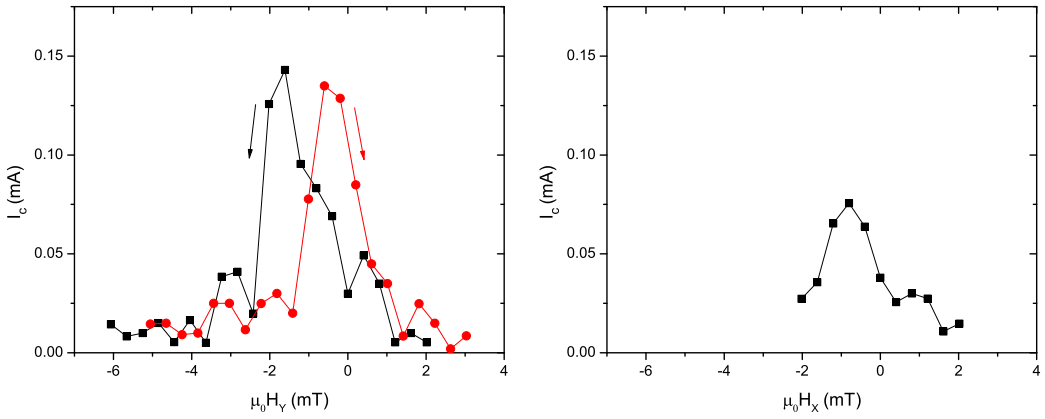

Figure 7.6 *Initial Fraunhofer pattern measurements for Ni/SAF/NiFeMo samples.* Both (a) and (b) are Fraunhofer patterns measured in the on state. However, due to the shift of the central lobe off of 0 mT [black curve in (a)], the measurement in the x-direction remained low the entire sweep.

magnetization will either add to that of the Ni, moving the shift further from 0 mT, or cancel it, bringing it back towards 0 mT. This is a promising result as it tells us that we are actually moving magnetization within the pillar, as desired. Again, the initial sweep in the transverse direction (Figure 7.6b) is low throughout, including at 0 mT, due to the shift of the peak off center.

Figure 7.7a shows the measurements of the critical current at 0 mT as we rotate the NiFeMo to the low state, while Figures 7.7b, and 7.7c show the Fraunhofer sweeps in the longitudinal and transverse directions. We once again can see some amount of 180-degree flip in the X-direction, but the size of this peak is troubling. We expected it to be low, assuming we had rotated the NiFeMo. Apparently, we may have just rotated it enough to have moved the peak, but not fully turned off the spin-triplet supercurrent.

When trying to rotate the NiFeMo longitudinally back to the initial state (Figure 7.8a), things become even more troubling. The critical current never seems to increase, even when applying fields more than twice what was used to rotate in the transverse direction.

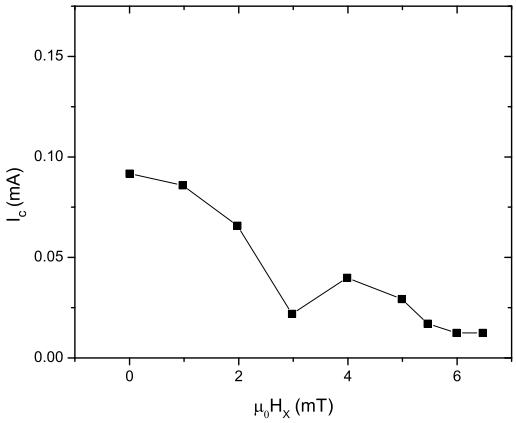

(a) Zero field switching measurement

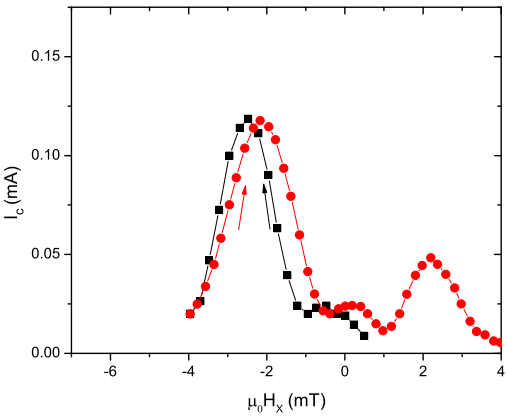

(b) Off-state transverse-field measurement.

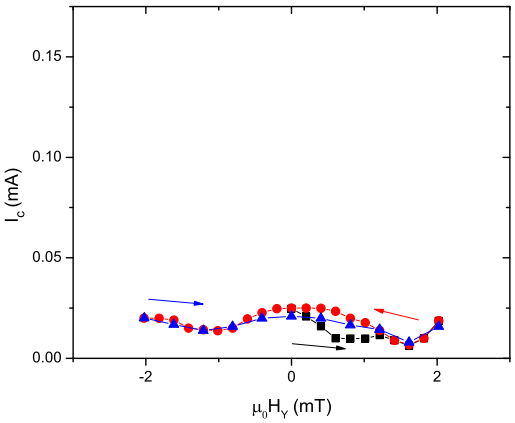

(c) Off-state longitudinal-field measurement. The third (blue) data was measured to ensure the state of the sample hadn't changed during the measurement.

Figure 7.7 *Low-state measurements of Ni/SAF/NiFeMo samples.*

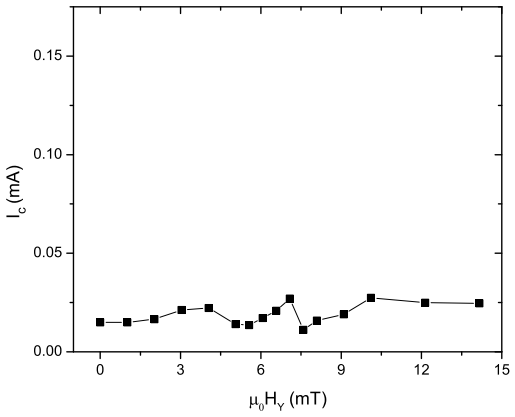

(a) Zero-field switching measurement

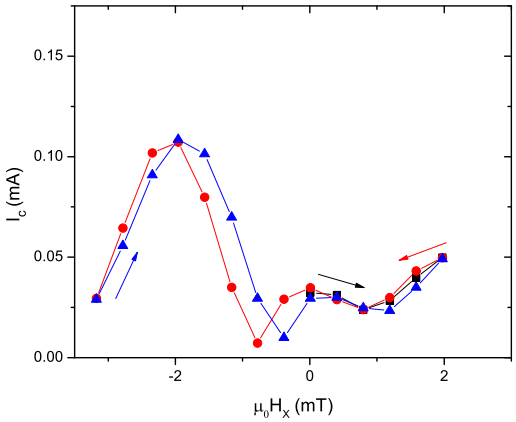

(b) On-state transverse-field measurement. The third (blue) data was measured to ensure the state of the sample hadn't changed during the measurement.

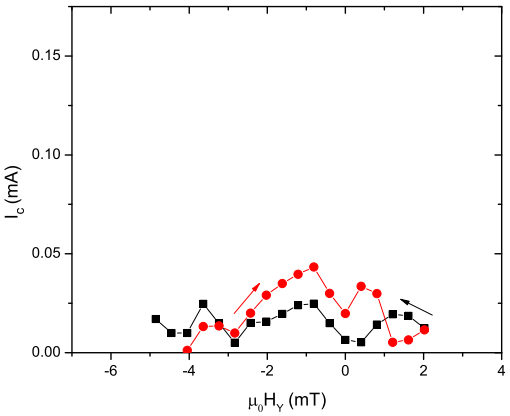

(c) On-state longitudinal-field measurement.

Figure 7.8 *High-state measurements of Ni/SAF/NiFeMo samples.*

Fraunhofer sweeps (Figures 7.8b and 7.8c) once again show a peak in the transverse field but not in the longitudinal field. This peak also moves between the up- and down-sweep directions, despite never experiencing more than a 30 mT external field. This, as well as the zero-field switching data showing movement at low fields (Figure 7.7a), implies the NiFeMo is moving very easily, but the Fraunhofer data taken throughout implies that this switching is neither clean nor consistent.

In the previous section, I mentioned measuring in a small field to make sure we were always at the peak. However, with the apparent ease of moving the magnetization and thus internal flux and peak position, measuring in any sort of field could be enough to change magnetization once again. That is to say, since the peaks in Figure 7.7b are offset about 2-3 mT, it would be ideal to keep this small external field on for all measurements. However, because there is roughly a 20% decrease in critical current within the first 2 mT (see Figure 7.7a), this field could be enough to disrupt magnetization throughout the entire experiment. We also realized that, if rotating longitudinally or transverse, we can only measure the Fraunhofer in that direction, unless the field is kept *very* low. Because of this, future measurements were only to be done in one direction (as described in Section 7.1) to avoid any minor rotation.

When using soft magnetic layers that can move magnetization easily, the only solution to the offset issue would be to extend the width of the Fraunhofer pattern. This would ensure that we are close enough to the peak to measure high on the central lobe, even if not at the maximum, for all measurements in no external field. According to Eqn 2.46, we can see that the values of B that produce minima in the critical current are inversely proportional to the sample radius R, and are given by the zeros of the Bessel function. Therefore, the width of the central peak, in mT, is determined by the diameter of the sample. Solving for our sample

geometry we can calculate that, for pillar diameters of 1 μm, the peak-to-zero Fraunhofer pattern width is roughly 12 mT, and even larger for smaller pillar diameters. This would be a solution to the second issue raised in the previous section, limiting our concerns with moving the Fraunhofer peak. In addition, magnetic layers of this size should be single domain. This should make the switching less ambiguous, resulting in a much cleaner Fraunhofer pattern in general and solving the third issue discussed above.

7.3.3 Small NiFeMo Pillars

With a clear direction, samples with the structure of Nb(100)/Cu(5)/NiFeMo(1)/Cu(10)/ Co(4)/Ru(0.75)/Co(4)/ Cu(10)/NiFeMo(1)/Cu(5)/Nb(20)/Au(15)/Nb(150)/Au(20) were fabricated. The diameter of these pillars were 0.2, 0.3, and 0.5 μm. The milling depth, i.e. how many ferromagnets (0-3, labeled P0-P3) were patterned into single domain circles, was also varied on each chip. While just patterning the Nb above the junction is enough to define the junction size, actually milling through the ferromagnets could ensure an absence of domain walls as well as alter the necessary size of the switching field. While all depths were investigated, issues such as dipolar coupling and softening the SAF became apparent. Therefore, the following discussion (in this and future sections) assumes only the top ferromagnetic layer (P1) was patterned.

In addition to the pillar diameter, there were several other differences between these samples and the previous. All spin mixer layers were now NiFeMo to enhance the effect we were hoping to see. Because changing Ni to NiFeMo reduces the spin-triplet generation and thus the critical current, Co(6)/Ru(0.75)/Co(6) was decreased to Co(4)/Ru(0.75)/Co(4) to compensate. The base Nb dropped from 150 nm to 100 nm due to the Nb roughness relative to its thickness. AFM measurements showed a dramatic decrease in surface roughness, from

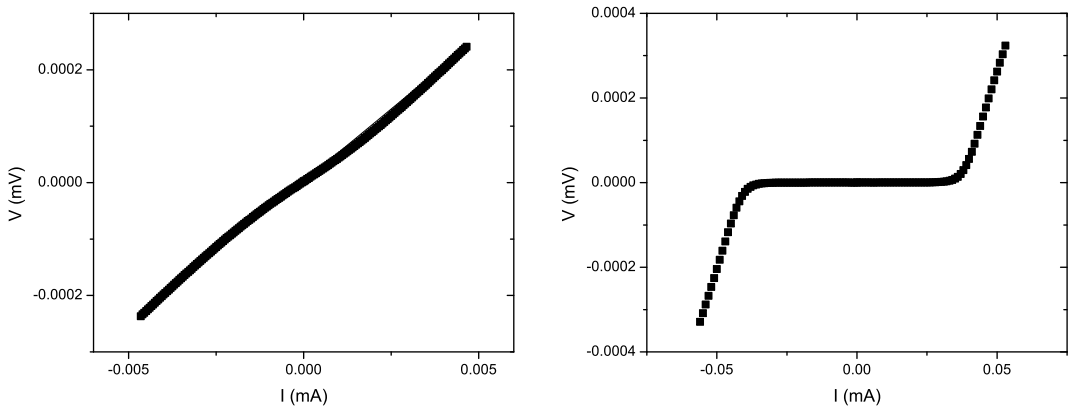

(a) I-V curve for NiFeMo/SAF/NiFeMo samples.

(b) I-V curve for Ni/SAF/NiFe samples.

Figure 7.9 *I-V curves for NiFeMo and NiFe.* The critical current in NiFeMo/SAF/NiFeMo samples is too low to effectively measure. A typical I-V curve for Ni/SAF/NiFe is shown for comparison, demonstrating a much larger critical current.

0.61 nm rms to 0.35 nm rms [65] for 150 nm and 100 nm Nb, respectively. Because all other metal layers are grown on this Nb base layer, it is important to keep the Nb surface smooth. This ensures better ferromagnetic layers. Lastly, the previous run had 10 nm Cu between ferromagnetic layers while the one before had 5 nm. It was at this point decided that all future samples would maintain 10 nm of Cu between ferromagnets in an attempt to decrease coupling effects from nearby magnets. Despite my best efforts and attempts at forethought, the results from these samples were fruitless.

As shown in Figure 7.9a, the maximum critical current obtained in these samples was about 400 nA, much lower than we expected the SQUID measurement system could measure. For comparison, Figure 7.9b displays an I-V curve from a Ni/SAF/NiFe sample, which has a critical current closer to 50 μA. While happy to see that our system was more sensitive than expected, the data collected from these samples were far from concrete and far too close to our noise floor for comfort.

7.4 NiFe Pillars

Although moving in the right direction with respect to magnetic switching properties, a few changes still had to be made regarding our material selection and geometry. At this point, the work described in Chapter 6 was carried out, and NiFe was chosen as a good candidate for the soft ferromagnetic layer as it showed larger triplet supercurrent and better switching behavior than NiFeMo. To enhance the supercurrent even more, the base spin-mixer layer was once again replaced with Ni, meaning we were sacrificing the size of the supercurrent on-off ratio by rotating only one spin-mixer layer relative to the rest in exchange for a larger (and measurable) critical current. The size of the pillars was also increased to 0.5, 0.7, and 1.0 μm diameter, hoping to increase the critical current even more. Still being single domain, these junctions would also have a wide enough central peak to confidently measure close to the maximum, even if moving the Fraunhofer peak remained a concern. These samples were fabricated as follows: Nb(100)/Cu(5)/Ni(1.2)/Cu(10)/Co(4)/Ru(0.75)/Co(4)/Cu(10)/NiFe(1)/Cu(5)/Nb(20)/Au(15)/Nb(150)/Au(20).

7.4.1 First Evidence

To our fortune, be it due to diligence or luck, the first sample we measured with this geometry showed us exactly what we wanted, as shown in Figures 7.10a and 7.10b. The initial Fraunhofer pattern displayed nothing negatively noteworthy. The forward and backward directions did not overlap perfectly, but considering the NiFe is pointing a different way for each sweep, this is not a surprise. Overlap did occur at the extremes, where the two curves have the same magnetization. In addition, the critical current in the wide central peak is greatly above that of the lobes; even though the critical current at zero field is not

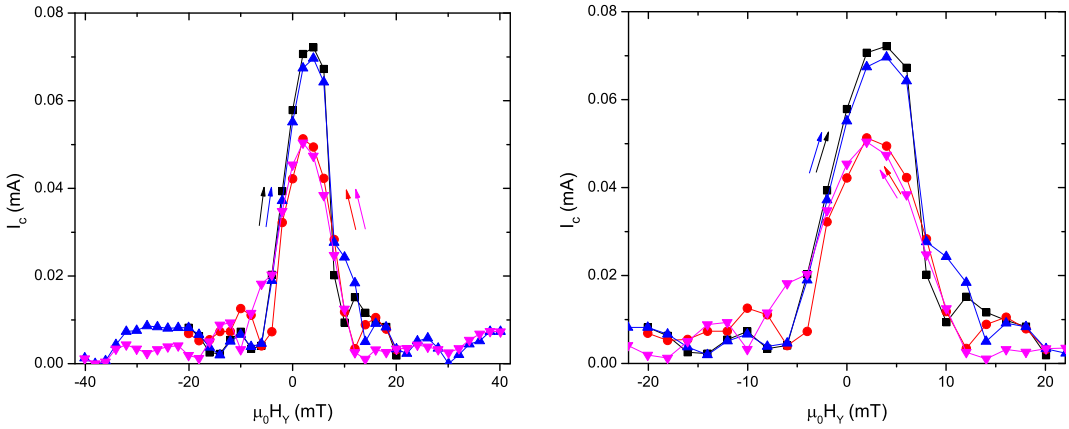

Figure 7.10 *Initial measurements for Ni/SAF/NiFe – Sample 1.* Data in (a) and (b) are the same, plotted with different field ranges. Measurements to ±20 mT agree well with those taken to ±40 mT.

the maximum, it is large enough to distinguish whether the spin-triplet supercurrent is on or off.

It should be noted that the data shown in Figures 7.10a and 7.10b are the same, but plotted with different field ranges. By measuring out to ±40 mT, we observe more lobes of the Fraunhofer pattern. However, to avoid unnecessary rotation of magnetization within ferromagnetic layers, we keep the external field as low as possible. From the comparison of the data we show that it is not necessary to use fields larger than 20mT, despite the data not demonstrating as clear of a Fraunhofer pattern.

The next step, as discussed in Section 7.1, is to measure the size of the critical current at zero field as we rotate the NiFe magnetization. Even if we were moving the Fraunhofer peak, as was a concern before, its width ensures we are obtaining a direct measurement of critical current, and thus the magnitude of spin-triplet supercurrent, near the maximum. As we increase the field in the transverse (off) direction (Figure 7.11a), the critical current goes down, and comes back up as the field increases in the longitudinal (on) direction (Figure 7.11b). According to Figures 7.11a and 7.11b, the NiFe rotates within 20 mT. This corre-

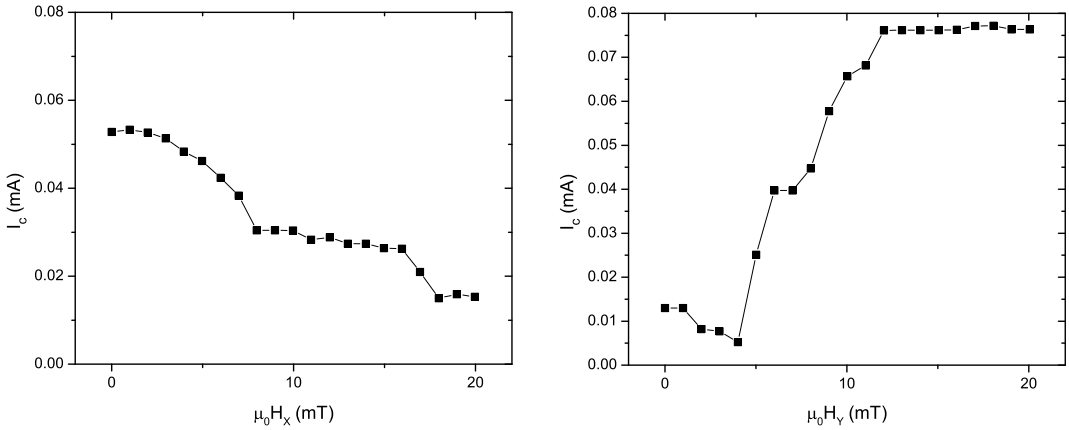

Figure 7.11 *Sample 1 switching data.* The triplet critical current turns off as the magnetization of NiFe is rotated by the transverse magnetic field (a). The triplet critical current is turned back on with the application of a longitudinal field (b).

sponds with the data from Section 6.1.2, also showing 180-degree switching within 20 mT. Lastly, AMR data (see Section 6.2.3) shows that Co/Ru/Co SAFs with 4 nm Co thickness shouldn't rotate much (<10%) within the first 20 mT, either.

Although the changes in the critical current for each successive field are not constant, and the critical current even plateaus for certain field ranges, given their small size it is possible that the pillars aren't perfectly round or have some other defects. As such, the magnetization may find energetically favorable minima while rotating, but eventually it does continue until fully rotated.

The field required to rotate the magnetization back to its original (on) state is less than that required to rotate it to its off state. This behavior is consistent with the magnetocrystalline anisotropy induced by the growth field (see Section 2.1.1). Because the samples are grown in a magnetic field (see Section 4.2.2), the internal magnetization favors the on direction, making it easier to rotate toward this field direction. In addition to the magnetocrystalline anisotropy, while the ferromagnetic layers are mostly decoupled by the Cu spacers between them, stray field effects due to dipolar coupling between layers could still

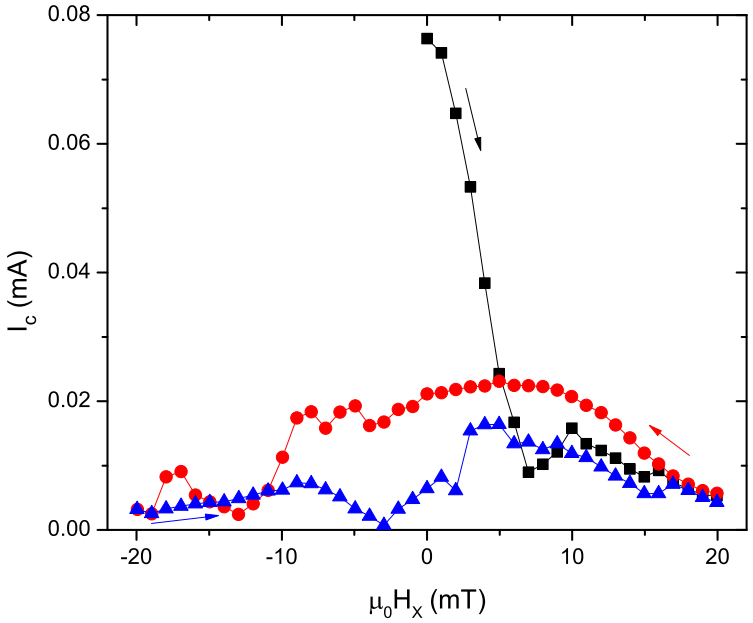

(a) On- to off-state Fraunhofer pattern sweeps.

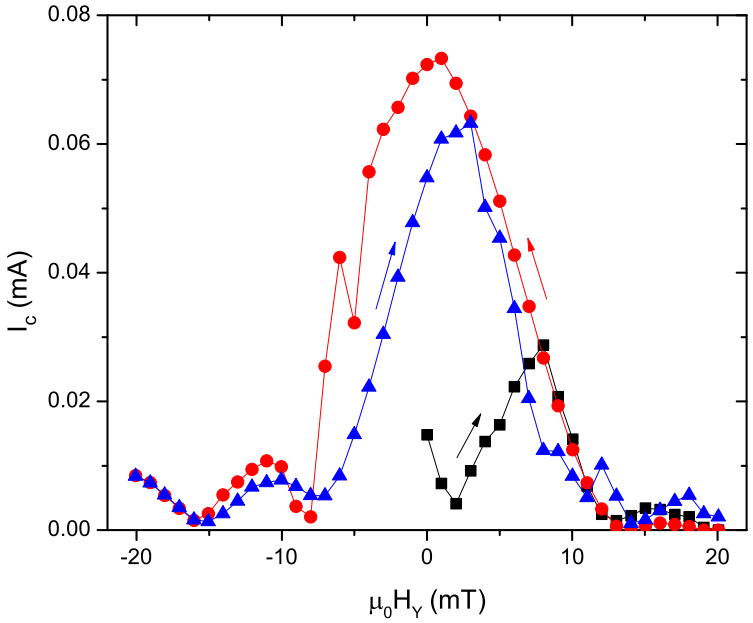

(b) Off- to on-state Fraunhofer pattern sweeps.

Figure 7.12 *Fraunhofer patterns measuring the switch in Sample 1.* The black curves measure the NiFe magnetization as it is rotated into the off state for (a) and into the on state for (b). Red and blue curves in each are subsequent measurements, demonstrating that the sample remains in that state.

have an effect.

The next step is to measure in field and obtain the Fraunhofer pattern as the magne-

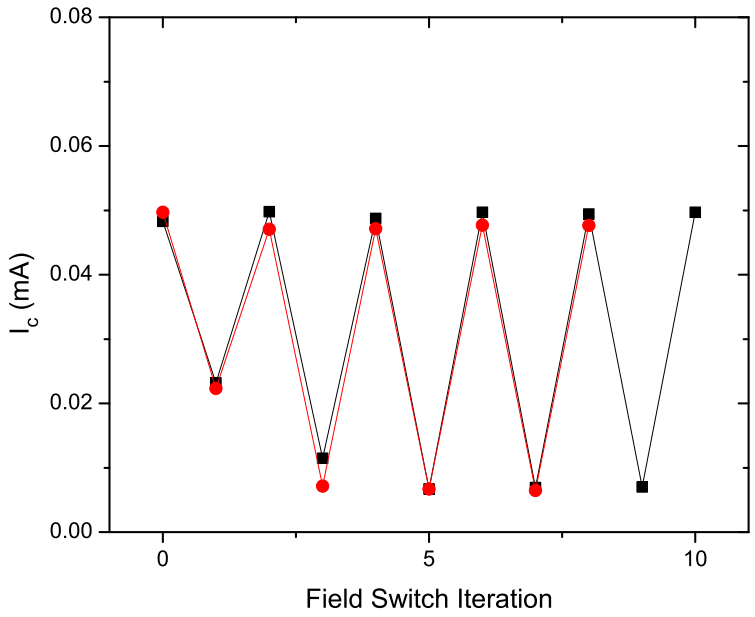

Figure 7.13 *On-off switching for Ni/SAF/NiFe – Sample 1.* Red and black curves measure the field in different directions (positive and negative). On/Off ratio ≈ 7.

tization rotates, measuring in field for the pattern in its off state as well. As Figure 7.12a shows, once the sample is in its off state, it stays there for the entirety of the measurement, not returning until being rotated again. This is also true for turning the triplet supercurrent back on (Figure 7.12b), maintaining the high-triplet state, as seen in the figure.

The last step is to demonstrate the ability to turn the sample from on to off and back again by simply applying the necessary field to rotate. Applying a 20 mT field in the on (off) direction, measuring the critical current should show us a high (low) value. This is demonstrated in Figure 7.13. There seems to be a bit of a training period in the first couple of switches, which is not fully understood.

The ratio of critical current size between on and off is about 7 for this first sample. That ratio, along with the shape of the Fraunhofer patterns for on and off measurements, is sufficient to claim that the ability to control triplet supercurrent in these samples has been realized. For completeness, the initial Fraunhofer patterns (longitudinal) and the final

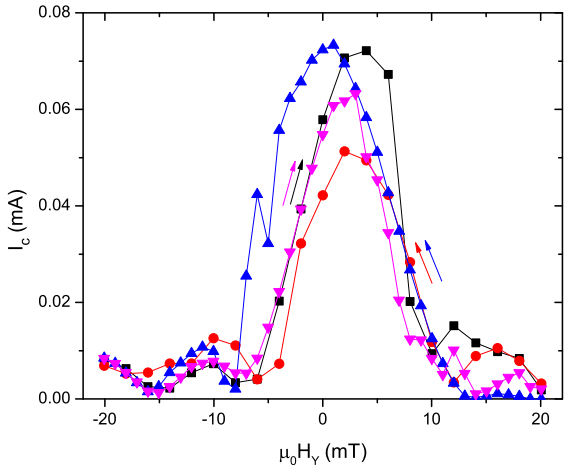

Figure 7.14 *Initial and final Fraunhofer measurements for Ni/SAF/NiFe – Sample 1.* Black and Red curves demonstrate the initial sweeps while blue and pink demonstrate the final sweeps, taken after being switched between states numerous times.

ones are plotted on each other in Figure 7.14. Although the size of the critical current is not exactly the same for each point, the general trend is the same. Most deviations occur after the switching begins, which is a largely uncontrollable regime (until the switching is completed). Therefore, differences at this point are not too alarming.

7.4.2 A Fabrication Hiccup

However, one sample does not a true experiment make. More samples were then fabricated and measured with the same geometry. During this sputtering run, the Co target came loose from its housing, potentially contaminating the Co layers with some indium, making the SAF softer. These samples all had either poor initial Fraunhofer measurements, implying some magnetization layer hadn't set properly, or showed evidence of SAF rotation much earlier than expected. This caused us to look closer at the SAF data, deciding it would be prudent to try to keep the field as low as possible as opposed to using 20 mT fields for every sample. Even 20 mT is enough to potentially rotate the SAF a little, so we want to limit our fields to only what is necessary to rotate the NiFe.

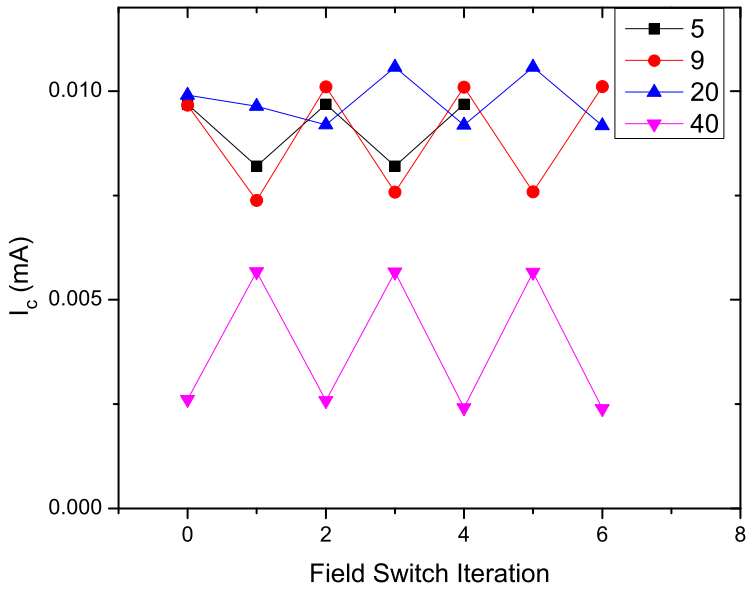

Figure 7.15 *Field dependence of on-off switching.* On-off switching data was taken for multiple field sizes, as listed (in mT). The even iterations are always in the longitudinal, or on, direction. At 20 mT (blue), the longitudinal direction becomes the off direction, likely due to SAF rotation in the pillar.

However, despite being a bit disappointing, these samples were still measured to see the effects of SAF rotation on our measurements. The most useful data taken from this experiment was looking at the on-off switching for different fields. Figure 7.15 shows this switching for four different fields. The initial measurement (5 mT) shows a small effect, which gets larger with increased field (9 mT). However, starting at 20 mT, further increases starts to rotate more than NiFeMo, with a switch between what becomes the on and off states. (For all on-off switching data, even iterations should be the on state while odd are off.) This flip between what is high and low remains that way for all subsequent fields (up to 45 mT).

We can conclude from this result that the SAF is rotating in these fields more than we anticipated. Whether this is due to softening of the SAF from indium contamination or some other source, it really drives home the need to keep our fields small enough to prevent

as much SAF rotation as possible.

7.4.3 Reproducibility

After cleaning the Co and its housing to prevent further contamination and securing it in place to ensure it didn't happen again, new samples were fabricated with the same structure as before. They were once again measured as explained in Section 7.1, and their data is plotted in Figures 7.16-7.25. In an effort to minimize Co/Ru/Co magnetization rotation, the size of the field was kept as small as possible, which can be seen in Figures 7.17 and 7.21. This, as well as some potential concerns with keeping the field too small, will be detailed below.

The Fraunhofer patterns that were measured while the magnetization was rotating (Figures 7.18 and 7.23) demonstrate the same characteristics we observed in Sample 1. The samples demonstrate a switch from "on" to "off" (a) and vice versa (b) between subsequent Fraunhofer pattern measurements. In addition to these, an extra measurement was taken with Sample 3. After the magnetization was rotated into the on or off state, a very narrow Fraunhofer pattern in each direction (x and y) was measured near zero field (Figure 7.22). This was done to show that the state is stable, even in the presence of a small field, which is demonstrated by the reversibility of all measurements. On-off measurements of these two samples (Figures 7.19b and 7.25), demonstrating ratios of 19 for Sample 2 and 5 for Sample 3.

As mentioned above, the size of the external field used while measuring Samples 2 and 3 was limited as much as possible to prevent Co/Ru/Co rotation. To determine this limit, the measurements in zero field were done as normal, stepping the transverse field up to 20 mT, although the minimum may occur before 20 mT. The field at which the minimum is found is

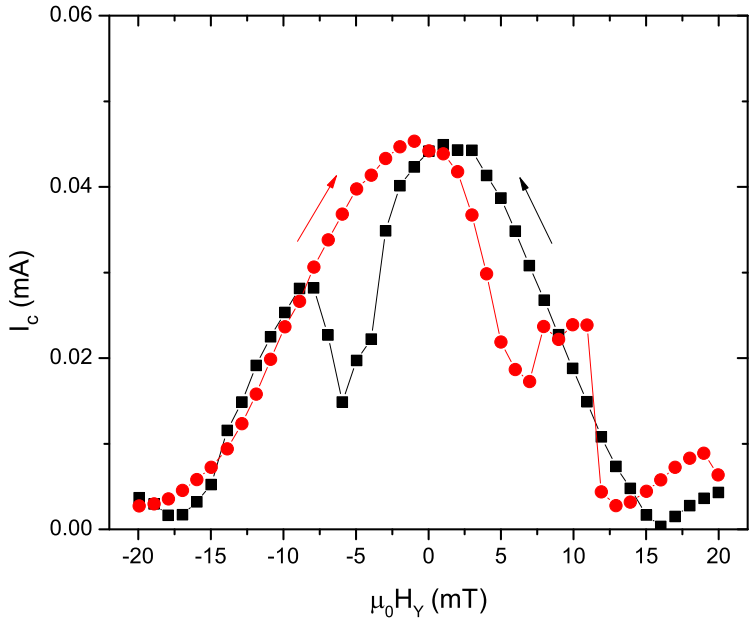

Figure 7.16 *Initial Fraunhofer measurements of Ni/SAF/NiFe – Sample 2.*

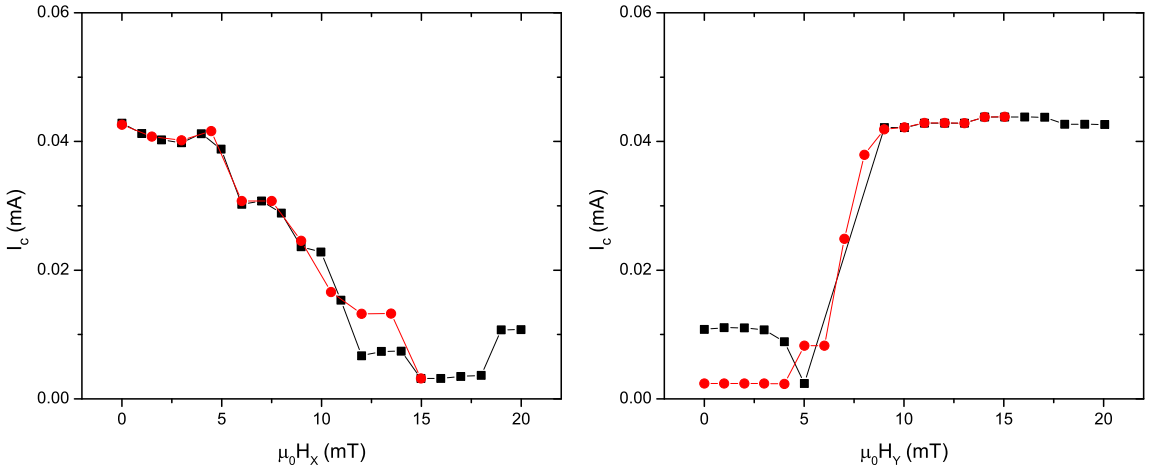

(a) Zero-field switch to off state – Sample 2.

(b) Zero-field switch to on state – Sample 2.

Figure 7.17 *Ni/SAF/NiFe switch field measurement – Sample 2.* Switching in zero field in (a) and (b), measuring the required field to rotate the magnetization to the off and on switch, respectively. Black curves in (a) and (b) measure rotation to 20 mT, which includes rotation of the SAF at 19 mT in (a). The red curves keep the field low enough to avoid as much SAF rotation as possible.

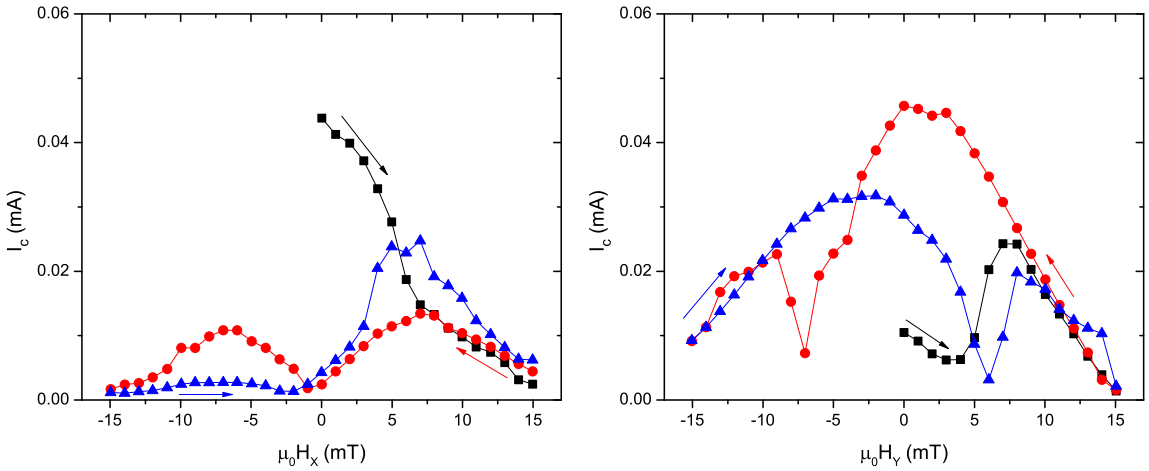

(a) On- to off-state Fraunhofer pattern sweeps. (b) Off- to on-state Fraunhofer pattern sweeps.

Figure 7.18 *Fraunhofer patterns measuring the switch – Sample 2.* The black curves measure the switch from on to off state (a) and vice versa (b). The red and blue curves in each are subsequent measurements, demonstrating that the sample remains in that state.

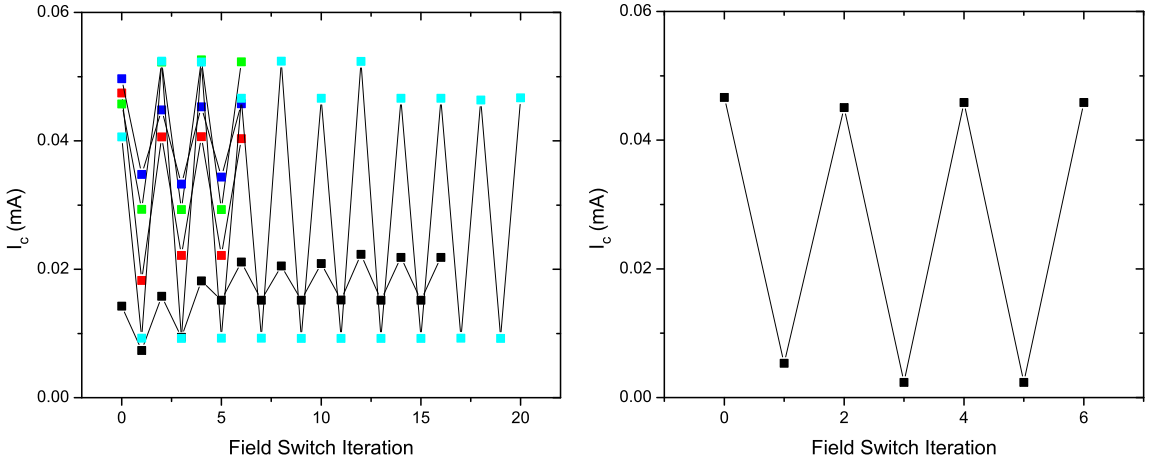

(a) On-off switching at 15 mT. (b) On-off switching at 16 mT.

Figure 7.19 *On-off switching for Ni/SAF/NiFe – Sample 2.* Even iterations have the field applied in the longitudinal direction, odd iterations have field applied transversely. Curves in (a) are all taken at 15 mT, but for fields applied in different directions (positive and negative). The lack of reproducibility is eliminated when the field is increased slightly to 16 mT (b). On/Off ratio for this sample is ≈ 19.

the field that is used for all subsequent switching in the sample. An example of this step can be seen in Figure 7.17a. The first run measures in zero field up to a 20 mT externally applied transverse field (black). Above 18 mT, though, the critical current increases, implying some rotation of the SAF. A second measurement was undertaken to demonstrate monotonic decrease of critical current to 15 mT (red) in the transverse direction. Measurements in the longitudinal direction show that the sample returns to the on state within that range as well (Figure 7.17b). Therefore, the field utilized to rotate the sample is set to 15 mT.

While we want to keep the field as low as possible, limiting the field to exactly the minimum value has its detriments as well. This field may be enough to rotate the NiFe 90 degrees, but might not be enough to fully flip it 180 degrees. Sample 3 demonstrated this effect, plotted in Figures 7.23b and 7.24. Looking at the data in Figure 7.21b, sweeping to 10 mT should be enough to reset the sample into the on state. Therefore, after sweeping from 0-10 mT (black curve, Figure 7.23b), the sample should be in the on state. This is confirmed in the subsequent sweep from 10 to -10 mT (red curve). However, when sweeping back from -10 mT (blue curve), we observe what looks like off-state behavior. I believe this is due to the NiFe not fully rotating 180° at -10 mT; when sweeping back, adjacent magnetization directions are not orthogonal, and thus not a maximum. However, resetting this measurement to -20 mT, the field to which it was initially measured, we see the sample is back in the on state as expected.

This is also plotted in Figure 7.24. The four curves plotted are as follows: black – initial measurement from 20 to -20 mT; red – initial measurement from -20 to 20 mT, taken after 180° due to black; blue – comparison to initial on-state measurement (black) from 10 to -10 mT, taken after 90° rotation; pink – comparison to initial on-state measurement (red) from -20 to 20 mT, taken after 180° due to blue. Even though the blue curve was taken after

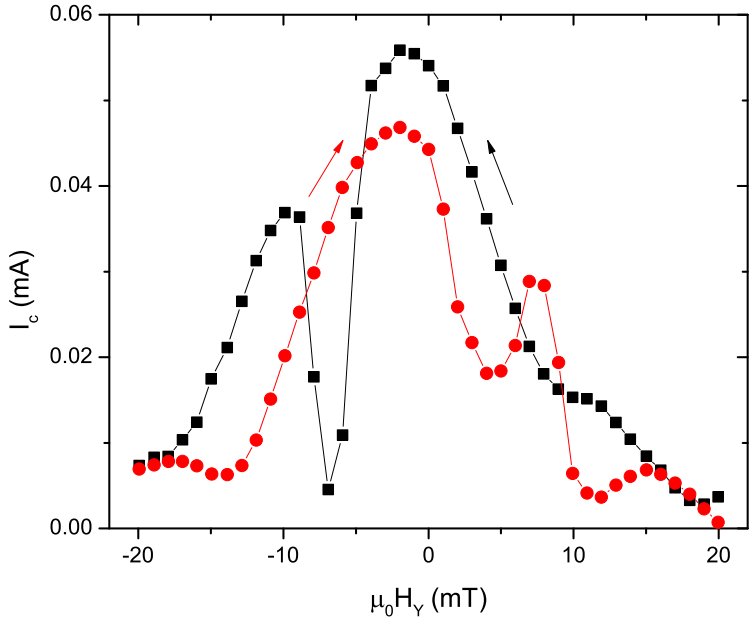

Figure 7.20 *Initial Fraunhofer measurements of Ni/SAF/NiFe – Sample 3.*

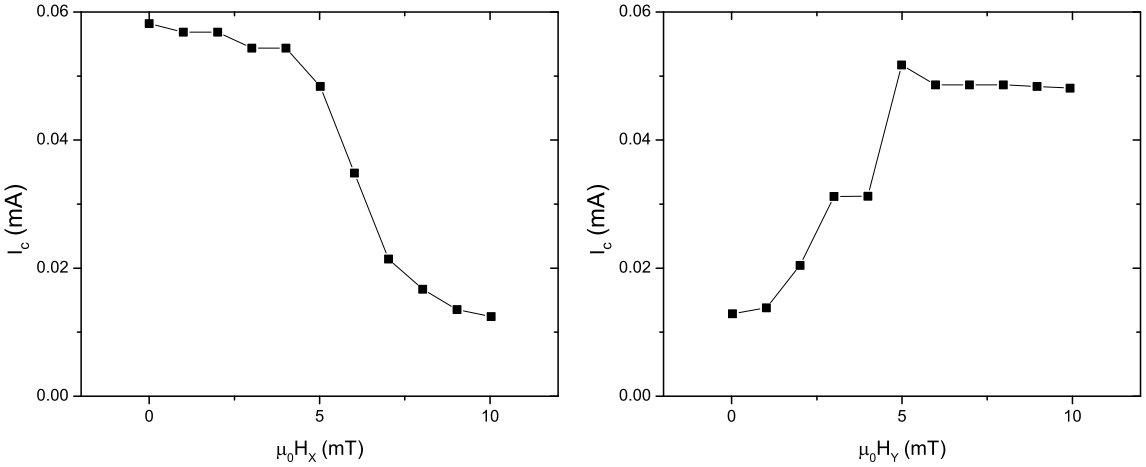

(a) Zero-field switch to off state – Sample 3.

(b) Zero-field switch to on state – Sample 3.

Figure 7.21 *Ni/SAF/NiFe switch field measurement – Sample 3.*

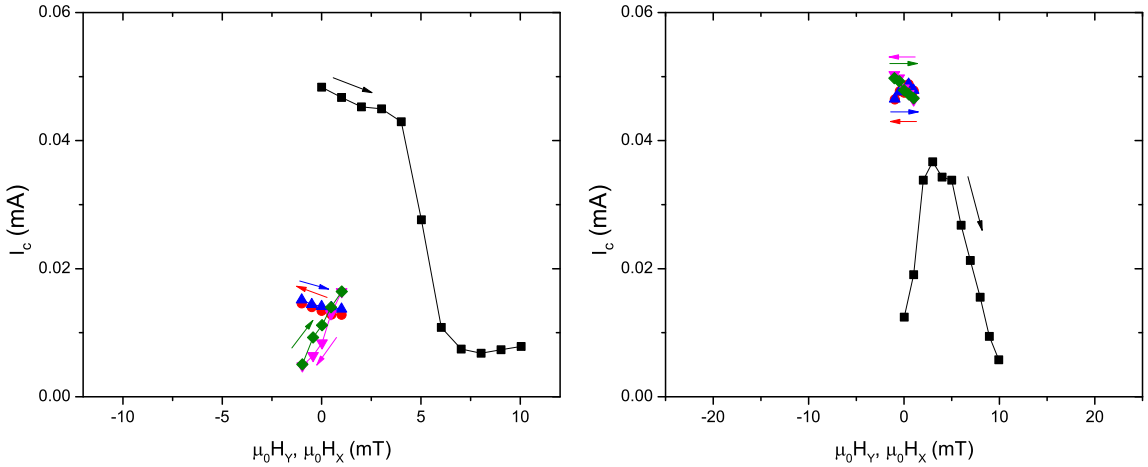

(a) Off-state near-zero-field Fraunhofer pattern sweeps.

(b) On-state near-zero-field Fraunhofer pattern sweeps.

Figure 7.22 *Near-zero-field Fraunhofer patterns measuring the state – Sample 3.* The black curves in each figure either turns the triplet supercurrent off (a) or on (a). The critical current is then measured in all directions, x- and y-, to small field to show stability of the magnetizations. This ensures the sample really is in this state and stable in small fields.

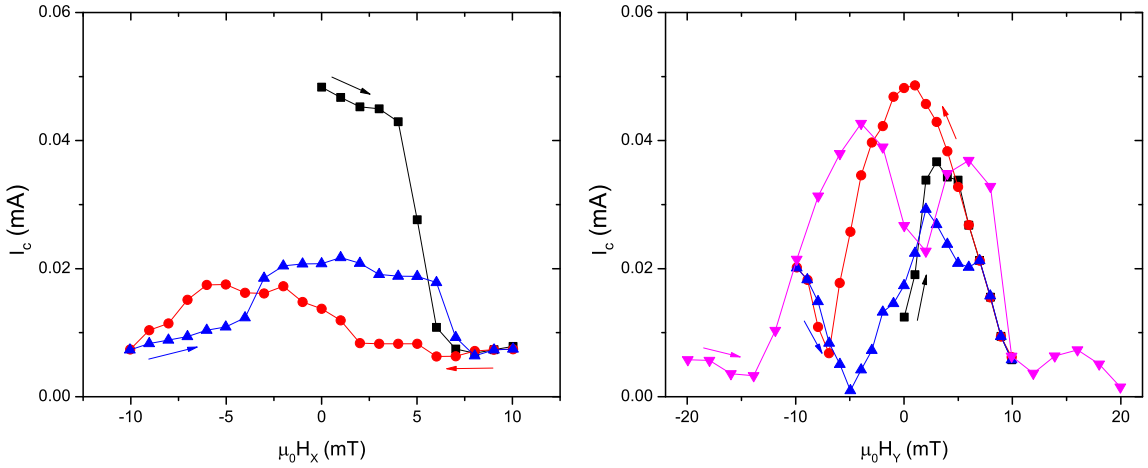

(a) On- to off-state Fraunhofer pattern sweeps.

(b) Off- to on-state Fraunhofer pattern sweeps.

Figure 7.23 *Fraunhofer patterns measuring the switch – Sample 3.* The black curves measure the switch from on to off state (a) and vice versa (b). The red and blue curves in (a) are subsequent measurements, demonstrating that the sample remains in the off state. The red curve in (b) remains in the on state, but doesn't flip the magnetization fully. Therefore, the blue curve isn't in the on state. This is reset when a larger field is applied (pink curve).

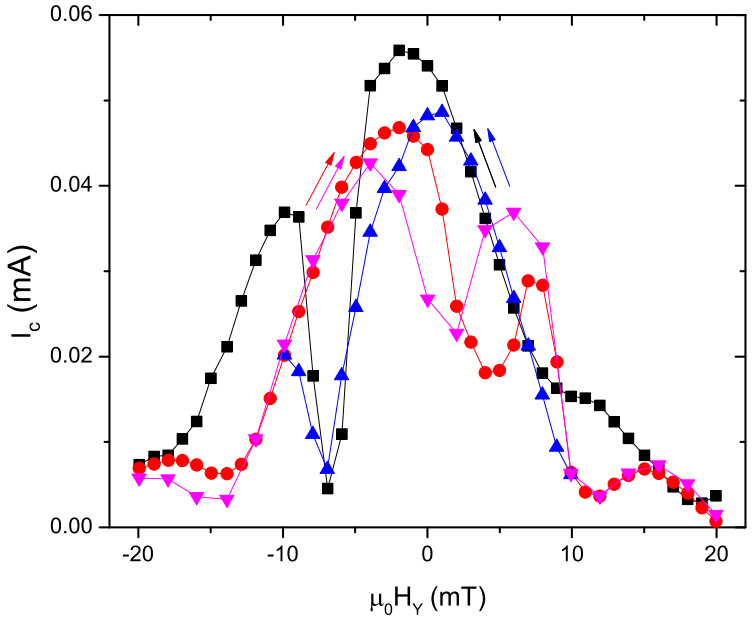

Figure 7.24 *Initial and final Fraunhofer measurements – Sample 3.* The overlaps between black and blue as well as between pink and red demonstrate the sample has returned to its initial state after numerous switches.

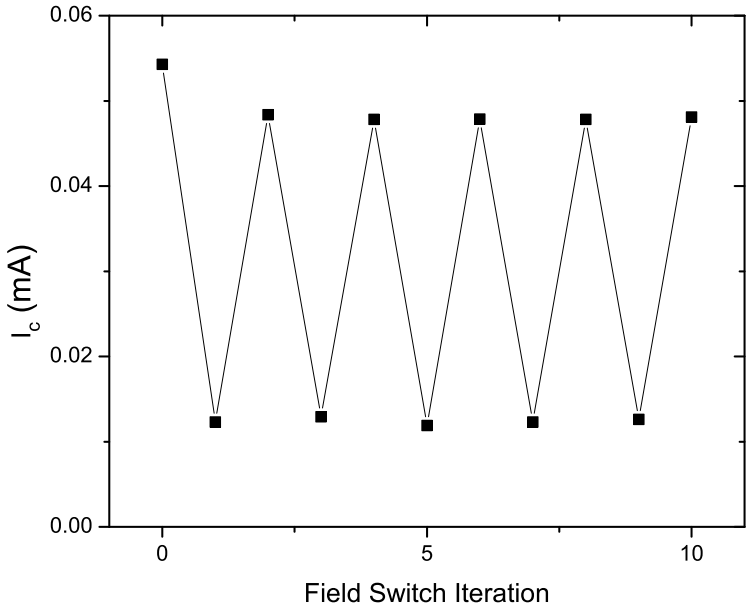

Figure 7.25 *On-off switching for Ni/SAF/NiFe – Sample 3.* On/Off ratio ≈ 5.

rotation from off to on state in only 10 mT, we see that the black and blue curves compare nicely. This tells us that 10 mT is enough to rotate the sample back to its on state. However, the pink curve requires a larger field (-20 mT) to compare well with the initial red curve. This implies that 180° flipping requires more field than that of 90°.

Keeping the field too low can also effect the on-off switching measurements. All data taken prior to this final switching measurement were acquired using a slowly increasing field, which will incrementally rotate the NiFe magnetization. However, the on-off measurement is done by applying the full necessary field in alternating directions, transverse and longitudinally. It is possible that, to rotate 90 degrees in one step, a larger field is required than what is necessary to slowly rotate 90 degrees. Using Sample 2 as an example of this effect, on-off switching at 15 mT was inconsistent and small (Figure 7.19a). However, by increasing the switching field only slightly to 16 mT, the switching was pronounced and reproducible (Figure 7.19b).

Overall, Samples 2 and 3 behaved in the same way as Sample 1, showing the same switching characteristics and behavior, with on-off ratios of about 19 and 5, respectively. Potential causes for the differences in ratios, as well as a more thorough analysis of the size of the ratio, will be discussed in the next section. However, it is important to note that the magnitude of the on-state critical current, and more importantly $I_c R_N$, is consistent across all three samples. This implies that the variability between samples is more likely caused by magnetic properties than fabrication issues or sample inconsistencies. Additionally, when measuring currents as small as we obtained when in the low state, slight variations of this current can have large impacts on the ratio. The important result is that the sample has changed from a high- to a low-triplet supercurrent state, or from a spin-triplet to a spin-singlet state, and is stable without the presence of a magnetic field. The effect is reproducible

between samples, and within a sample the size of the effect is also reproducible.

7.4.4 Quantitative Analysis of On-Off Ratios

It is hard to ignore that the ratios for this effect have fairly large sample-to-sample variation. While it is true that the size of the effect should be the same, it is not useful to put too fine a point on it. There are many differences between each run that can account for discrepancies: the initial magnetization state of the Ni can vary, and flux removal is not a precise practice; small differences in roughness or growth conditions could effect the hardness of the NiFe, etc. More importantly is that the relative magnetization directions play a very crucial role in the amplitude of supercurrent.

Due to minor differences between samples, it is impossible to determine exactly how much we are rotating the NiFe and not the Ni or the Co/Ru/Co. When fully in the on state, all adjacent magnetization layers are assumed to be orthogonal ($\varphi = \theta = 90^\circ$). Recalling Eqn 2.50, which states $I_c \propto \sin\theta \sin\varphi$, we can see that small deviations from this angle marginally affect the critical current amplitude. In contrast, when fully in the off state, one angle is orthogonal ($\varphi = 90^\circ$) while the other is collinear ($\theta = 0^\circ$). This state is never completely achieved due to small rotations in the SAF (see Section 6.2), and small deviations in θ ($\delta\theta$) will have a larger effect on the critical current amplitude than deviations in φ ($\delta\varphi$), i.e. $|\sin(\delta\theta) - \sin(\theta)| > |\sin(\delta\varphi) - \sin(\varphi)|$ for the same size deviation.

It is therefore difficult to analyze the theoretical on-off ratio we expect in these samples. However, using the data from AMR measurements of the Co/Ru/Co SAF, we can determine a rough estimate of spin-triplet generation in the on and off states from Eqn 2.50. In this analysis, in the off state, we will assume that the magnetization of the NiFe has rotated 90° relative to that of the Ni layer. Obtaining resistances from the data (lower curve in Fig 6.9c)

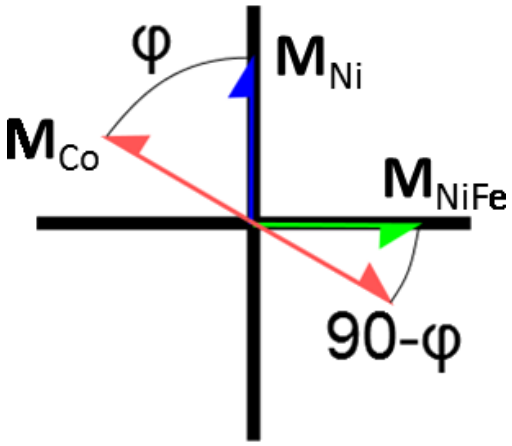

Figure 7.26 *Cartoon of magnetization direction and relative angles for the off state used in on-off ratio analysis.*

and solving for φ in Eqn 6.1, we can determine the rotation of the magnetization of the SAF relative to that of Ni as

$$\varphi = \arccos\left(\sqrt{\frac{R_\varphi - R_\perp}{R_\parallel - R_\perp}}\right) \tag{7.1}$$

where $R_\parallel$ and $R_\perp$ are given in Table 7.1. The relative-magnetization angle between NiFe and the SAF is $\theta = 90° - \varphi$. These directions of magnetization for each layer and relative angles thereof between adjacent layers are demonstrated in Fig 7.26. In the on state, we will assume $\theta, \varphi = 90°$.

$R_\parallel$	52.9044 Ω
$R_\perp$	52.7624 Ω

Table 7.1 *Table of $R_\parallel$ and $R_\perp$ for Co(4) SAF.*

The on-off ratio can be written as

$$\frac{I_{c-on}}{I_{c-off}} = \frac{1}{\sin\theta_{off}\sin\varphi_{off}}. \tag{7.2}$$

Eqn 7.2 yields ratios of 3.1, 3.6, and 5.0, respectively. This data is summarized in Table 7.2.

In each sample, we measured ratios as large or larger than those determined by this analysis, implying we have rotated the SAF less in these samples than a worst-case analysis yields.

Sample	Switch Field (mT)	R(φ) (Ω)	φ ($^\circ$)	Expected Ratio	Measured Ratio
1	20	52.7797	69.58	3.1	7
2	16	52.7745	73.01	3.6	19
3	10	52.7684	78.12	5.0	5

Table 7.2 *Table of quantitative on-off ratio analysis.*

Chapter 8

Conclusions

8.1 Overview

The early theories predicting long-range spin-triplet pair correlations in superconductor/ ferromagnet/superconductor (S/F/S) Josephson junctions spurred experimentalists to realize this phenomenon. Early results proved promising, and the development of three-ferromagnetic-layer structures, written herein as S/F_1/F_2/F_3/S or S/F'/F/F"/S, granted researchers a method to make reproducible samples with which exploration of this field was possible. Once the ability to create samples that demonstrated long-range spin-triplet supercurrent (as well as those that did not) became clear, a desire to turn this triplet supercurrent "on" and "off," or measure a large or small critical current, respectively, in the same sample developed within the community. That was the focus of this work – to create ferromagnetic Josephson junctions in which the spin-triplet critical current amplitude could be adjusted. Relying on the relative magnetizations between neighboring layers, we were able to demonstrate reproducible switching by rotating the NiFe spin-mixer layer into and out of collinearity with the Co/Ru/Co synthetic antiferromagnet (SAF).

8.2 Summary of Results

At the onset of this project, a sample that could demonstrate this switching, and stably maintain the state in zero field, had yet to be realized. To observe this effect, we relied on controlling magnetization directions of independent ferromagnetic layers within S/F'/F/F"/S Josephson junctions. Although some of the samples measured had been made previously, none of them had undergone switching measurements. In addition to investigating the effect with previously made samples, a lot of optimization and characterization needed to be done before successful samples could be fabricated and measured. This process and the results obtained are summarized below.

The first samples measured had Ni as the F' and F" layers and Co/Ru/Co SAF as the F layer. Knowing Ni to be a hard ferromagnet, we hoped to rotate the SAF in order to control the collinearity of the ferromagnetic layers. However, to achieve this rotation, measurements required very large fields. This resulted in movement of Ni domains as well, providing irreproducible data. From these results, it was determined that a softer ferromagnet was needed for the rotating layer.

NiFeMo, a softer ferromagnet than Ni, was chosen to replace Ni as one spin-mixing layer (F"). Ni remained as the other spin mixing layer (F') while maintaining Co/Ru/Co as the F layer, both of which were hard ferromagnetic layers. Although the NiFeMo layer rotated at lower fields than in previous samples, the sample dimensions prevented us from successfully measuring on-off switching. Ideally the central lobe of the Fraunhofer pattern, a measure of the critical current relative to the flux in the junction, would be wide enough such that the critical current is still large at zero field. However, the width of the central lobe in a 3 μm-diameter sample was too narrow relative to the offset of the central peak, preventing

a large critical current to be measured at zero field. To obtain a wider central lobe, the Josephson junction diameter needed to be decreased, which conveniently also allowed for the magnetic layers in the Josephson junction to be single domain. All future samples were made with small sample diameters, $\leq 1\mu m$.

While fabricating smaller samples, we also replaced the F' layer with NiFeMo. This was done with the intent of rotating both spin mixer layers, increasing the size of the effect, as described in Eqn 2.50. Unfortunately, the critical current was too small to be measured. Additionally, between this set of samples and the previous, the expected switching behavior of NiFeMo seemed to change – a worrying result when trying to eliminate sample-to-sample variability. At this point, being comfortable with the initial investigation, we decided to narrow our scope to a few materials: NiFe, Co/Ru/Co, and Ni. Layer characterization was necessary to determine the optimal thicknesses of each layer before full samples were created.

Triplet generation measurements with NiFe demonstrated that it would be as suitable a spin-mixer layer as NiFeMo, with comparable or higher $I_C R_N$ values and a low switching field ($|\mu_0 \mathrm{H}_{switch}| \approx 10\mathrm{mT}$). Also, anisotropic magnetoresistance (AMR) data from Co/Ru/Co samples with various Co thicknesses assured us that thinner Co layer would grant a hard synthetic antiferromagnet. Although thinner samples proved harder, there is also less short-range supercurrent decay in samples with thin F layers compared to those with thick F layers. To find a balance between these opposing effects, Co(4), where the parenthetical number is the layer thickness in nm, was chosen for each layer in the SAF.

Samples were then made and measured with one NiFe spin-mixer (F") as a rotating soft layer. Ni was the other spin-mixer (F'), as it generates more spin-triplet components than NiFe, and Co/Ru/Co was the central SAF. Using the smaller geometry (sample diameter=$1\mu m$) and this composition (F': Ni; F: Co/Ru/Co; F": NiFe), these samples

demonstrated the ability to control long-range spin-triplet amplitude and maintain the state in zero field. Multiple samples across various sputtering runs demonstrated the switching we sought, with on-off ratios as large as $I_{c-on}/I_{c-off} \approx 19$.

8.3 Future Work

Despite feeling comfortable with the results presented here, samples in this geometry undoubtedly have a "Goldilocks Zone" of sorts. The magnetic field must be high enough to rotate the NiFe while staying low enough not to rotate the SAF. However, we feel that the effective magnetic-field range is small for these samples.

As stated previously, SAF characterization results imply that thinner Co requires more field to rotate, generating a harder synthetic antiferromagnetic layer. However, the thinner the central ferromagnet, the less suppression of spin-singlet supercurrent is present. We are in the process of making and measuring samples with Co(3); perhaps the slightly harder SAF will give a larger region of acceptable magnetic fields that minimally rotate the magnetization, thus widening the Goldilocks Zone.

In addition, it would be ideal if the NiFe were softer than it is in these samples. Given that NiFe is the last magnetic layer grown in the structure, surface roughness from the underlying layers could become a very large factor as to how it behaves. Although the difference is not large, roughness measurements have shown that growing a $[\mathrm{Nb/Al}]_n$ multi-layer for the bottom electrode, as opposed to the Nb(100) currently in the system, provides a smoother surface for the rest of the stack. This would, however, require breaking vacuum during the run, as there are only seven sputtering guns in the sputtering chamber, and eight materials are needed for this type of multi-layer growth. Before opening the system to switch guns,

it would therefore be necessary to deposit an Au capping layer to protect the multilayer. Despite the added steps, the smoother growth could promote better characteristics of the ferromagnetic layers, perhaps even enough to lower the switching field of the NiFe slightly. As another option, in order to maintain an *in situ* fabrication of all layers, $[Nb/Au]_n$ multilayer samples are also being considered. While demonstrating smoother growth compared to Nb(100), samples with multilayers of $[Nb/Au]_n$ are not as smooth as those with $[Nb/Al]_n$. However, as their growth does not require breaking vacuum, they still may yield smoother sample layers. Samples of both types of multilayers are currently being made as of the time of writing this thesis.

Another option for future work is to remove the Ni F' layer and replace it with NiFe. As mentioned previously, rotating both spin-mixer layers would theoretically enhance the on-off ratio. At one point during the experiment, this hope was abandoned, but with the procedure and fabrication thoroughly optimized, this may still be worth pursuing. In addition, NiFe has slightly more triplet generation capabilities than NiFeMo, and with a thinner SAF, the critical current may become large enough to measure.

One aspect I find particularly interesting is the potential use of this switching in practical applications. Having an "on" and "off" triplet state can be interpreted as a "0" or "1" state as a binary memory. However, Josephson junctions with this geometry, i.e. a circle, don't have bi-modal stability; there is no preferential direction in the plane of the ferromagnet, so the initial state could point any direction. If we could engineer a system that had a preferred initial direction, this type of application could become realized.

APPENDIX

Range of Spin-Triplet Pair Correlations in S/F/F Systems

Quite a bit of my time as a graduate student had been spent trying to determine the length-scale of the long range spin-triplet pair correlations in S/F/S Josephson junctions. To my dismay, all results from this work have been far from conclusive. This appendix will describe that work, the troubles encountered along the way, and where the project is now. Hopefully this document will help any future student who may start a similar undertaking.

There are two main aspects of this project: measurements of supercurrent in lateral geometry Josephson junctions and measurements of long range proximity effect in ferromagnetic wires. The initial intent was to measure the Josephson junction critical current as a function of junction length, effectively mapping out the spin-triplet decay length. The proximity effect measurements were carried out by measuring the change in resistance as a function of temperature and wire length. From such data, the coherence length of spin-triplet pair correlations in Co should be determinable. While the proximity effect project only emerged from the frustrating results of the Josephson junctions, these two projects will be discussed simultaneously throughout this appendix. In lieu of a chronological story, I hope this organization allows for better comprehension of the work and results described.

Motivation

It is common for those investigating S/F systems to claim that a pair of electrons in a spin-singlet state with $m_s = \pm 1$ experience a ferromagnetic material as a normal metal because both electrons are in the same (majority or minority) spin band (see Sections 2.3.2 and 2.5), a claim I have even made myself throughout this thesis. However, there is little experimental evidence as to the spatial extent to which spin-triplet correlations will persist. The exchange energy between bands may no longer be an issue, but other phenomena (spin-flip scattering, spin-orbit scattering) may still play a role in transport. Therefore, this project was intended to determine the length scale spin-triplet pair correlations can travel before decaying.

Conceptually, determining this length-scale should be no more difficult than growing a thicker Co/Ru/Co SAF in the middle of a S/F'/F/F"/S junction. However, a number of complications arise from this attempt. As Co is grown thicker, its lattice orientation switches from face-centered cubic (FCC) to hexagonal closed pack (HCP), causing the magnetization to become inhomogeneous [87]. In addition to altering the magnetization of the Co, the transition may cause more spin-flip scattering, shortening the spin-diffusion length compared to Co without a lattice transition, evident in the data in [90]. The spin-diffusion length is defined as the distance in a material an electron can diffuse before it encounters a spin-flipping collision, i.e. an up electron becomes a down or vice versa, and is given in the dirty limit by

$$l_{sf}^{F} = \sqrt{D_F \tau_{sf}^{F}} \tag{A.1}$$

where D_F is the diffusion constant in a ferromagnet and τ_{sf}^{F} is the mean time between spin-flip events [88]. This is dependent on a number of factors, including material and

temperature. The spin-diffusion length in Co has been measured at various temperatures, with results (in nm)

$$\begin{aligned} &= 38 \pm 12 \quad (T = 300K) \quad [89] \\ l_{sf}^{F} &= 59 \pm 18 \quad (T = 77K) \quad [89] \\ &\geq 40 \qquad (T = 4.2K) \quad [90]. \end{aligned} \tag{A.2}$$

The value at 4.2 K is an estimate extrapolated from thin samples due to an apparent change in length as samples were grown thicker [90].

Issues arising from fabricating junctions with thick Co have been observed when measuring the Fraunhofer patterns [91]. Using the geometry mentioned throughout this thesis (see Section 3.1 and Figure 3.1), critical current measurements in junctions with $d_{Co} < 15$ nm, and therefore total thickness $D_{Co} < 30$ nm, demonstrated clean Fraunhofer patterns. However, at $D_{Co} \geq 30$ nm, the patterns became too messy to determine a reliable peak value of the critical current.

Alternative materials were also used in the vertical geometry, including Co/Ni multilayers that have perpendicular anisotropy, i.e. with the magnetization pointing in the same direction as the current (Figure A.1) [92]. In those junctions, the Fraunhofer patterns were still very distorted in samples with 18 [Co/Ni] layers, or a total central ferromagnet thickness of 11.2 nm. From these results, it was clear that a new geometry would need to be developed to determine the range of spin-triplet pair correlations in ferromagnetic samples.

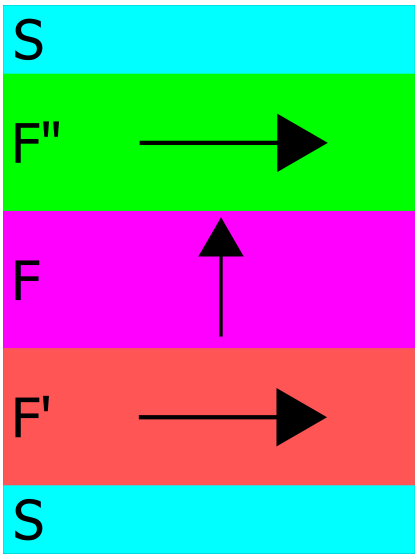

Figure A.1 *Cartoon of perpendicular magnetic anisotropy.* The F layer in this Josephson junction demonstrates this anisotropy as its magnetization points out of plane.

Sample Geometry and Fabrication

In order to keep Co thin, a lateral, or planar, geometry was chosen for this project. This is represented in Figure A.2. Seeing no reason to change the material, both Josephson junction and proximity effect samples were created with Co as F and Ni as the spin-mixing layer(s). The proximity effect samples were also tested with Ni as a base wire. Separate F and S layers were isolated from each other by Cu or Au spacing layers. The final structure for these junctions had a wire of [Co/Au](x) with junction lengths defined by two electrodes of Ni(1.5)/Cu(5)/Nb(55) for Josephson junction samples and a [Co/Au](x) or Ni(x) wire with Ni(1.5)/Cu(5)/Nb(60) contact for proximity effect samples. For the base wires, both the Co and Au were grown 15 nm thick and the Ni was 30 nm, but due to the lateral geometry, the distance between the electrodes (x) determines the length of the junction, so has been written above as [Co/Au](x) or Ni(x). For proximity effect samples, the length of the wire was typically 1 or 5 μm while the electrodes in the Josephson junction could be as narrow

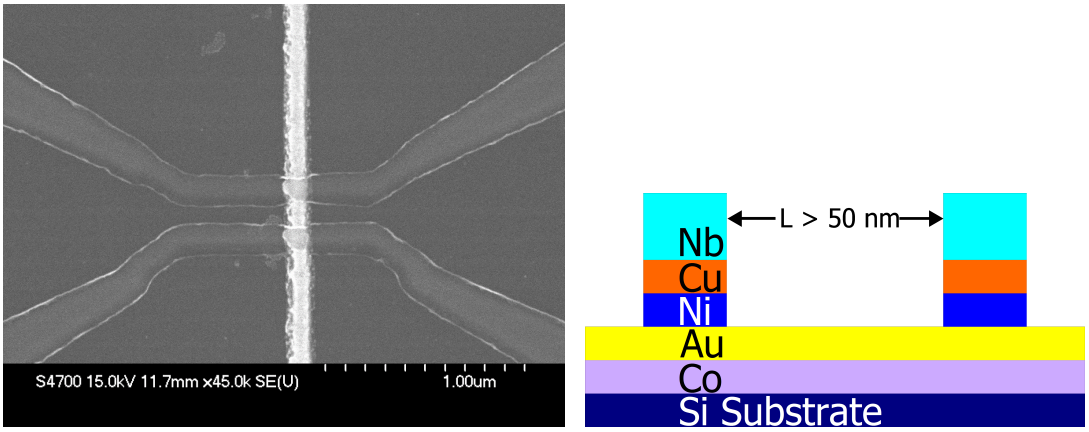

(a) (b)

Figure A.2 *Images of lateral Josephson junction.* In the SEM image (a), the bright vertical wire is the Co/Au bilayer and the dimmer horizontal wires are the Ni/Cu/Nb multilayer. A cartoon depiction of the side view is shown in (b). The Ni/Cu/Nb electrodes define the junction length, L.

as 50 nm, but typically were 100-150 nm.

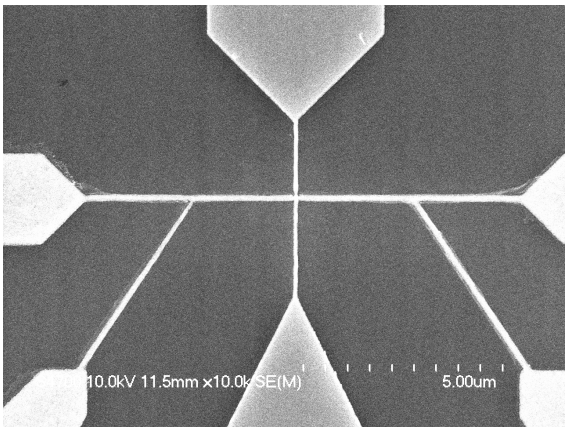

Figure A.3 *SEM image of a lateral geometry proximity effect sample.* The horizontal wire is the Co/Au bilayer, attaching to 4 leads for a 4-terminal measurement. The vertical wire is the Ni/Cu/Nb multilayer.

Considerations

Many iterations of the specific patterns were attempted, culminating with Figures A.2 and A.3. Through clever choices of geometry, many potential issues are avoided, some of which are listed below:

1. Co thickness is fixed along the length of the wire, so there are no structure transitions and therefore no direct length limitations in Josephson junctions.

2. Fabricating narrow, long wires creates a natural uniaxial shape anisotropy as mentioned in Section 2.1.1.

3. With $\vec{M}$ pointing along the wire, the current and magnetization become collinear. This, in principle, avoids a large magnetic flux contribution to the Fraunhofer patterns for the Josephson junction samples.

4. Being able to define the magnetization direction through wire features allows us to create a natural non-collinearity, more specifically one with orthogonal orientation, between neighboring ferromagnetic layers.

5. With a wider base wire away from the junction, there is a lower probability of breaks along the wire. This allows for 4 terminal interface resistances to be measured.

To avoid adverse effects at domain walls, fabrication was done in a way to promote single domain wires. To determine the domain structure, Co, Co/Au, and Co/Cu/Au wires were fabricated and measured with MFM. This work was done with Charles Moreau at Albion College in a manner very similar to work done in his previous paper [93]. Co/Au multilayers demonstrated the highest likelihood of single domain structure in the wire, especially after magnetization. This result is favorable because it also caps the Co layer, preventing it from oxidizing between fabrication steps. We also tested samples with Ni as a base layer, and the MFM was tested for those as well. They, too, showed single domain properties (Figure A.4).

An initial worry was that any positive results could be attributed by critics as super-current flowing through the Au layer. To account for that, samples with and without the

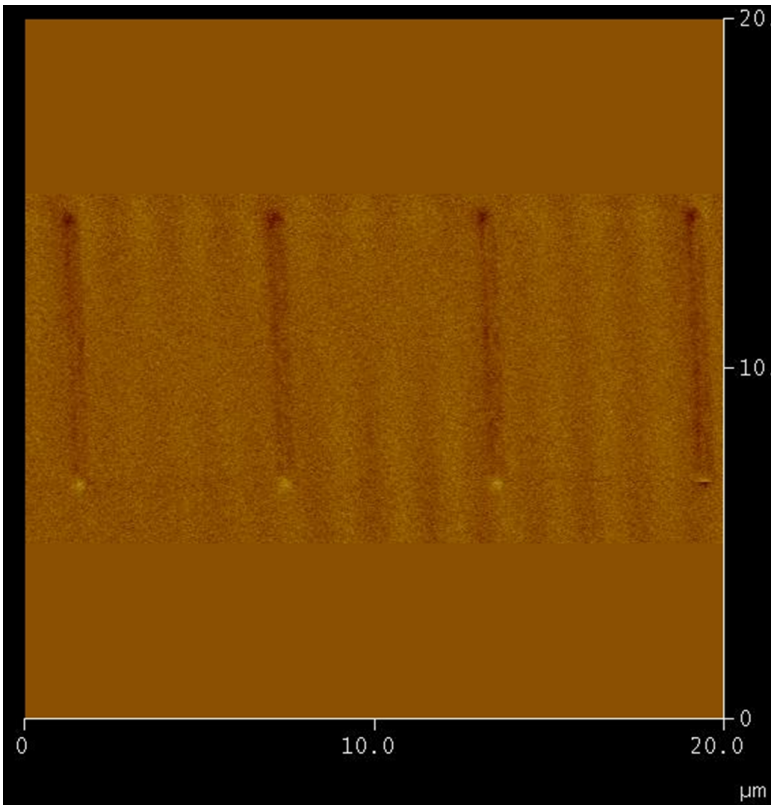

Figure A.4 *MFM results of Ni nanowires.* The dark and light dots at the ends of the wires, but nowhere else, demonstrate the single domain nature of the wires. The fringe pattern in the image is an artifact of the AFM.

spin-mixing Ni layers would be created. Similar to samples used in the initial spin-triplet discovery (Section 3.1), there should be a large difference in critical current (for Josephson junctions) or an appreciable difference in resistance (for proximity samples) between samples with and without Ni.

However, these concerns were largely quelled with theoretical [94] and experimental [95] results regarding ferromagnetic-normal metal bilayers. When a normal metal is grown on a ferromagnet, the normal metal decreases the exchange energy of the ferromagnet. However, the structure as a whole acts as a weak ferromagnet with a reduced exchange energy. This was demonstrated with S/N/S critical current measurements (N=Cu) that were compared to S/F-N/S critical currents (F=Fe, N=Cu) [95]. The results showed a dramatic decrease in critical current, reminiscent of the spin-singlet suppression in S/F/S Josephson junctions. Therefore, in our samples, even the Au channel in the Co/Au bilayer is spin-polarized, limiting the range of spin-singlet pair correlations.

Fabrication

The sample fabrication steps, demonstrated in Figure A.5, are the same between the two geometries with only the pattern written during the EBL step changing. The procedure follows:

1. Spin coat wafer with LOR-5B and S1813 bi-layer
2. Expose wafer to optical pattern, defining the large pads and leads
3. Evaporate Ti/Au and lift off resist
4. Protect and dice wafer

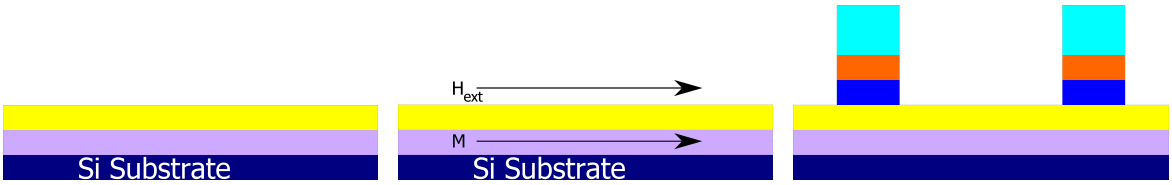

(a) Deposit the base wire (b) Magnetize the base wire (c) Deposit the top leads

Figure A.5 *Cartoons of lateral geometry fabrication steps.* Colors from bottom up: Dark blue – Si substrate; Light purple – Co; Yellow – Au; Blue – Ni; Orange – Cu; Light blue – Nb.

5. Lift off resist and clean chip

6. Spin coat MMA/MAA EL9 and PMMA C2 bi-layer

7. Define base pattern with EBL

8. Sputter base multilayer, Co/Au, and lift off resist

9. Protect the chip with S1813 and magnetize sample

10. Lift off resist and clean chip

11. Spin coat PMMA C2 mono-layer

12. Define top layer pattern with EBL

13. Light ion mill (∼2 nm) *in situ*, sputter top multilayer, Ni/Cu/Nb/Au, and lift off resist

Details of most of these steps can be found in Chapter 4. Initially, the entire structure was to be made in two EBL/sputtering steps, with the top layers being patterned as small wires at the junction but extending to the limits of the JEOL, writing at different magnifications in order to pattern the large pads for sample mounting as well. However, the initial attempts at this process revealed a major issue: the 5 nm Au (at the time kept thin to prevent a channel for supercurrent) did not have enough contrast in the SEM, making alignment impossible.

Instead, a photo mask was developed which contained alignment marks, leads, and mounting pads, done on a wafer scale to expedite the fabrication process.

The magnetization step was added to increase the probability of creating single domain wires. Because this is done outside of the cleanroom, chips are spun with S1813 first, protecting it from dust and other contaminants. The chips are placed in an electromagnet which is brought up to ∼150 mT. The chips are then brought back into the cleanroom where the resist is removed in acetone, and the chips are ready for the rest of the fabrication process.

The ion mill step before the second sputtering run is done to ensure the interface is clean. For this project especially, the resistance at the interface was a major concern. Because the materials are not sputtered *in situ*, there is the possibility of contamination, for example from resist residue, at the interface that a simple ion milling step can alleviate.

Fabrication Issues

The geometry attempted in this project had never been used before and was therefore developed from scratch during this process. As such, many complications, adjustments, and restarts followed, as one would expect. I have already touched on one of them, in that the initial pattern had no way to align, and therefore an entirely new process was developed to incorporate optical base leads. What follows are other main complications that arose, although I do not claim this is an exhaustive list.

Sidewall

The sputtering system is an uncollimated system, as discussed in Section 4.1.2.2. However, the extent of the spread and its effect hadn't been quantified until very narrow wires were

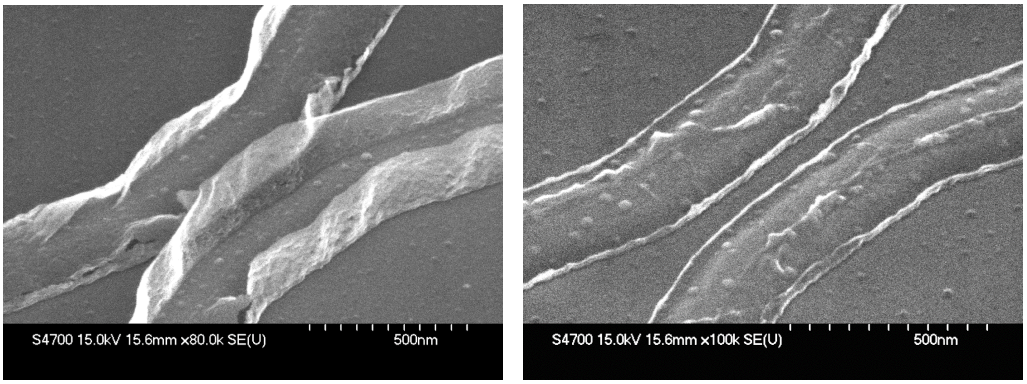

(a) Sidewall buildup due to wide sputtering angle.

(b) Sidewall eliminated through collimation.

Figure A.6 *Images of sidewall issues.*

sputtered. While not an issue for soft materials such as Au, sputtered Nb wires demonstrated a large side wall deposition, sometimes collapsing on the junction but often standing rigid. This is shown in Figure A.6a. This happens because, due to the relative thicknesses of the upper and lower resist layers in the bilayer, the allowed deposition angles of the sputtered material are so wide that resist deposits on the edges. A cartoon representation of this is demonstrated in Figure A.7a.

To eliminate the sidewall, the sputtered material must be better collimated. This can be by changing the resist profile, as demonstrated in Figure A.7b [96], or by adding a mechanical collimator, a long, narrow tube that is placed over the sample during deposition that geometrically limits the spread of material (Figure A.7c). While attempts to manipulate the resist profile will appear again, mechanical collimation was added to the processing, eventually becoming a permanent aspect of sputtering the base layer. Figure A.6b shows the the effect of collimating during the sputtering step.

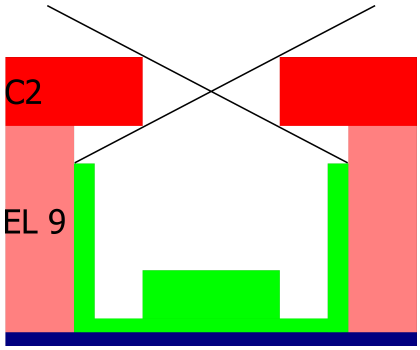

(a) EL9/C2 bilayer profile

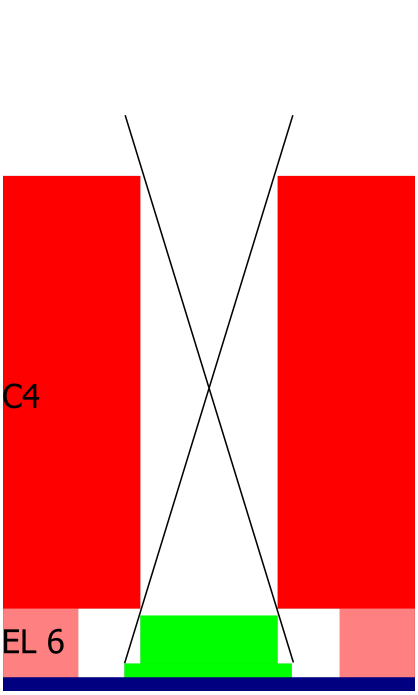

(b) EL6/C4 bilayer profile

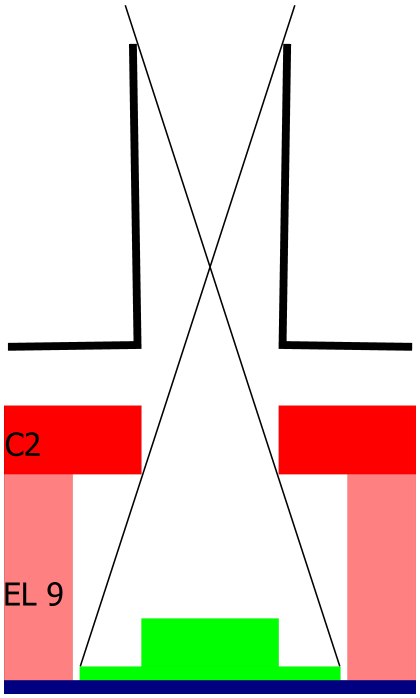

(c) EL9/C2 bilayer profile with a collimator

Figure A.7 *Cartoons of resist profiles.* The black lines represent the angles allowed based on resist geometry. (a) demonstrates uncollimated sputtering, while (b) shows self-collimation from the resist profile. (c) demonstrates the ability to reduce spread from a mechanical mask.

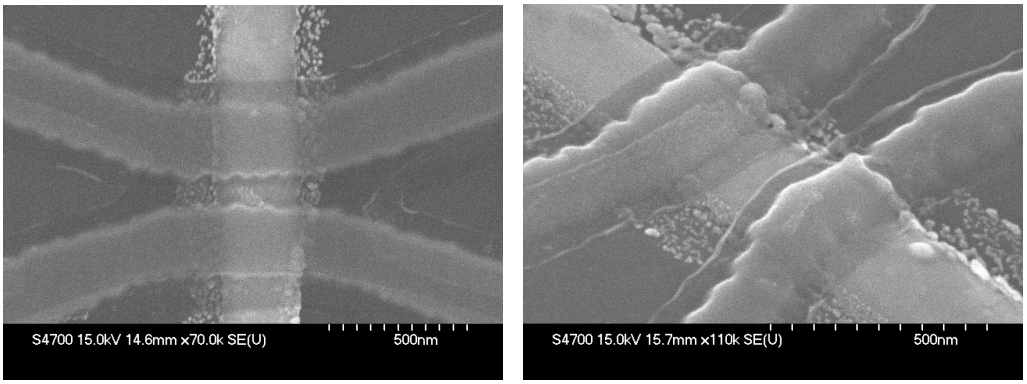

(a) (b)

Figure A.8 *Images of junction definition concerns.* In the top down view (a), there are faint white lines between the top leads, left and right of the junction. These lines are the edges of the top leads, and are in contact at the junction. These are more clear in the angled view, which, in this sample, shows separation between the electrodes, but their defining edges are still unclear.

Junction Definition

Even though the collimators reduced the spread enough to eliminate sidewall buildup, there was still a bit of spread in the deposited material. While this is useful for the base layer deposition, of which rigid edges could cause problems when growing the top layer, the electrodes deposited during the final step need to be well defined. Without distinct edges, how can we know what the length of the Josephson junction is? In addition, how can we guarantee there isn't a short in the electrodes? This concern is demonstrated in Figure A.8.

At this point, self-collimation from resist profiles was considered and attempted. Various combinations of resists were used, two of which being attempted the most: MMA/MAA EL9 with PMMA C2, the original combination, and MMA/MAA EL6 with PMMA C4, which both decreases the base layer thickness and also increases that of the top layer. Once again, these profiles can be seen in Figure A.7. With the resist profile taking care of the collimation, the mechanical collimators could be removed, increasing the sputtering rate dramatically.

While in principle this should have worked, the resulting samples often demonstrated odd

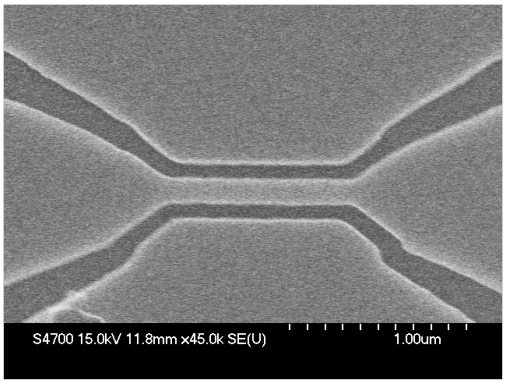

(a)

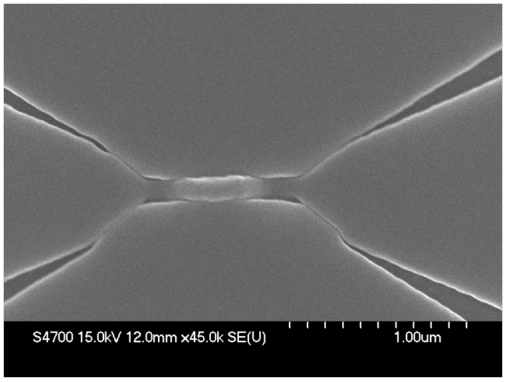

(b)

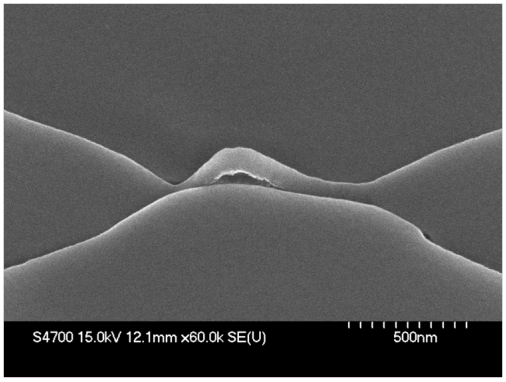

(c)

Figure A.9 *Images of resist deformation.* All images are taken after sputtering but before liftoff. In (a), we see the shape and structure of the junction without any deformation. In (b) we can see the wires have been pinched, the extent of the buckling visible in (c), which was taken at a 45-degree angle.

deposition, and sample reproducibility became a massive concern. While not immediately obvious, this was caused by deformation of the resist when in the sputtering chamber. At some point during sputtering, strains due to temperature excursions, either from cooling or more likely overheating, caused buckling behaviors, as seen in Figure A.9. A suggested solution was to utilize a PMMA monolayer [97]. Although this eliminates the undercut, potentially leaving rigid edges in the deposited material, it allows for very precise definition of the sputtered layer. After attempting this, the liftoff removed any of our concerns and progress could continue.

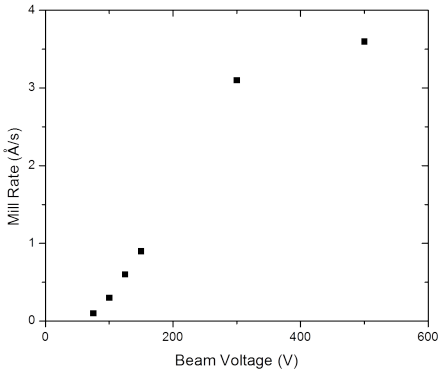

(a) Plot of mill rate vs beam voltage.

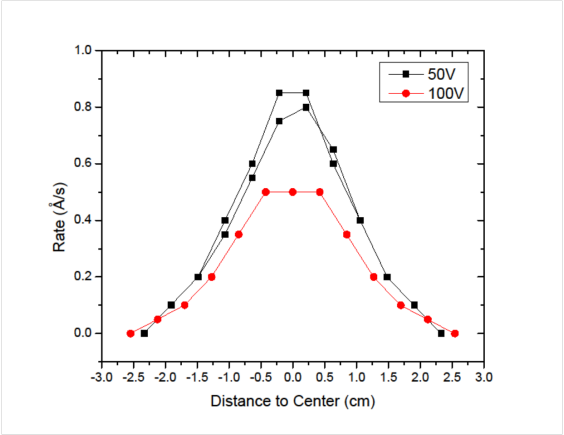

(b) Plot of mill rate vs. position, relative to accelerator voltage.

Figure A.10 *Plots of ion mill characteristics.* The mill rate relative to beam energy is plotted in (a), demonstrating the lower threshold of appreciable beam voltage. The beam profile is plotted in (b), demonstrating the amount of spread present in the mill relative to accelerating voltage. The mill rates with an accelerating voltage of 50 V were measured twice, represented by two sets of data in (b).

Mill Damage and Sputtering Alignment

Initially, samples were ion milled with the same parameters used to mill and define pillar dimensions. However, samples made this way were unsuccessful, and we found evidence of damage to the base wire due to the ion mill. Further reading led us to realize the beam energy plays a major role in how milling takes place, as well as the potential damage caused [98], so we needed to characterize our mill. This included the beam energy as well as the beam profile.

To determine the acceptable range of beam energy, we measured the milling rate vs beam voltage, displayed in Figure A.10a. We wanted to mill at low energies to avoid unnecessary damage, but not right at the threshold, limiting the effect of the cleaning entirely. Typically this meant the mill was set between 125 and 135 V, but voltages as high as 175 V had be used at times.

We then had to determine the profile of the mill which, according to the manual [99], is largely effected by the accelerating voltage. To measure this, we rotated the sample holder over the mill while the FTM measured the milling rate for each position in the stepping motor. The results are plotted in Figure A.10b. From this, it was determined that the accelerating voltage should be turned up to 100 V, yielding a slightly broader profile. More importantly, because the beam profile for milling is so narrow we needed to recalibrate the sputtering chamber, which also improved deposition due to the limiting angles of the collimators. To do this, Reza Loloee and I measured the position of every sample holder/target gun combination and reprogrammed the system accordingly. This was done once again by Reza and Victor Aguilar when a new sputtering program was developed.

Measurement Setup

Quick Dippers

Like the other work described in this thesis, the lateral geometry samples were also dipped into a liquid helium storage dewar on various Quick Dipper probes. However, the probes used for these measurements have been highly modified to obtain much lower temperatures, and are explained here. As there are many manuals, checklists, and procedures, written by William Pratt, Reza Loloee, Joseph Glick, and myself, accessible to anyone using these systems, I will forgo discussions on mounting and operation and discuss only the relevant aspects of each dipper. However, I will mention that these samples are much more sensitive to static discharge, and therefore grounding straps must be worn and the probe must be grounded when mounting.

Quick Dipper V (QD-V) is a semi-permanent fixture attached to a liquid helium storage dewar. It is effectively a hollow cylindrical shell, isolated from the dewar with a vacuum jacket, that is placed deep into the dewar. It can be filled by opening a capillary tube, allowing liquid helium to flow from the outside in while the level is monitored by Cernox resistors that change resistance when covered with helium. QD-V is also attached to a roughing pump. Through evaporative cooling while being pumped on, the temperature of the liquid helium drops, reaching a minimum temperature of $\sim$1.1 K in this system. This temperature was once measured with a conductance bridge, although recently a Lakeshore Model 350 Temperature Controller has replaced it.

Quick Dipper VI (QD-VI) is a very basic probe that has 6 voltage leads and 6 current leads running from the outside to the sample. It has, however, been designed to be dipped into QD-V. By using this combination, it is possible to measure samples from 1.2 K to 4.2 K reliably.

Quick Dipper VII (QD-VII) is a remarkable probe that took years to engineer. It features a vacuum can and a ^{3}He pot. By dipping it into and lowering the temperature of QD-V, the ^{3}He liquefies above the sample holder. By using a charcoal pill on a magnetic arm, this liquid ^{3}He can be pumped on, decreasing the temperature of the sample down to 0.32 K.

Measurement

The measurement techniques used for the Josephson junctions and the proximity effect samples differed quite a bit, and as such I will describe them separately. However, all measurements are 4 terminal, utilizing a lock-in to obtain minimal noise. While the initial proximity effect measurements were taken by hand, LabVIEW programs have been developed by Victor Aguilar to automate the data collection. The Josephson junction programs were

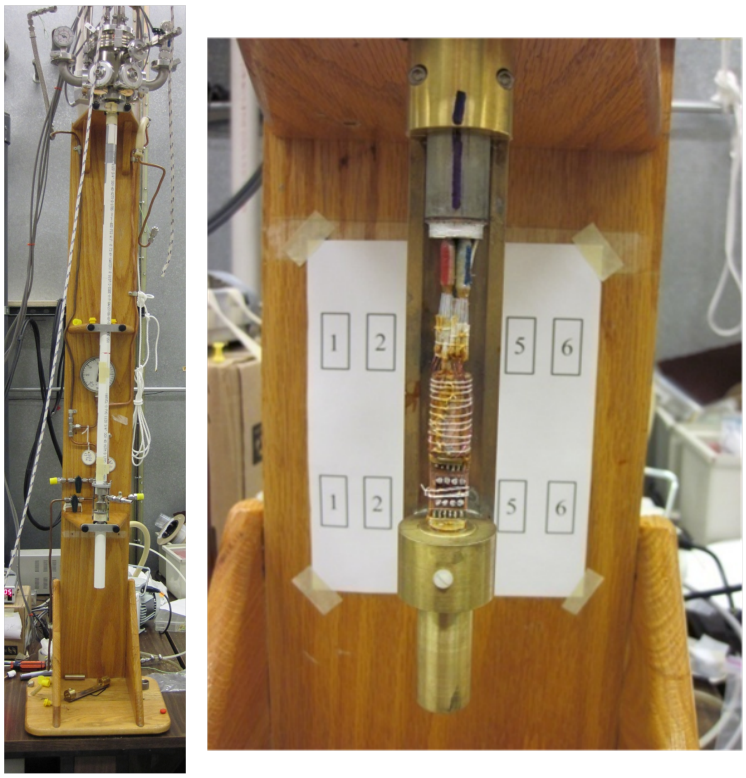

(a) (b)

Figure A.11 *Images of QD-VII.* The entire dipper is shown in (a), including the system required to pump out the vacuum can. A close up of the mounting area is shown in (b).

written and modified by several past and present group members.

The Josephson junction data were taken in a standard differential resistance measurement. Using the concept of load lines [100] (Figure A.12), voltages supplied by a Tektronix AFG 3022B Function Generator and SRS Model SR850 DSP Lock-in Amplifier were added together, from which a current source was created via a ballast resistor (typically set to 10 kΩ for these experiments). The circuit is shown in Figure A.13. The function generator supplied the system with a very slow (typically 2 mHz) sawtooth-patterned voltage, effectively supplying a DC current to the sample. On top of this, a fast (typically 98 Hz), small AC signal was added from the lock-in amplifier. This measurement scheme allows us to measure $\frac{dV}{dI}$ vs I curves. Effectively, this can be thought of as measuring the instantaneous resistance of the sample at every current increment. In relation to Figure A.12, this can be pictured as slowly sliding the red line along the x-axis, measuring the slope of the curve at each point. If desired, a more traditional I-V curve can be obtained by integrating the output with respect to current.

The important data for proximity effect chips are that of resistance vs temperature (R vs T). As the superconducting pair correlations penetrate into the ferromagnetic wire, the resistance of the wire should drop. The longer the coherence length, the more the resistance should change. Therefore, the measurement does not need to be any more than a standard 4 terminal resistance measurement. However, because the effect is small relative to the normal resistance of the wire, a ratio transformer is used (see Section 6.2.2 and Figure 6.8). By subtracting off the normal resistance of the wire, a much more resolved measurement of the changes in resistance as an effect of temperature are possible.

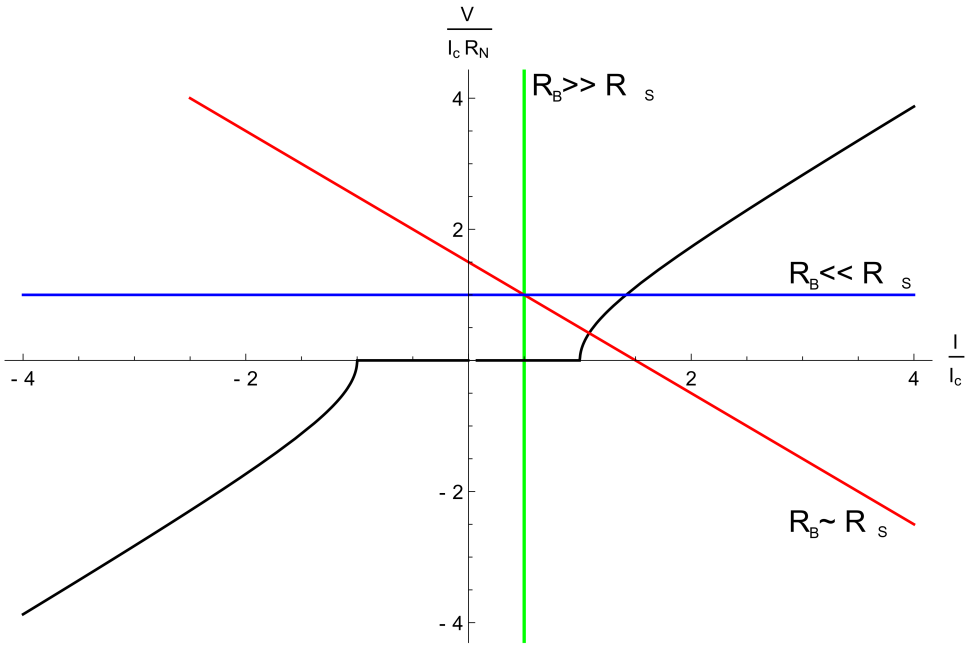

Figure A.12 *Diagram of various load line schemes.* The following examples are for measuring $\frac{dV}{dI}$ vs I in a Josephson junction: if $R_B \ll R_s$ (blue), details in the normal state and near the critical current are well resolved, but the superconducting gap is almost entirely missed; if $R_B \gg R_s$ (green), measurements within the superconducting gap are well resolved, but not the details near the critical current. A good balance is obtained for $R_B \approx R_s$, which can measure points within the gap, near the normal transition, and while the sample is normal.

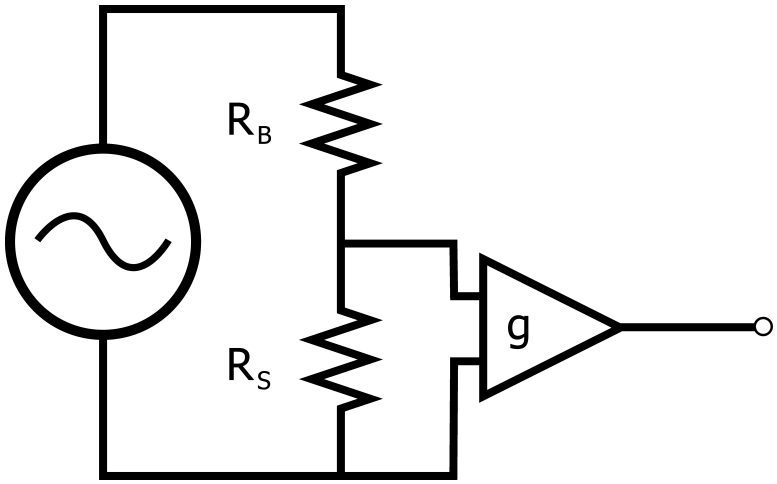

Figure A.13 *Circuit diagram for lateral geometry Josephson junction measurements.* The ballast resistor (R_B) turns the voltages from the lock-in and function generator into AC and DC components of the current, respectively. The output is measured with the lock-in. Often, no pre-amp was used, so g=1, although a pre-amp with g=100 was used on occasion.

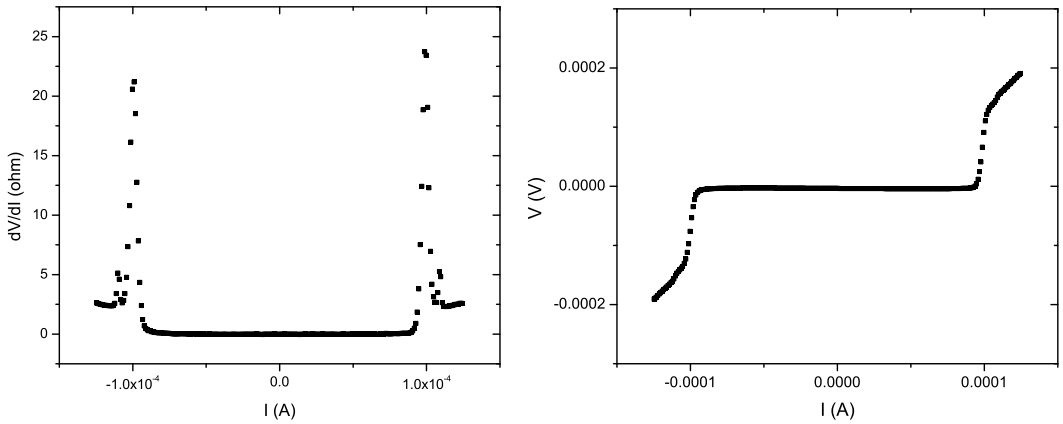

(a) (b)

Figure A.14 *S/N/S Josephson junction measurements.* dV/dI measurement (a) and integrated I-V curve of the same data (b). Width of the Au wire is ∼100 nm, with Nb electrode separation of ∼100 nm; $T = 0.33$ K.

Data

In samples made with no ferromagnetic material, the measured critical current became larger with decreased temperature, as expected. This is shown in Figures A.14a and A.15. These results left us confident that we could fabricate junctions with ferromagnetic layers in this geometry. Adding different material should not change that.

However, changing the material had a very large effect. In samples without F' layers, we observed no critical current (Figure A.16a). This is not a surprise, given that we were generating no spin-triplet pair correlations. When we added the Ni spin-mixer layer, completing the S/F'/F/F'/S configuration, we still observed no positive results (Figure A.16b). The data shown are not unique to the particular sample. Measured samples across various sputtering runs and fabrication techniques, made over years of fabrication, all show similar trends.

Some other groups have attributed similar trends in their data to charge imbalance, a consequence of injecting electrons into quasiparticle states above the superconducting gap

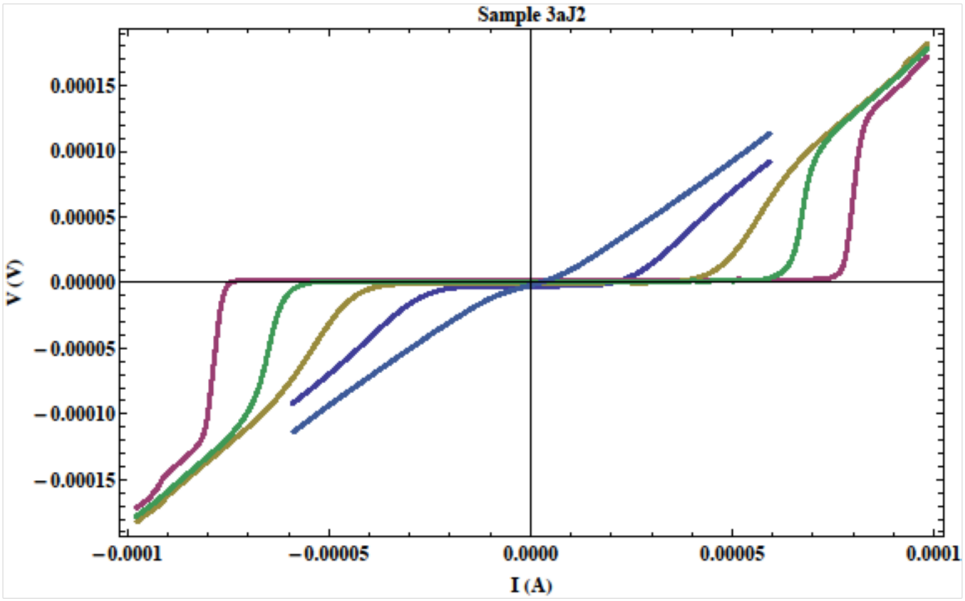

Figure A.15 *Temperature dependence on S/N/S critical current.* Width of the Au wire is ∼100 nm, with Nb electrode separation of 120 nm. Temperatures are listed from the inside curve out: Light blue – 3.55 K; Dark blue – 2.55 K; Yellow – 1.91 K; Green – 1.55 K; Purple – 1.22 K.

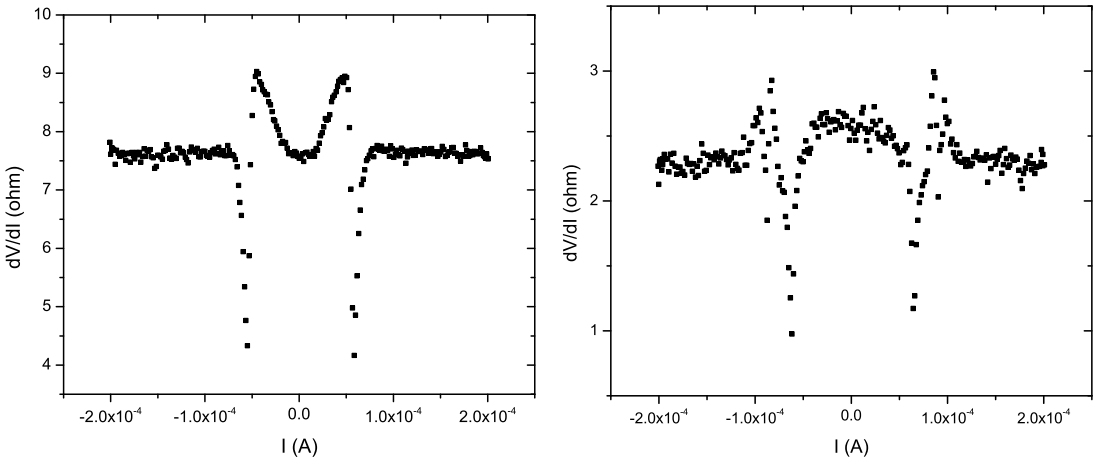

(a) S/F/S Josephson junction measurement.

(b) S/F'/F/F'/S Josephson junction measurement.

Figure A.16 *S/F/S and S/F'/F/F'/S Josephson junction measurements.* In (a), there is no spin-mixer, so critical current is neither expected nor observed. Adding Ni spin-mixer layers (b) should show either critical current or proximity effect (lower resistance at low drive). However, this is not observed. S-Nb; F-Co/Au bilayer; F'-Ni. $T = 0.34$ K for both samples.

[101]. Their results mimic our trend rather closely. However, we do not believe the effect seen in our samples is due to this. Charge imbalance is most important near T_c or under strong current drive. The current that this effect occurs at in our S/F'/F/F'/S samples is much lower than the critical current in our S/N/S junctions.

The data from proximity effect samples, which should be more clear as they are less complicated systems, were even more confusing (Figure A.17). Fabrication of these samples were done the same way as in the Josephson junctions, sometimes even in the same sputtering runs. Despite this, while an S/N/S Josephson junction demonstrated supercurrent, the proximity effect measured in a normal metal was unreliable. The S/N junction shown in Figure A.17a has the largest decrease in resistance, about 10% by 0.3 K. However, the superconducting lead covers about 10% of the Au wire, which opens a pathway for current to travel through the superconductor, as demonstrated in Figure A.19b. This region of superconductivity should drop the resistance of that length to 0. Taking into account this "shorting" through the superconductor, in addition to the proximity effect we expect to see, we therefore expect the decrease in resistance of the entire wire to be much larger than we measure our samples.

The results in samples with ferromagnetic material are even less clear. In those with no spin-mixer layer, i.e. S/F samples, we have measured a very small drop in resistance, less than 1% (Figure A.17b). When adding a second F layer as a spin-mixer, the data are mysterious and inconsistent. As shown in Figure A.17c, we observe excursions from the normal resistance of the wire at higher temperatures ($\sim$9 K) when compared to other samples ($\sim$5 K). There does not seem to be a consistent drop in resistance, but rather multiple jumps, implying the presence of multiple effects. The resistance also increases and plateaus below $\sim$4 K. In one sample (Figure A.17d), the resistance never decreases but rather

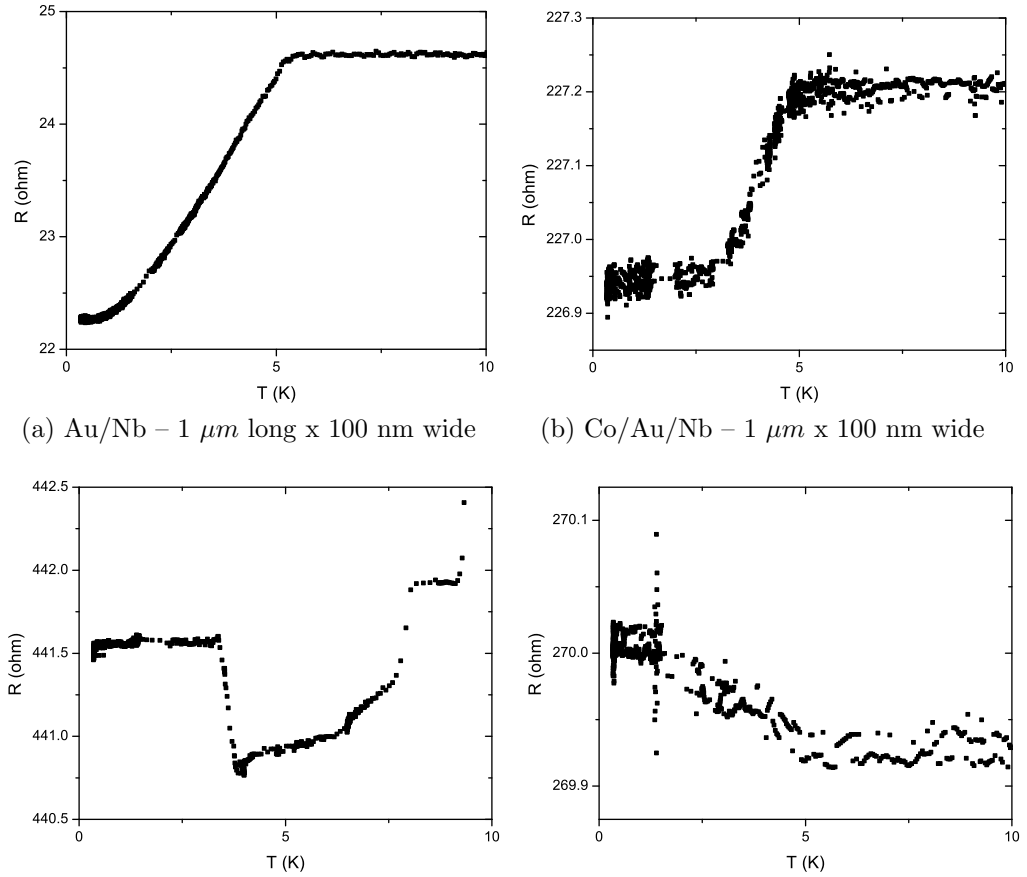

(a) Au/Nb – 1 μm long x 100 nm wide

(b) Co/Au/Nb – 1 μm x 100 nm wide

(c) Co/Au/Ni/Cu/Nb – 1 μm x 100 nm wide

(d) Co/Au/Ni/Cu/Nb – 5 μm x 100 nm wide

Figure A.17 *Data from Rvs.T proximity effect measurements.*

an increase is measured as the temperature decreased (Figure A.17d). These results are not well understood.

Other groups have reported resistance changes that are much larger than those measured in our samples. In a 40 nm long Co nanowire, one group observed 0 resistance, i.e. a Josephson effect, when measuring the wire with superconducting W electrodes [102]. Eliminating any Josephson effect, they replaced W with Pt electrodes, and added a small W contact between the voltage leads, inducing superconducting proximity effect. In these samples, they reported a "normal metal coherence length" of hundreds of nm in Co. It should be noted that these samples did not have a spin-mixing layer, but it is likely that the FIB used in

the fabrication process created a spin-mixing interface. Similar results were also reported recently, again in Co nanowires in contact with a narrow W strip, about 220 nm wide [103]. Although the superconductor was in contact with the ferromagnetic wire over ∼6% of its length, the drop in resistance between 5.2 K and 2.4 K was 22%. This result is not only much larger than in our S/F samples, but larger than in our S/N samples as well.

We even tried to measure the proximity effect in the Josephson junction samples, the data from an S/F'/F/F'/S sample are shown in Figure A.18. The trends are once again similar to those observed by other groups: the increase at very low temperature is similar to the re-enterance effect observed in the 90s [104]; the sharp peak near 6 K is similar to an effect measured in other Co nanowire/superconductor systems [102], which was claimed to possibly be due to charge or spin imbalance, but not conclusively known. We believe the rapid change in resistance between 6 and 7 K is due to non-uniform current density that emerges when the electrodes are normal, i.e. $T > T_c$. With the geometry as it is, when the Nb is non-superconducting, the path the current takes may not overlap entirely with the voltage leads, dropping the measured resistance substantially. Overall, while the trends present in our data are similar to those seen in other work, we are not convinced the effects are the same.

Discussion and Outlook

The results of these projects are confusing and, if I may say, disappointing. The results obtained through fabrication of S/N/S samples, especially those that demonstrate typical temperature dependence of the Josephson critical current, imply that our sample fabrication is optimized. However, no Josephson junction samples with ferromagnets demonstrated

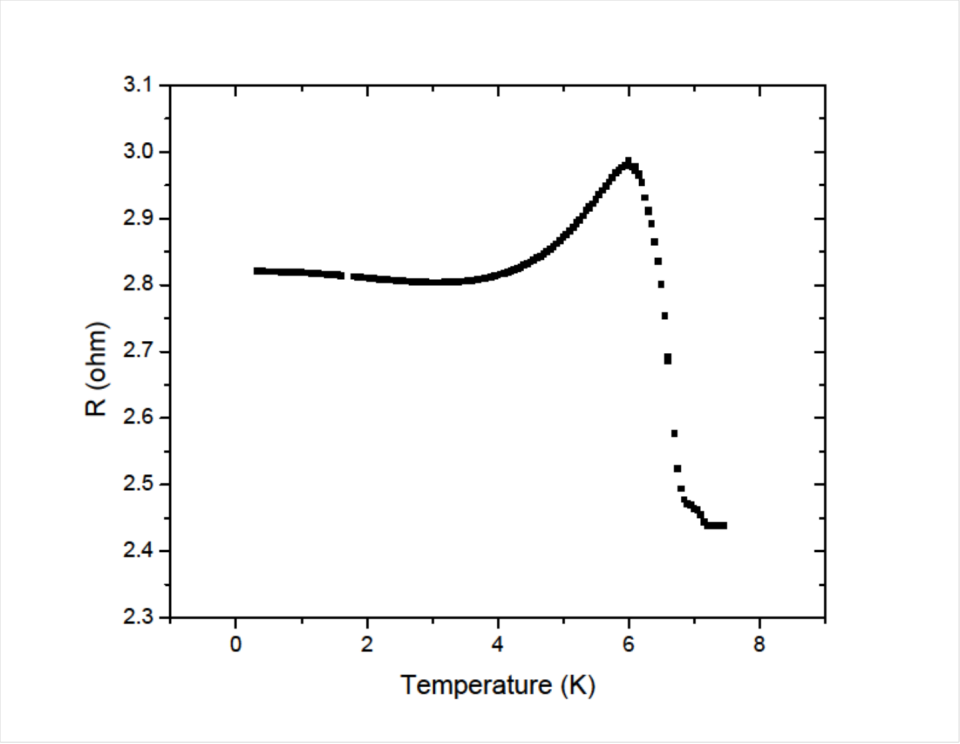

Figure A.18 *Proximity effect in Josephson junction samples.*

successful results. The same can be said about the proximity effect results.

Some other groups have seen signatures similar to ours in their data, claiming charge or spin imbalance as a possible explanation. However, we do not believe this is the case in our samples, at least not the full picture. In the end, the reason for the samples behaving as they do is still a mystery to us. Despite reason to think that they are clean, the problem likely arises from some issue at the interface. What that issue is, however, is unknown.

What does that mean for the future of this project? Either material or geometry changes may be in our future yet. I must first acknowledge the work discussed before by Golikova *et al.* regarding F-N bilayers [95]. Their samples were grown with an e-beam evaporator, equipment that we do not have access to at our facility. However, slight adjustments to their patterning, entirely based around finding a way to introduce a non-collinear magnetization layer, could be all that is required to make lateral S/F'/F/F'/S samples.

Separately, if we could find a material that has perpendicular anisotropy and is a good spin-triplet generator, we could avoid fabrication and interface issues by doing all of the deposition in one step. If the entire multilayer is deposited in the same way our pillars are, we could mill a small gap in the wire, milling through all of the layers except the final F layer. In this way, we would have non-collinearity (F' layer magnetization points out of plane, base wire magnetization points along the wire), we could control the length of the junction, and every interface would be deposited *in situ*. However, this magic material has not been found yet. Perhaps one day a student will pick up where I left off and successfully measure supercurrent in these lateral geometry Josephson junctions using the possibilities above.

As for the proximity effect samples, a lot more troubleshooting needs to be done. Part of the concern is that we may be seeing shorting through the superconducting wire where it crosses the ferromagnetic wire. To eliminate this concern, we could attempt different geometries that avoid wire crossing, one example of which is demonstrated in Figure A.19c.

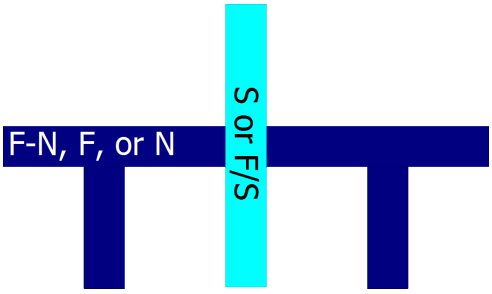

(a) Current proximity effect sample geometry

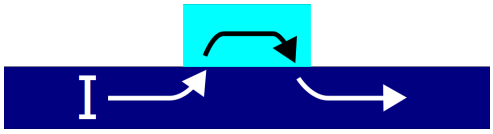

(b) Cartoon demonstrating possible shorting of current through superconducting wire

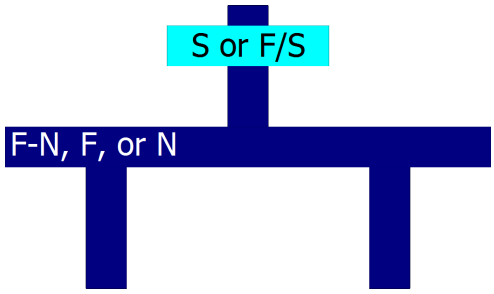

(c) Potential future proximity effect geometry

Figure A.19 *Proximity effect geometries.* The current geometry is displayed in (a). Due to the superconductor making contact with the current-carrying wire, shorting through S could cause a resistance drop unrelated to the proximity effect (b). By moving the superconductor away from the wire, as demonstrated in (c), a more direct measure of the proximity effect is possible.

BIBLIOGRAPHY

BIBLIOGRAPHY

[1] H. Kammerling Onnes, *Leiden Comm.* **120b, 122b, 124c** (1911).

[2] J. Bardeen, L.N. Cooper, J.R. Schrieffer, *Phys. Rev.* **108**, 1175 (1957).

[3] J. Orenstein and A. J. Millis, *Science* **288**, 468 (2000).

[4] T. Tohyama *Jpn. J. Appl. Phys.* **51** 010004 (2012).

[5] S. Hassan, Humaira, M. Asghar, *Proc. ICCSN '10* 559 (2010).

[6] High-performance computing results can be found at http://www.top500.com .

[7] M. W. Johnson *et al.*, *Nature*, **473**, 194 (2011).

[8] T. F. Rønnow *et al.*, *Science*, **345**, 420 (2014).

[9] D. S. Holmes, A. L. Ripple, M. A. Manheimer, *IEEE Trans. Appl. Supercond.* **23**, 1701610 (2013).

[10] K. K. Likharev and V. K. Semenov, *IEEE Transactions on Applied Superconductivity* **1**, 3 (1991).

[11] N. O. Birge, to appear in *Phil. Trans. R. Soc. A.*

[12] A. I. Buzdin, *Rev. Mod. Phys.* **77**, 3 (2005).

[13] F. S. Bergeret, A. F. Volkov, K. B. Efetov, *Rev. Mod. Phys.* **77**, 4 (2005).

[14] C. Kittel, *Introduction to Solid State Physics, Seventh Ed.* John Wiley & Sons, New York (1996).

[15] D. J. Griffiths, *Introduction to Quantum Mechanics, Second Ed.* Pearson Education, Upper Saddle River (2005).

[16] W. Heisenberg, *Z. Physik* **49**, 619 (1928).

[17] N. W. Ashcroft, N. D. Mermin, *Solid State Physics*. Holt, Rinehart and Winston, New York (1976).

[18] K.H.J. Buschow, *Handbook of Magnetic Materials, vol. 23*. North-Holland, Oxford (2015).

[19] Nicola A. Spaldin, *Magnetic Materials, Fundamentals and Applications*. Cambridge University Press, Cambridge (2011).

[20] P. Weiss, *J. Phys.* **6**, 661 (1907).

[21] H. Barkhausen, *Z. Phys.* **20**, 401 (1919).

[22] L. Solymar, D. Walsh, R. R. A. Syms, *Electrical Properties of Materials, Ninth Edition*. Oxford University Press, Oxford (2014).

[23] F. Bitter, *Phys. Rev.* **38**, 1903 (1931).

[24] H. J. Williams, F. G. Foster, E. A. Wood, *Phys. Rev* **82**, 119 (1951).

[25] L.N. Cooper, *Phys. Rev.* **104**, 1189 (1956).

[26] Michael Tinkham, *Introduction to Superconductivity, Second Edition*. Dover Publications, Inc., New York (1996).

[27] W. Meissner, R. Ochsenfeld, *Naturwissenschaften* **21**, 787 (1933).

[28] A. F. Andreev, *Sov. Phys. JETP* **19**, 1228 (1963).

[29] P. Flude, R. A. Ferrell, *Phys. Rev.* **135**, A550 (1964).

[30] A. I. Larkin, Y. N. Ovchinnikov, *Zh. Eksp. Teor. Fiz.* **47** 1136 (1964).

[31] A. I. Larkin, Y. N. Ovchinnikov, *Sov. Phys.–JETP* **20** 762 (1965).

[32] C. J. Lambert, R. Raimondi, *J. Phys.: Condens. Matter* **10**, 901 (1998).

[33] W. Belzig, F. K. Wilhelm, C. Bruder, G. Schon, A. D. Zaikin, *Superlattices and Microstructures* **25**, 1251 (1999).

[34] E. A. Demler, A. B. Arnold, M. R. Beasley, *Phys. Rev. B* **55**, 15174 (1997).

[35] T. Muhge, N. N. Garifyanov, Y. V. Goryunov, G. G. Khaliullin, L. R. Tagirov, K. Westerholt, I. A. Garifullin, H. Zabel, *Phys. Rev. Lett.* **77(9)**, 1857 (1996).

[36] J. S. Jiang, D. Davidovic, D. H. Reich, C. L. Chien, *Phys. Rev. Lett.* **74(2)**, 314 (1995).

[37] T. Kontos, M. Aprili, J. Lesueur, X. Grison, *Phys. Rev. Lett.* **86(2)**, 304 (2001).

[38] V. V. Ryazanov, V. A. Oboznov, A. Y. Rusanov, A. V. Veretennikov, A. A. Golubov, J. Aarts, *Phys. Rev. Lett.* **86(11)**, 2427 (2001).

[39] T. Kontos, M. Aprili, J. Lesueur, F. Genet, B. Stephanidis, R. Boursier, *Phys. Rev. Lett* **89(13)** 137007 (2002).

[40] B. D. Josephson, *Phys. Lett.* **1**, 251 (1962).

[41] B. D. Josephson, *Adv. Phys.* **14**, 419 (1965).

[42] R. P. Feynman, R. B. Leighton, M. Sands, *The Feynman Lectures on Physics, Vol III.* Addison-Wesley Publishing Company, Massachusetts (1965).

[43] V. Ambegaokar, B. I. Halperin, *Phys. Rev. Lett.* **22**, 25 (1969).

[44] M. Giroud, H. Courtois, K. Hasselbach, D. Mailly, B. Pannetier, *Phys. Rev. B* **58(18)**, R11872 (1998).

[45] M. D. Lawrence, H. Giordano, *J. Phys.: Condens. Matter* **11**, 1089 (1999).

[46] V. T. Petrashov, I. A. Sosnin, I. Cox, A. Parsons, C. Troadec *Phys. Rev. Lett.* **83(16)**, 3281 (1999).

[47] F. S. Bergeret, A. F. Volkov, K. B. Efetov, *Phys. Rev. Lett.* **86(18)**, 4096 (2001).

[48] A. Kadigrobov, R. E. Shekhter, M. Jonson, *Low Temp. Phys.* **27(9-10)**, 760 (2001).

[49] Y. V. Fominov, A. F. Volkov, K. B. Efetov, *Phys. Rev. B* **75**, 104509 (2007).

[50] T. Champel, T. Löfwander, M. Eschrig, *Phys. Rev. Lett.* **100**, 077003 (2008).

[51] A. F. Volkov, F. S. Bergeret, K. B. Efetov, *Phys. Rev. Lett.* **90**, 117006 (2003).

[52] M. Eschrig, T Löfwander, *Nature Physics* **4**, 138 (2008).

[53] Matthias Eschrig, "Spin-polarized supercurrents for spintronics." *Physics Today* **64**, 43 (2011).

[54] M. Houzet, A. I. Buzdin, *Phys. Rev. B* **76**, 060504(R) (2007).

[55] R. S. Keizer, S. T. B. Goennenwein, T. M. Klapwijk, G. Miao, G. Xiao, A. Gupta, *Nature* **439**, 825 (2006).

[56] I. Sosnin, H. Cho, V. T. Petrashov, A. F. Volkov, *Phys. Rev. Lett.* **96(15)**, 157002 (2006).

[57] T. S. Khaire, M. A. Khasawneh, W. P. Pratt, Jr., N. O. Birge, *Phys. Rev. Lett.* **104**, 137002 (2010).

[58] M. A. Khasawneh, W. P. Pratt, Jr., N. O. Birge, *Phys. Rev. B* **80**, 020506(R) (2009).

[59] C. Klose *et al.*, *Phys. Rev. Lett.* **108**, 127002 (2012).

[60] Y. Wang, Ph.D. Thesis, Michigan State University, United States (2010).

[61] Y. Wang, W. P. Pratt, Jr., N. O. Birge, *Phys. Rev. B* **85** 214522 (2012).

[62] C. Klose, Bachelors Thesis, Universität Konstanz, Germany (2010).

[63] V. A. Oboznov, V. V. Bol'ginov, A. K. Feofanov, V. V. Ryazanov, A. I. Buzdin, *Phys. Rev. Lett.* **96**, 197003 (2006).

[64] B. Baek, W. H. Rippard, S. P. Benz, S. E. Russek, P. D. Dresselhaus, *Nat. Commun.* **5**, 3888 (2014).

[65] B. M. Niedzielski, unpublished data.

[66] B. M. Niedzielski, E. C. Gingrich, R. Loloee, W. P. Pratt, Jr., N. O. Birge, *Supercond. Sci. Technol.* **28**, 085012 (2015).

[67] J. W. A. Robinson, J. D. S. Witt, M. G. Blamire, *Science* **329**, 59 (2010).

[68] D. Sprungmann, K. Westerhold, H. Zabel, M. Weides, K. Kohlstedt, *Phys. Rev. B* **82**, 060505(R) (2010).

[69] J. Wang, M. Singh, M. Tian, N. Kumar, B. Z. Liu, C. Shi, J. K. Jian, N. Samarth, T. E. Mallouk, M. H. W. Chan, *Nature Physics* **6**, 389 (2010).

[70] M. S. Anwar, F. Czeschka, M. Hesselberth, M. Porcu, J. Aarts, *Phys. Rev. B* **82**, 100501 (2010).

[71] Y. V. Fominov, A. A. Gulobov, T. Y. Karminskaya, M. Y. Kupriyano, R. G. Deminov, L. R. Tagirov, *JETP Lett.* **91**, 308 (2010).

[72] P. V. Leksin, N. N. Garif'yanov, I. A. Garifullin, Y. V. Fominov, J. Schumann, Y. Krupskaya, V. Kataev, O. G. Schmidt, B. Büchner, *Phys. Rev. Lett.* **109**, 057005 (2012).

[73] A. A. Jara, C. Safranski, I. N. Krivorotov, C. Wu, A. N. Malmi-Kakkada, O. T. Valls, K. Halterman, *Phys. Rev. B* **89**, 184502 (2014).

[74] M. G. Flokstra, T. C. Cunningham, J. Kim, N. Satchell, G. Burnell, P. J. Curran, S. J. Bending, C. J. Kinane, J. F. K. Cooper, S. Langridge, A. Isidori, N. Pugach, M. Eschrig, S. L. Lee, *Phys. Rev. B* **91**, 060501(R) (2015).

[75] X. L. Wang, A. Di Bernardo, N. Banerjee, A. Wells, F. S. Bergeret, M. G. Blamire, J. W. A. Robinson, *Phys. Rev. B* **89**, 140508(R) (2014).

[76] A. Singh, S. Voltan, K. Lahabi, J. Aarts, *Phys. Rev. X* **5**, 021019 (2015).

[77] N. Banerjee, J. W. A. Robinson, M. G. Blamire, *Nat. Commun.* **5**, 4771 (2014).

[78] M. G. Blamire and J. W. A. Robinson, *J. Phys.: Condens. Matter* **26**, 453201 (2014).

[79] J. Linder and J. W. A. Robinson, *Nature* **11**, 307 (2015).

[80] CTI-Cryogenics, *8200^{TM} Compressor: Installation, Operation, and Servicing Instructions*, Helix Technology Corporation (1995).

[81] F. Pobell, *Matter and Methods at Low Temperatures, Second Ed.* Springer-Verlag, Berlin (1996).

[82] R. C. Jaklevic, J. Lambe, A. H. Silver, J. E. Mercereau, *Phys. Rev. Lett.* **12**, 159 (1964).

[83] J. Clarke, A. I. Braginski (Eds.), *The SQUID Handbook, Vol 1.* Wiley-VCH, Weinheim (2004).

[84] R. Kleiner, D. Koelle, F. Ludqig, J. Clarke, *Proceedings of the IEEE* **92**, 10 (2004).

[85] A. H. Silver, J. E. Zimmerman, *Phys. Rev.* **157**, 317 (1967).

[86] S. S. P. Parkin, N. More, K. P. Roche, *Phys. Rev. Lett.* **64** 2304 (1990).

[87] B. Dassonneville, H. Y. T. Nguyen, R. Acharyya, R. Loloee, W. P. Pratt, Jr., J. Bass, *IEEE Transactions on Magnetics* **46**, 6 (2010).

[88] J. Bass, W. P. Pratt, Jr., *J. Phys.: Condens. Matter* **19**, 183201 (2007).

[89] L. Piraux, S. Dubois, A. Fert, L. Belliard, *Eur. Phys. J. B* **4**, 413 (1998).

[90] A. C. Reilly, W.-C. Chiang, W. Park, S. Y. Hsu, R. Loloee, S. Steenwyk, W. P. Pratt, Jr., J. Bass, *IEEE Transactions on Magnetics* **34**, 4 (1998).

[91] M. A. Khasawneh, T. S. Khaire, C. Klose, W. P. Pratt, Jr., N. O. Birge, *Supercond. Sci. Technol.* **24**, 024005 (2011).

[92] E. C. Gingrich, P. Quarterman, Y. Wang, R. Loloee, W. P. Pratt, Jr., N. O. Birge, *Phys. Rev. B* **86**, 224506 (2012).

[93] C. E. Moreau, J. A. Caballero, R. Loloee, W. P. Pratt, Jr., N. O. Birge, *J. Appl. Phys.*, **87** 9 (2000).

[94] T. Yu. Karminskaya, M. Yu. Kupriyanov, *JETP Letters* **85**, 6 (2007).

[95] T. E. Golikova, F. Hübler, D. Beckmann, I. E. Batov, T. Yu. Karminskaya, M. Yu. Kupriyanov, A. A. Golubov, V. V. Ryazanov, *Phys. Rev. B* **86**, 064416 (2012).

[96] Private communication with Dr. Baokang Bi, MSU.

[97] Private communication with Vincent Mourik, Delft, at APS March Meeting 2013, Baltimore.

[98] E. G. Spencer and P. H. Schmidt, *JVST* **8**, 5 (1971).

[99] *One cm Ion Mill Manual*, Commonwealth Scientific (1985).

[100] P. Horowitz, W. Hill, *The Art of Electronics*. Cambridge University Press, Cambridge (1989).

[101] P. Cadden-Zimansky, Z. Jiang, V. Chandrasekhar,*New J. Phys.***9**, 116 (2007).

[102] J. Wang, M. Singh, M. Tian, N. Kumar, B. Liu, C. Shi, J. K. Jain, N. Samarth, T. E. Mallouk, M. H. W. Chan, *Nature Physics* **6**, 389 (2010).

[103] M. Kompaniiets, O. V. Dobrovolskiy, C. Neetzel, W. Ensinger, M. Huth, *J Supercond Nov Magn* **28**, 431 (2015).

[104] P. Charlat, H. Courtois, Ph. Gandit, D. Mailly, A. F. Volkov, B. Pannetier, *Phys. Rev. Lett.* **77**, 24 (1996).